

Copyright

by

Mukremin Kilic

2006

The Dissertation Committee for Mukremin Kilic  
certifies that this is the approved version of the following dissertation:

## Cool White Dwarfs and the Age of the Galaxy

Committee:

---

Don E. Winget, Supervisor

---

Ted von Hippel, Supervisor

---

Hugh C. Harris

---

James Liebert

---

Didier Saumon

---

E. L. Robinson

---

Chris Sneden

# **Cool White Dwarfs and the Age of the Galaxy**

by

**Mukremin Kilic, B.S.**

## **Dissertation**

Presented to the Faculty of the Graduate School of

The University of Texas at Austin

in Partial Fulfillment

of the Requirements

for the Degree of

**Doctor of Philosophy**

**The University of Texas at Austin**

August 2006

to my brother,  
Zakir Abime

# Acknowledgments

When I was trying to decide between graduate schools in astronomy and physics, the total solar eclipse of the last millenium came to my help. Seeing an incredible show put up by the Sun and the Moon led me to pursue a degree in astronomy. I knew that I wanted to do astronomy after that, and I knew that I wanted to be an observer.

The astronomy program in Texas seemed appealing due to its telescopes at McDonald observatory. I knew that Texas was part of the United States, but I did not know that it was in the south, and hot most of the time! I cannot complain though, I had a very good time in Austin. Choosing an advisor seemed difficult at the beginning, since we had to find an advisor in our first semester. I took a class from Don Winget and he seemed to be a nice guy. He had an interesting project to work on, and I ended up working with him. I am glad that I made the right decision back then. Don has so much enthusiasm about astronomy that it spills into the people around him. He fueled my quest for knowledge with his enthusiasm. Without him, I would not be here. Thank you Don.

Something unexpected happened in my second year in graduate school. A world's expert on observational astronomy, Ted von Hippel, descended from the heavens above (Mauna Kea) to Austin. He took our little project at the McDonald 0.8m telescope to bigger telescopes and lead a large group of us to work on the most important question in white dwarf research, the age of the Galaxy using the oldest

white dwarfs. His ideas and insights into the problems made my thesis an order of magnitude more significant. Without his continuous support, I would not be here. Thank you Ted.

I am grateful to Jim Liebert, Hugh Harris, Jeff Munn, Didier Saumon, and Chuck Claver for their help and guidance over the years. I feel lucky to work with Jim and hope that I can have 10% of his expertise one day. Hugh and Jeff came to my help when I needed a new method for my project. Didier shared his state-of-the-art cool white dwarf models with us, and Chuck taught me how to observe with a large telescope and camera. Without these people, I would not be here. I am also thankful to my internal committee members Rob Robinson and Chris Sneden for their support over the years.

Our weekly group meetings in the Whole Earth Telescope (WET) Lab and in the chairman's office turned out to be really useful. Having a chance to discuss anything and everything in those discussions was invaluable. When I joined the WET lab, Travis and Anjum were the only other students in the group. I learned a lot from Anjum, but most importantly I learned driving from her, which surprised everybody who knew about Anjum's driving. She has been a good colleague and friend. I had a chance to work with Fergal on our Spitzer project in my last year, and I enjoyed our soccer games. I enjoyed our lunch meetings with Agnes, Barbara, Elizabeth, and Steve. Mike Montgomery has been the only postdoc in our group, and I am always amazed by his deep physical understanding. He can basically work on any theoretical question in astronomy and physics. I also felt lucky to meet some of my professional brothers, sisters, and uncles (Don's friends and former students) including Scot, Atsuko, Steve Kawaler, Kepler, and Dennis.

I am thankful to my family for supporting me through many years of school. Since they cannot speak English, the following lines will be in Turkish. *Baba, Anne, kardeşlerim beni yıllarca desteklediğiniz için sağolun. Sizin maddi ve manevi*

*desteđiniz olmadan lise ve üniversiteyi bitiremezdim. Çok teşekkürler.* I am also thankful to my friends from the astronomy department, Laurel House, and other friends. They say that there is a lady behind every succesful man, the lady behind me is Vishala. Thank you Vishala for supporting me.

MUKREMIN KILIC

*The University of Texas at Austin*  
*August 2006*

# Cool White Dwarfs and the Age of the Galaxy

Publication No. \_\_\_\_\_

Mukremin Kilic, Ph.D.

The University of Texas at Austin, 2006

Supervisor: Don E. Winget and Ted von Hippel

White dwarf stars represent the most common endpoint of stellar evolution and therefore provide a reliable estimate of the star formation history and age of different Galactic populations. The major observational requirement for accurate age measurements is to have a large sample of cool, old white dwarfs. The intrinsic faintness of the coolest white dwarfs has made them difficult to observe, and the previous studies of the Galactic disk and halo suffered from small samples of cool white dwarfs. The most commonly used sample of cool white dwarfs in the Galactic disk included only 43 stars. The current best estimate for the age of the disk is about 8 billion years. Due to small number statistics, the error in this age estimate is  $\sim 1.5$  billion years. In order to reduce the age uncertainty to less than 10%, we

have created a large sample of cool white dwarfs from the Sloan Digital Sky Survey. We have used a reduced proper motion diagram to effectively identify white dwarfs among many other field stars and assembled a new white dwarf luminosity function including 6000 white dwarfs. This new luminosity function is consistent with an 8 billion years old population and -when supplied with our ongoing near infrared photometric observations- will provide an accurate age estimate for the Galactic disk.

In addition to being accurate cosmochronometers, white dwarfs have become important in the search for dark matter and micro-lensing objects. For many years, astronomers have been trying to understand dark matter. Claims by several investigators that they had found a large number of faint halo white dwarfs in deep field images suggested that halo white dwarfs may exist in large numbers and explain part of the missing matter. In order to test this claim, we have looked at the deepest images of the Universe taken with the *Hubble Space Telescope*. We have obtained proper motion measurements of the point sources in the Hubble Deep Field North and South, and showed that the observed number of white dwarfs is consistent with the standard Galactic models. We have demonstrated that the white dwarfs in these fields do not contribute to dark matter in the Galaxy.

By studying possible planetary systems around white dwarfs, we can predict the future of our solar system and see if the Earth is going to survive the demise of a giant Sun. Even though planets around white dwarfs are waiting to be discovered, the existence of debris disks around several white dwarfs suggest that planets may exist around white dwarfs. Planets in previously stable orbits around a star undergoing mass loss may become unstable, and some of these systems may result in close encounters which could result in tidal stripping of a parent body that would end up in a circumstellar debris disk around a white dwarf. Until recently, there was only a single white dwarf known to have a circumstellar debris disk. We have found four

more debris disks around white dwarfs, all of which turned out to be DAZs - white dwarfs with hydrogen rich atmospheres that have trace amounts of metals. Our observations strengthened the connection between the debris disk phenomenon and the observed metal abundances in cool DAZ white dwarfs. We have demonstrated that accretion from circumstellar debris disks can explain the metal abundances in at least 15% of the DAZ white dwarfs, a problem that has been puzzling astronomers for decades.

# Contents

<b>Acknowledgments</b>	<b>v</b>
<b>Abstract</b>	<b>viii</b>
<b>Chapter 1 Introduction</b>	<b>1</b>
1.1 White Dwarfs: The Quantum Dots . . . . .	2
1.2 White Dwarf Evolution . . . . .	3
1.2.1 Death of a Star, Birth of a White Dwarf . . . . .	3
1.2.2 The Days of Their Lives . . . . .	5
1.2.3 Change of Pace . . . . .	6
1.3 Motivation: What can we learn from White Dwarfs? . . . . .	8
1.4 My Dissertation Project . . . . .	10
<b>Chapter 2 Cool White Dwarfs and the Age of the Galaxy</b>	<b>12</b>
2.1 Introduction . . . . .	12
2.2 Photometric Identification of Cool White Dwarfs . . . . .	15
2.2.1 Forward Approach: Photometry to Spectroscopy . . . . .	17
2.2.2 Reverse Approach: Spectroscopy to Photometry . . . . .	19
2.2.3 Discussion . . . . .	21
2.3 Astrometric Identification of Cool White Dwarfs in the Sloan Digital Sky Survey . . . . .	27

2.3.1	Target Selection . . . . .	28
2.3.2	Observations . . . . .	32
2.3.3	Results . . . . .	36
2.4	A New White Dwarf Luminosity Function . . . . .	52
2.4.1	Construction of a Luminosity Function . . . . .	52
2.5	Conclusion . . . . .	57

### **Chapter 3 The Mystery Deepens: Mid-infrared Observations of White Dwarfs**

3.1	Introduction . . . . .	59
3.2	Target Selection and Observations . . . . .	61
3.3	Results . . . . .	62
3.3.1	White Dwarfs with $T_{\text{eff}} < 7000$ K . . . . .	66
3.3.2	White Dwarfs with $T_{\text{eff}} > 7000$ K . . . . .	69
3.4	Discussion . . . . .	70
3.5	Conclusion . . . . .	74

### **Chapter 4 White Dwarfs and Dark Matter**

4.1	Introduction . . . . .	77
4.2	Hubble Deep Field North . . . . .	78
4.2.1	Proper Motion Measurements . . . . .	78
4.2.2	Results . . . . .	81
4.2.3	Objects brighter than $V = 27$ . . . . .	87
4.2.4	Objects with $27 \geq V \geq 29$ . . . . .	90
4.2.5	Previously Identified High Proper Motion Objects . . . . .	90
4.2.6	Discussion . . . . .	91
4.3	Hubble Deep Field South . . . . .	94
4.3.1	Identification of Point Sources . . . . .	95

4.3.2	The HDFS Second Epoch Data . . . . .	98
4.3.3	Results . . . . .	102
4.3.4	Discussion . . . . .	106
4.4	Conclusion . . . . .	113
<b>Chapter 5</b>	<b>Debris Disks Around White Dwarfs</b>	<b>118</b>
5.1	Introduction . . . . .	118
5.2	Observations . . . . .	120
5.2.1	Photometry . . . . .	120
5.2.2	Spectroscopy . . . . .	121
5.3	Results . . . . .	123
5.4	Discussion . . . . .	129
5.4.1	GD362 . . . . .	129
5.4.2	GD56 . . . . .	130
5.4.3	Possible Trends . . . . .	133
5.4.4	Properties of White Dwarf Debris Disks . . . . .	136
5.5	Conclusions . . . . .	137
<b>Chapter 6</b>	<b>Conclusions and Future Work</b>	<b>139</b>
6.1	An Improved White Dwarf Luminosity Function . . . . .	139
6.1.1	The Future . . . . .	143
6.2	Resolving the Mystery of Cool White Dwarf Atmospheres . . . . .	146
6.3	Debris Disks Around White Dwarfs . . . . .	147
6.3.1	The Future . . . . .	148
6.4	Faint Halo White Dwarfs: The Ultra Deep Field . . . . .	149
6.5	Overview . . . . .	150
	<b>Bibliography</b>	<b>152</b>



# Chapter 1

## Introduction

*“İstikbal Göklerdedir (The future is in the skies).”*

*– M. Kemal Atatürk*

If you are reading these lines, it means that you are one of the  $\sim 10$  select people who are either interested in the current status of white dwarf research, or one of my 7 committee members. My goal was to have 9 committee members, but I was not able to persuade the Graduate School to allow me to have that many people in my committee. The main reason that I wanted to have so many committee members is to make sure that at least 10 people read this dissertation, otherwise what good is it to write a 150 page document?

If you are 40 years or older, you have probably already asked yourself why we are here on planet Earth. Scientifically, I cannot tell you why we are here, but I can try to answer the question of *how*. In this thesis, I will take you on a journey with an old friend, a cool white dwarf, and show you how we can learn about our own existence by studying our solar system, Galaxy, and the Universe. Our old friend has lived for such a long time that he can remember the first stars in our Galaxy, and therefore has a lot to tell us about how our Galaxy formed and evolved.

I will first explain the historical discoveries that lead scientists to reveal the secrets of white dwarf stars, and make a brief introduction to the physics of white dwarfs. The important questions that can be asked using white dwarfs and my efforts to answer these questions will follow.

## 1.1 White Dwarfs: The Quantum Dots

The term “white dwarf” was first used in a scientific journal in 1927 by Van Maanen, however the discovery of the first white dwarf was more than a decade earlier. Russell and Pickering were the first ones to realize the peculiarity of the star 40 Eridani B in 1910 (Schatzman 1958). 40 Eridani B is an A-type star in a triple star system with 40 Eridani A (a K-type dwarf) and 40 Eri C (an M dwarf). A stars are more massive and  $\sim 100$  times brighter than K-type stars. In contrast, Russell and Pickering found that 40 Eridani B is 100 times fainter than 40 Eridani A. In other words, they found it to be ten thousand times fainter than they expected. Two other stars with similar spectral types and brightnesses, Van Maanen 2 and Sirius B, were found by Van Maanen (1913) and Bessel (1844), respectively. Adams (1915) obtained optical spectrum of the companion of Sirius, and found that Sirius B had the same spectral type (A-type) as Sirius. He noted that Sirius B is as massive as the Sun, yet it is 100 times fainter than the Sun and ten thousand times fainter than its companion star, Sirius. Knowing the distance to Sirius B and its surface temperature, Adams was able to estimate the radius of Sirius B and found it to be about 100 times smaller than the Sun. In other words, Sirius B holds as much material as the Sun in a volume as small as the Earth. These results demonstrated that matter thousands of times denser than platinum is not only possible, but is actually present in the Universe (Eddington 1926). 40 Eridani B, Van Maanen 2, and Sirius B initially defined the class of white dwarf stars.

The theoretical explanation for the density of matter in white dwarf stars

came in 1926. Fowler (1926) showed that matter can exist in such a dense state if it has sufficient energy so that the electrons are not bound in their ordinary atomic orbits, but are shared equally among nearly all of the nuclei. The interior of a white dwarf is analogous to one gigantic molecule in its lowest quantum state; a quantum dot (Wheeler 2000). The density of such matter is only limited by the sizes of electrons and atomic nuclei. Pauli's exclusion principle tells us that no two electrons can occupy exactly the same energy-state, and as the average distance between electrons gets smaller the average momentum must get larger. The electrons are pushed to higher speeds because of the density of matter. The electrons with the highest energies move at near light speed and carry considerable momentum, and so they are able to provide support against the pull of gravity. The mystery of white dwarf interiors was solved by the understanding of this electron degeneracy pressure. This pressure strongly depends on the density, but is independent of the temperature, so the star is able to withstand its own gravitation without possessing a higher temperature.

Now that we understand how a dense star can exist, the next question is "how do they form, live, and die?"

## **1.2 White Dwarf Evolution**

### **1.2.1 Death of a Star, Birth of a White Dwarf**

Normal stars like the Sun spend the majority of their lives burning hydrogen. The Sun has been fusing hydrogen into helium for about 4.5 billion years, and theory suggests that it has 5 billion more years to go. When a star has nearly burned up all the hydrogen in its core, the burning will be replaced by burning in a shell further out which is still hydrogen-rich. The star will then have a helium core, an energy producing shell, and a hydrogen-rich envelope. If the star is massive enough, its

core eventually contracts until it reaches the temperature at which helium burning starts. Helium is fused into carbon and oxygen in the core of the star. If the star is not massive enough to reach the temperature needed to fuse carbon and oxygen into heavier elements, it will end up with a carbon/oxygen core surrounded by helium and hydrogen-burning shells and a hydrogen-rich envelope. The extra energy created by the helium and hydrogen-burning shells will cause the envelope to rapidly expand, and the star will eventually lose most of its mass in the giant and asymptotic giant branch phases preceding the planetary nebula phase. The mass loss process, the relative masses of the remnant hydrogen and helium layers, and the relative distribution of carbon and oxygen in the core are still only poorly understood. The remnant left behind will be a newly born white dwarf with a carbon/oxygen core, a helium layer, and in most cases an additional hydrogen layer.

A white dwarf consists of a degenerate core containing the bulk of the mass and a thin non-degenerate envelope. There is an upper mass limit for white dwarfs due to electron degeneracy pressure. Chandrasekhar (1931) showed that if the remnant object is more massive than 1.4 solar masses ( $M_{\odot}$ ), the electron degeneracy will not be sufficient to halt the contraction of the star. Above  $1.4M_{\odot}$  there will be too few energy-states available to the electrons since they cannot travel faster than the speed of light. Therefore, the object may collapse into either a neutron star or a black hole. The endpoint of this collapse is not well known, however it is worth mentioning that the neutron stars have masses  $\sim 1.4M_{\odot}$  (Schulze et al. 2006).

Currently the best estimate for the upper mass limit for main sequence stars becoming white dwarfs comes from star cluster observations. White dwarfs represent the endpoint of the evolution of stars with initial masses ranging from about  $0.07M_{\odot}$  to  $8M_{\odot}$  (Fontaine et al. 2001). This implies that 98% of all stars, including the Sun, will eventually become white dwarfs.

### 1.2.2 The Days of Their Lives

White dwarfs start their lives with surface temperatures of 100-200 kK. They are effectively without nuclear energy sources, and therefore we expect them to radiate energy without replenishment for the rest of their lives. Normal stars have a safety mechanism to prevent secular changes in the star. If the star produces more energy through nuclear burning than it can radiate, the resulting increase in energy leads to an expansion and to a decrease in temperature. Since nuclear burning is highly sensitive to temperature, after a small decrease in temperature thermal equilibrium will be re-established. The same mechanism works in the other case as well; if the star is radiating more energy than it produces, a slight contraction increases the temperature, which in turn increases the rate of energy production, and the thermal equilibrium will be re-established again.

White dwarfs have no such mechanism to keep themselves in thermal equilibrium. The pressure of a degenerate gas depends on the density and is almost independent of the temperature. This means that a white dwarf cannot keep itself in thermal equilibrium by contracting. The electron degeneracy pressure prevents the contraction. A normal star heats up as it loses energy, whereas a white dwarf cools down more as it radiates energy. Therefore white dwarfs spend all of their lives simply cooling.

The interiors of white dwarfs are highly degenerate, and since degenerate electrons are good conductors, the interiors are nearly isothermal. The core temperature is approximately the same as the temperature at the core/envelope boundary. A white dwarf can be treated as having an isothermal core that contains most of the mass of the star and a thin non-degenerate outer layer that acts like an insulating blanket and controls the rate at which the energy is radiated into space (Mestel 1952). The rate of radiation is controlled by the radiative opacity at the boundary between these two layers. Radiative transfer of energy in the core of the star is neg-

ligible compared to thermal conduction. Mestel (1952) created a simple analytical model for white dwarf evolution and showed that to first order there is a simple relation between the age and luminosity of a white dwarf;

$$\log (\tau_{cool}) \propto -\frac{5}{7} \log \left( \frac{L}{L_{\odot}} \right).$$

The beauty of this equation is that it tells us the age of a white dwarf if we know its luminosity. We can measure the ages of white dwarfs and hence use them as chronometers to determine the ages of their parent populations. The Mestel age-luminosity relation is in good agreement with the predictions of detailed numerical models (Iben & Tutukov 1984), and is applicable to white dwarfs with  $-1 \geq \log(L/L_{\odot}) \geq -3$  (Wood 1990). We expect several important physical effects to produce deviations from the classical Mestel cooling theory. Neutrino cooling, surface convection, and crystallization can change the cooling rate of white dwarfs and cause deviations from the Mestel theory (Fontaine et al. 2001).

### 1.2.3 Change of Pace

If you have ever watched water (or anything else with thermal energy) cool down, you probably noticed that it cools down fastest at the beginning, and the cooling slows down with time. The same cooling trend applies to white dwarfs. At the extreme temperatures expected in a hot, young white dwarf star, plasmon neutrinos dominate the energy loss from the star. The energy loss due to neutrinos is an order of magnitude higher than the loss from photons. Plasmon neutrinos drive the evolution of hot white dwarfs and cause the stars to cool down very fast. The effects of neutrinos diminish with decreasing temperature of the star and are predicted to be insignificant below  $\sim 20$  kK (Winget et al. 2004).

As the white dwarf cools down, the interior of the star becomes strongly degenerate, and the only significant energy source is the thermal energy of the star.

Energy transport is dominated by electron thermal conduction in the interior and by radiation in the outer layers. The star basically dissipates its thermal energy and the decrease in its luminosity follows approximately the classical Mestel theory.

As the surface temperature of a white dwarf drops below 15 kK, a convection zone (associated with partial ionization of the dominant element at the surface) develops. Convection lowers the temperature gradient between the surface and the core, and shortens the evolutionary timescale. This causes a deviation from the Mestel cooling and makes the star cool faster.

Another important physical effect that takes place in the interiors of cool white dwarfs is crystallization. As the white dwarfs cool, the Coulomb interactions between ions become significant in the interiors. Kirzhnits (1960), Salpeter (1961), and Abrikosov (1961) showed that the ions should crystallize into a lattice. Crystallization of the interiors of white dwarfs releases latent heat and supplies the stars with an additional energy source (Van Horn 1968). This extra energy delays the cooling of white dwarfs. Theoretical investigators have also proposed delays in white dwarf cooling due to chemical fractionation (phase separation) of carbon and oxygen at the time of interior crystallization resulting in the release of significant gravitational energy (Stevenson 1980; Chabrier et al. 1993; Wood 1995; Fontaine et al. 2001). Carbon and oxygen may not crystallize together, but undergo phase separation upon crystallization. Redistribution of the ions may provide an additional energy source that would delay the white dwarf cooling further. After crystallization the heat capacity in the crystallized regions will be due to lattice vibrations in the form of phonons, and this will result in lower heat capacity. The heat capacity will drop off with  $T^3$  and the white dwarf will cool rapidly.

We expect a typical white dwarf with  $M_\star = 0.6M_\odot$  to crystallize at  $T_{\text{eff}} \sim 6000$  K (Wood 1992). More than 40 years after E. Salpeter’s prediction of crystallization in white dwarf interiors, the first empirical test was achieved by Metcalfe et

al. (2004). Fitting the observed pulsation periods of the massive white dwarf BPM 37093, they concluded that 90% of the star is crystallized. However, the effect of crystallization on white dwarf cooling is not empirically constrained yet, and it is one of the main uncertainties for the age estimates of the coolest white dwarfs.

### 1.3 Motivation: What can we learn from White Dwarfs?

So far I told you about how white dwarfs were discovered in the first place, their formation, structure and evolution with time. The important question is why should we care?

White dwarfs are natural laboratories for testing physics under extreme conditions. We can explore the physics of matter in dense media just by observing these stars. It is impossible to construct an experiment involving such high density and pressure in terrestrial laboratories. As mentioned in the previous section, electron degeneracy, plasmon neutrinos, crystallization, and phase separation are a few of the studies made possible by observations of white dwarf stars.

Stars with initial masses of  $\sim 0.07 - 8M_{\odot}$  will ultimately become white dwarfs (Fontaine et al. 2001). The Sun will become a white dwarf, too. Therefore, studying the evolution of white dwarfs is basically looking into the future of our own solar system. If humanity does not destroy itself in the next 5 billion years, there is a chance that our descendants will watch the Sun get bigger and become a red giant, and then shed its outer layers and turn into a white dwarf. Our planet may or may not survive the red giant phase, but the outer planets probably will survive. Finding and studying planets around white dwarfs will show us our future.

White dwarfs are excellent chronometers for measuring the age of different stellar populations of the Galaxy. They are a homogenous class of objects with a narrow mass distribution. The average mass for white dwarfs is  $0.60M_{\odot}$  with a dispersion of  $0.13M_{\odot}$  (Liebert et al. 2005). We expect all white dwarfs with  $M_{\star} =$

$0.5 - 1.1M_{\odot}$  to have carbon/oxygen cores, with overlying helium layers and possibly an additional hydrogen layer (Iben 1991). Their high surface gravity ( $\log g \sim 8$ ), slow rotation rates, and low magnetic fields imply that they are physically simple. They have no nuclear or gravitational energy generation, therefore the only energy source that they can use is the residual thermal energy of the ions. Their evolution is simply cooling. All of these factors show that we can use white dwarfs as cosmic chronometers to reveal the archeological record of the Galaxy, including the star formation history of the disk, thick disk, and halo of our Galaxy.

White dwarfs are also believed to be the progenitors of Supernovae of type Ia. If a white dwarf is in a binary system with another star, it may accrete material from the companion star and its mass may come close to the Chandrasekhar mass limit ( $1.4M_{\odot}$ ). The accreted material will increase the central density of the white dwarf until carbon can ignite. Carbon ignition and subsequent thermonuclear runaway is thought to happen when the white dwarf has a mass about 1% less than the Chandrasekhar mass. When carbon burns, it releases energy and the star cannot respond to the extra energy by expanding and cooling itself. Instead, the temperature continues to increase, the burning goes even faster and it cannot be controlled. Oxygen also ignites in the center, and all the fuel is consumed all the way to iron-peak elements. The result is a thermonuclear explosion that blows the white dwarf up completely (Wheeler 2000). Astronomers use Type Ia supernovae as standard candles: objects whose absolute magnitude is thought to be very well known. By comparing the relative intensity of light observed from the object with that expected based on its assumed absolute magnitude, we can infer the distance to the object. By measuring the redshift and brightness of the supernova we can determine its distance and discern the geometry of the universe. An understanding of the structure and dynamical properties of white dwarfs may improve our understanding of the resultant Type Ia supernovae.

Recently, halo white dwarf stars were proposed to be part of the dark matter in the Galaxy which would explain the microlensing events observed towards the Large Magellanic Cloud. Alcock et al. (2000) found that 20% of the dark matter in the Galaxy may be in the form of  $0.5M_{\odot}$  objects. Since the average mass for white dwarfs is  $\sim 0.6M_{\odot}$ , halo white dwarfs were thought to be good candidates to explain the observed microlensing events. The discovery of several high proper motion objects in the Hubble Deep Field North and South and among the field stars suggested that halo white dwarfs may exist in larger numbers than expected from theoretical predictions and therefore explain part of the dark matter. Constraining the contribution of faint halo white dwarfs to dark matter will reveal what dark matter is or what it is not.

These are only a few of the interesting questions that can be answered using white dwarfs, and there are many more questions to be asked and to be answered.

## 1.4 My Dissertation Project

When I talked to Don Winget about possible projects to work on, he mentioned that one of the biggest problems in white dwarf research is the “number” of cool white dwarf stars. At the time, the best estimate of the age of the Galactic disk (Winget et al. 1987) came from a sample of 43 cool white dwarfs discovered by Liebert et al. (1988). Using this sample, Leggett et al. (1998) estimated the Galactic disk to be  $8 \pm 1.5$  billion years old. My thesis project was to greatly expand the sample of cool white dwarfs in order to decrease the uncertainty in the age of the Galactic disk as determined from white dwarf cosmochronology, and possibly find enough cool halo white dwarfs to determine the age of the halo as well. Through the years, I mostly worked on this problem, however I explored other interesting problems related to white dwarfs as well, including their contribution to dark matter, their near- and mid-infrared flux distributions, and debris disks around them.

Most of the work presented in this dissertation has already been published as first author papers in the *Astrophysical Journal* and *Astronomical Journal*. Since I have done this work with many collaborators, I will use “we” to refer to the first person for the rest of this thesis. The organization of this dissertation is as follows:

Chapter 2 describes our efforts to identify cool white dwarfs photometrically and astrometrically. I provide a detailed account of how we succeeded in finding a large number of cool white dwarfs to create an accurate white dwarf luminosity function. The text is derived from three papers published in the *Astronomical Journal* by Kilic et al. (2004b, 2006a) and Harris et al. (2006).

Chapter 3 describes our survey of cool white dwarfs in the mid-infrared. Our goal was to explore their flux distributions in the mid-infrared, and we discovered something surprising. This chapter is based on a paper published in the *Astrophysical Journal* by Kilic et al. (2006b).

Chapter 4 is derived primarily from two papers published in the *Astrophysical Journal* by Kilic et al. (2004a, 2005b). It describes our analysis of point sources in the Hubble Deep Field North, South, and the Ultra Deep Field. Our goal in this analysis was to determine the contribution of halo white dwarfs to Galactic dark matter.

Chapter 5 tells the story of our exciting discoveries of debris disks around white dwarfs. We are finally finding evidence of possible planetary systems around white dwarfs. This work is based on two papers published in the *Astrophysical Journal* by Kilic et al. (2005a, 2006c).

Chapter 6 is a summary of the major conclusions of this work and outlines future directions.

## Chapter 2

# Cool White Dwarfs and the Age of the Galaxy

*“The stars the moon and the sun...so old, so wise. Think of what they have seen.”*

*– E. Paluszak*

### 2.1 Introduction

White dwarf stars are the remnants of the earliest and all subsequent generations of star formation and they are tracers of the age and evolution of the Galaxy. They are initially hot and consequently cool rapidly, though the cooling rate slows as their temperature drops, allowing the oldest white dwarfs to remain visible with current technology. Because the cooling rate slows, any census finds more and more white dwarfs at lower and lower temperatures (and luminosities) until, quite abruptly, we find no more of them. Such a census is called the white dwarf luminosity function.

Attempts to exploit the white dwarfs as chronometers showed that the white

dwarf luminosity function was a map of the history of star formation in the disk, and that there was a shortfall of low luminosity white dwarfs – the inevitable consequence of the finite age of the disk (Liebert 1979; Winget et al. 1987; Liebert et al. 1988). The largest samples to date used to determine the white dwarf luminosity function are those of Fleming et al. (1986; see Liebert et al. 2005 for an updated version) on the hot end and Oswalt et al. (1996, using white dwarfs in common proper motion binaries) on the cool end. The most commonly used luminosity function for cool white dwarfs (Liebert et al. 1988) was based on a sample of only 43 stars selected on the basis of large proper motion from the Luyten Half Second Proper Motion Survey (Luyten 1979). Wood & Oswalt (1998) argue that space densities obtained from a sample of 50 objects could be in error by as much as 50%, and the ages inferred from observed distribution must be considered uncertain by 15% from sampling statistics alone (see Geijo et al. 2006). Depending on how the data are binned, as many as 3 or as few as 1 of the 43 objects occupy the last bin in the luminosity function. The simple fact is, the faintest, age-dependent end of the white dwarf luminosity function is not yet reliably determined (see Figure 2.1).

The need to construct a larger, deeper and more complete sample is obvious. At the 12th European Conference on white dwarfs in June 2000, the white dwarf community identified deriving a high quality luminosity function with an order of magnitude more white dwarfs than presently available as the single most important project in this field (von Hippel 2001). Of even greater interest is the possibility of delineating a useful sample of white dwarfs from the local halo, which may be drawn largely from a single burst of star formation at a greater age than the disk. Oppenheimer et al. (2001) claimed to have found a significant population of halo white dwarfs from kinematic surveys, though this claim was later disputed by several investigators (Reid et al. 2001; Reyle et al. 2001; Silvestri et al. 2002; Bergeron 2003; Spagna et al. 2004).

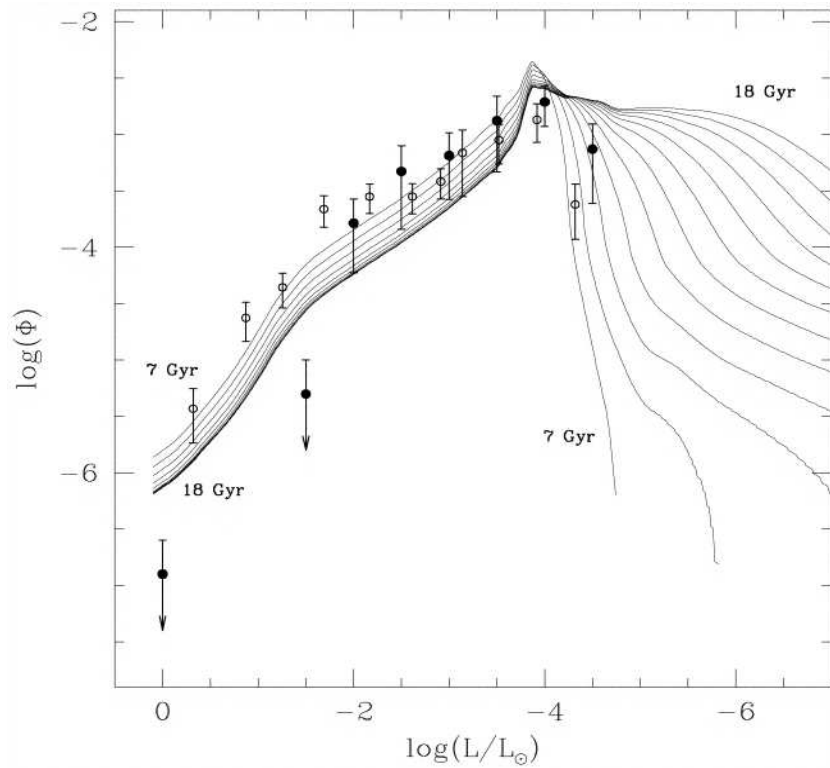


Figure 2.1: Theoretical age fits to the Liebert et al. (1988) (open circles) and Oswalt et al. (1996) (filled circles) white dwarf luminosity functions, from Wood & Oswalt (1998). Theoretical white dwarf luminosity functions are marked with age in Gyr from 7 to 18 Gyr. Current white dwarf luminosity function error bars are too large to precisely constrain the Galactic disk age.

An investigation of the cool end of the white dwarf luminosity function that is focused on disentangling theoretical uncertainties in the cooling process would greatly benefit from a much larger sample of cool white dwarfs. The details of the constituent input physics can affect the implied ages of white dwarfs below  $\log(L/L_{\odot}) \sim -4.2$  by as much as 2–3 Gyr, hence are critical for using white dwarfs as chronometers (Knox et al. 1999; Montgomery et al. 1999; Chabrier et al. 2000b; Salaris et al. 2000).

In order to create a large sample of cool white dwarfs, we used two different observational methods; a photometric and an astrometric search.

## 2.2 Photometric Identification of Cool White Dwarfs

A magnitude-limited, kinematically-unbiased sample of white dwarfs can be obtained through a photometric survey. A unique color signature is necessary to photometrically identify a white dwarf among the many other types of field stars. The magnitude limit of a survey is also a critical factor in the search for cool white dwarfs; if the survey cannot provide sufficiently high signal to noise ratio data for  $M_V \sim 16$ , it cannot recognize cool low luminosity white dwarfs. Broad-band photometric surveys can be used to find hot white dwarfs due to their blue colors. Recently, Kleinman et al. (2004) found 2551 new white dwarfs with  $T_{\text{eff}} \geq 8000$  K in the Sloan Digital Sky Survey Data Release 1.

Broad-band filter photometry has a limited capacity to distinguish metal poor subdwarfs from cool white dwarfs. In the absence of significant line blanketing, both the white dwarfs and subdwarfs have broad-band colors that closely approximate those of a blackbody. However, by comparing the flux through a magnesium absorption line-centered filter, e.g. DDO51, several authors have suggested that cool white dwarfs could be distinguished from other field stars of similar  $T_{\text{eff}}$  (Claver 1995; Harris et al. 2001; Kilic et al. 2003). This is because the majority of

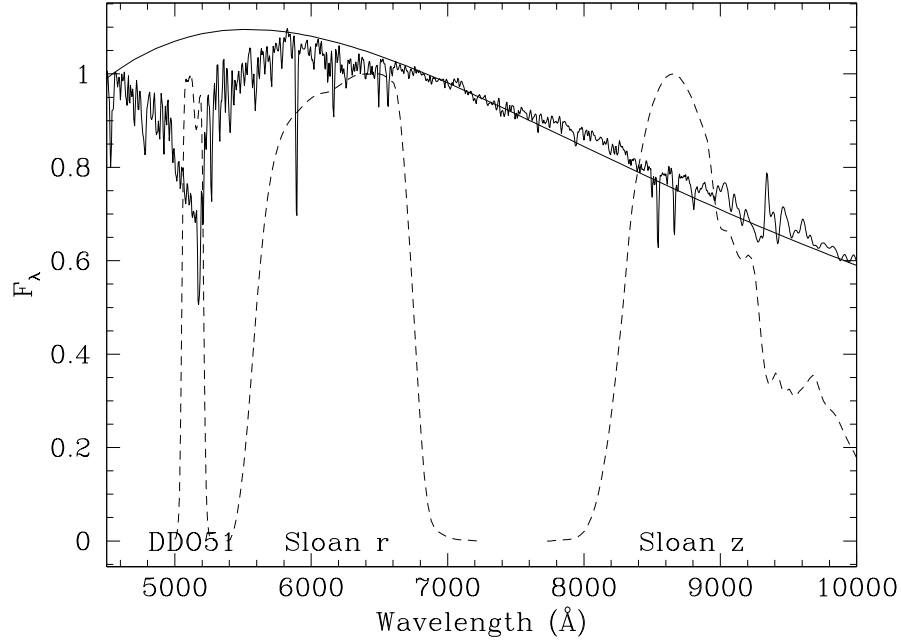


Figure 2.2: Template spectra for a K3V star (Pickles 1998) and a 5000 K H-rich white dwarf (Saumon & Jacobson 1999). The tracing for the DDO51, SDSS r, and z filters are shown as dashed lines. The greatest difference between the white dwarf and the template stellar spectrum, Mg absorption, is apparent in this figure.

cool white dwarfs have essentially featureless spectra around 5150 Å, whereas subdwarfs and main sequence stars show significant absorption from the Mg b triplet and/or MgH. Figure 2.2 shows a template spectra for a K3V star (Pickles 1998) and a 5000 K white dwarf spectrum along with the tracing of the DDO51, SDSS r, and z filters. It is clear from this figure that white dwarfs should be distinguishable from the subdwarf stars using the narrow-band DDO51 filter and a combination of broad-band filters. Mg absorption is the strongest feature in the range sampled by the chosen filters, r, z, and DDO51.

### 2.2.1 Forward Approach: Photometry to Spectroscopy

In order to test the above claim, E. Olsewzki kindly provided us with DDO51 photometry of an area of 2 square degrees from the Spaghetti Survey (Morrison et al. 2000) which overlaps with the Sloan Digital Sky Survey fields. A color-color diagram for this field is shown in Figure 2.3. Main sequence stars are shown as small dots, and a typical error bar for these objects is shown in the lower left corner of the figure. Two hot white dwarfs found by the Sloan Digital Sky Survey are shown as open circles. Spectroscopically identified QSOs and stars (which are not white dwarfs) are shown as open squares and filled triangles, respectively. White dwarfs are expected to be separated from main sequence stars in this color-color diagram (see Figure 4.11 of Claver 1995); we have selected stars that deviate from the main sequence as possible cool white dwarf candidates. Cool white dwarf candidates selected for follow-up spectroscopy at the 9.2m Hobby-Eberly Telescope (HET) and the McDonald 2.7m Telescope are shown as filled circles (see Table 2.1 for photometric information).

Table 2.1: Objects with HET + McDonald 2.7m Spectroscopy

No	Object	DDO51	u	g	r	i	z	Type
1	J114149.41–001140.4	19.67	20.49	19.77	19.14	18.05	17.32	WD+M3
2	J120650.72–010519.1	20.29	22.44	20.81	19.44	17.87	17.11	M4
3	J120651.91–010435.2	19.31	21.30	19.38	18.59	18.32	18.14	K2
4	J120709.16–011247.2	16.84	18.12	16.90	16.34	15.70	15.33	WD+M2
5	J120741.55–010630.9	19.89	22.70	20.07	19.62	18.39	18.17	K3
6	J123202.54–010232.1	20.33	22.88	20.59	19.25	17.94	17.25	M1
7	J123208.81–010230.5	20.69	22.52	20.68	19.82	19.37	19.03	K3
8	J131833.56–004448.4	16.59	18.76	16.80	16.11	15.68	15.41	K2
9	J143044.16–002853.1	16.99	18.74	17.09	16.53	16.35	16.63	K0

Follow-up spectroscopy of 9 white dwarf candidates in the Spaghetti Survey Field was obtained in April and May 2002 using the HET and in February 2003 using the McDonald 2.7m Telescope. We used the HET equipped with the Marcario Low

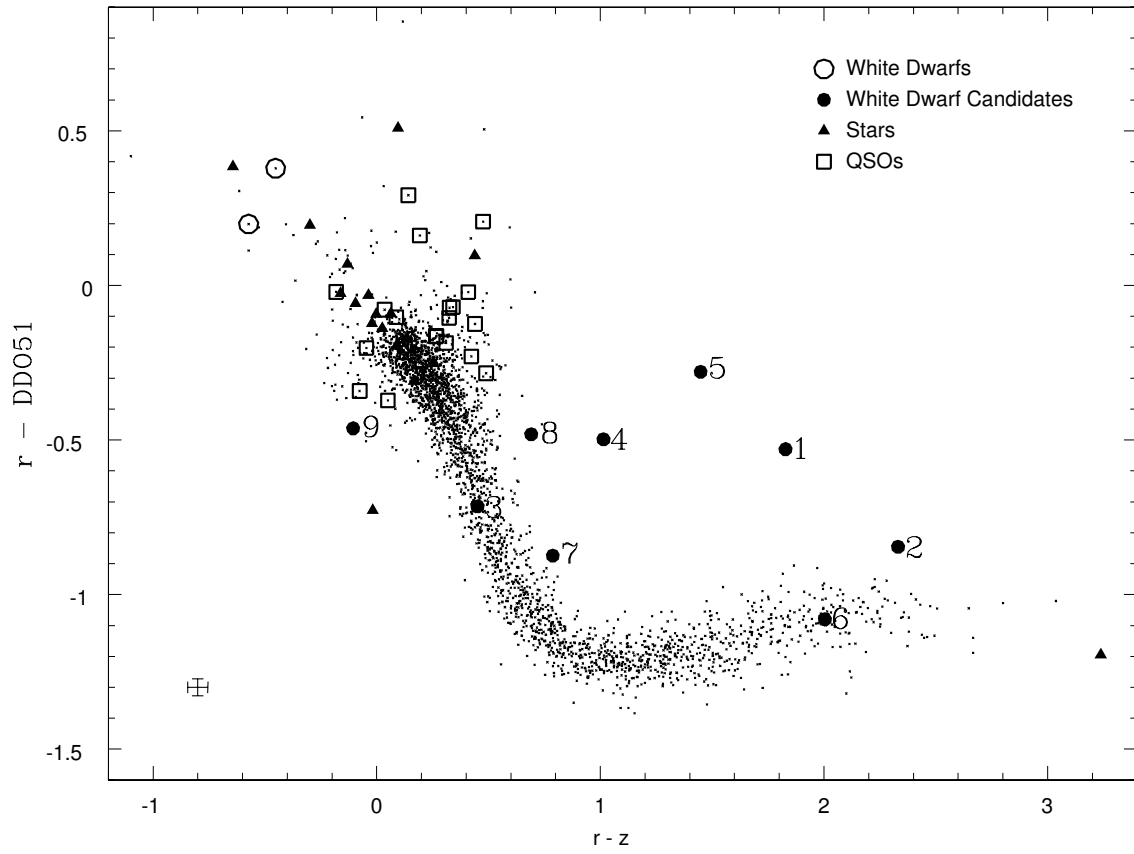


Figure 2.3:  $r - \text{DDO51}$  vs.  $r - z$  color-color diagram of a 2 square degree field from the Spaghetti Survey.

Resolution Spectrograph (LRS) to obtain low resolution spectroscopy of four cool white dwarf candidates. Grism 1 with a  $2''$  slit produced spectra with a resolution of  $16 \text{ \AA}$  over the range  $4000 - 10000 \text{ \AA}$ . Spectroscopy for four additional stars was obtained at the McDonald 2.7m Telescope with the Imaging Grism Instrument (IGI) and TK4 camera using the holographic grating, which produced spectra with a resolution of  $12 \text{ \AA}$  over the range  $4000 - 8000 \text{ \AA}$ . A spectrophotometric standard star was observed each night for flux calibration. Ne–Cd calibration lamp exposures were taken after each observation with the HET, and Ne–Ar lamp calibrations were taken at the beginning of the night for the 2.7m observations. The data were reduced using standard IRAF routines.

The observed spectra for selected white dwarf candidates from the HET and the 2.7m showed that two of the objects observed at the HET, SDSS J114149.41–001140.4 and SDSS J120709.16–011247.2 are white dwarf + late type star spectroscopic binaries. SDSS J114149.41–001140.4 also shows strong  $H\beta$  and  $H\gamma$  lines. None of the other candidates turned out to be white dwarfs. This discovery contradicted the expected yield of the DDO51 filter which led us to reconsider our strategy for using this filter. We then pursued a reverse approach which is described in the next section.

### 2.2.2 Reverse Approach: Spectroscopy to Photometry

Follow-up spectroscopy of photometrically selected cool white dwarf candidates resulted in the discovery of subdwarf stars and unusual binaries instead of cool white dwarfs. In order to test the effectiveness of the filter in distinguishing cool white dwarfs from subdwarf stars, we decided to observe known cool white dwarfs with the DDO51 filter. DDO51, r, and z band photometry of 30 known cool white dwarfs with temperatures ranging from 10000 K down to very cool temperatures ( $T_{\text{eff}} \leq 3500 \text{ K}$ ) was obtained at the CTIO 4m–Blanco Telescope and Kitt Peak 4m–Mayall Tele-

scope equipped with the  $8k \times 8k$  MOSAIC Imager in November 2002 and June 2003, respectively.

The MOSAIC Imager when used with these 4m telescopes provides a  $35' \times 35'$  field of view. The CCD images were processed with the standard procedures in the MSCRED package in IRAF v2.12. We adopted the reduction procedures used by the NOAO Deep Wide-FieldSurvey Team<sup>1</sup>. Source identifications were performed on the projected images using the SExtractor package (Bertin & Arnouts 1996) v2.1.6. The main motivation for using the SExtractor package was its morphological classification capability. SExtractor uses a neural network to classify objects as stars (stellarity=1) or galaxies (stellarity=0). Stellarity is a continuous variable that can take any value from 0 to 1. A comparison of stellarity indices with magnitudes show that objects with stellarity index  $\geq 0.8$  have reliable classification as stars. We selected all objects with a stellarity index larger than 0.8 and with photometric errors less than 0.1 mag for our analysis. Only those objects detected in each filter that matched up to within  $0.5''$  or better in each coordinate are included in our final catalog.

Most of our observations were obtained under photometric conditions. Since we are mainly interested in the differential photometry between white dwarfs and the rest of the field stars, data from non-photometric nights are also useful. We have cross-correlated color-color diagrams for each field with the data from the Spaghetti Survey and matched the observed field star sequences to remove any photometric offsets from non-photometric observing conditions. Figure 2.4 shows the color-color diagram for 30 known white dwarfs and surrounding field stars. Field stars from the Spaghetti Survey and our study are shown as black dots. A typical error bar for the field stars is shown in the lower left corner of the figure. A good match between our data and the Spaghetti Survey data is apparent in this figure. Known white

---

<sup>1</sup><http://www.noao.edu/noao/noaodeep/ReductionOpt/frames.html>

dwarfs are shown as filled circles. Our synthetic photometry of white dwarf model atmospheres (kindly made available to us by D. Saumon) are also shown.

Temperatures and colors for the observed white dwarfs are given in Table 2.2. The observed white dwarf sequence is in agreement with our follow-up spectroscopy, and both demonstrate that white dwarfs are much closer to (and more blended with) the main sequence stars than previously predicted. Cool white dwarfs occupy a region running from the center of the field star locus ( $r - \text{DDO} = -0.1$ ,  $r - z = 0.05$ ) for  $T_{\text{eff}} \sim 7000$  K to the red edge of the field star locus ( $r - \text{DDO} = -0.75$ ,  $r - z = 0.65$ ).

### 2.2.3 Discussion

Our observations demonstrate that the narrow-band DDO51 filter, centered on the Mg band, is not as effective at separating white dwarfs from subdwarfs as we expected. White dwarfs with temperatures between 7000 K and 5000 K ( $-0.10 \geq r - \text{DDO} \geq -0.45$ ,  $0.05 \leq r - z \leq 0.35$ ) are photometrically indistinguishable from observed field stars. Using template spectra from the Pickles (1998) library, we have measured the equivalent width of the Mg/MgH feature in main sequence stars. Mg absorption becomes strong enough to affect the photometry in K0 ( $T_{\text{eff}} \sim 5000$  K) and later type stars (see Figure 2.5). Due to the spread in colors and weak Mg absorption in the F-G type stars, white dwarfs with  $7000 \text{ K} \geq T_{\text{eff}} \geq 5000 \text{ K}$  have similar colors to F-G stars.

White dwarfs with temperatures in the range 5000 – 3500 K ( $-0.45 \geq r - \text{DDO} \geq -0.80$ ,  $0.35 \leq r - z \leq 0.65$ ) lie just above the edge of the observed field star sequence. Until recently, cool white dwarfs were thought to have spectral energy distributions similar to blackbodies. In fact, this is why Claver (1995) suggested that a narrow-band filter centered on the MgH feature would place cool white dwarfs above the observed field star sequence; the DDO51 filter would separate

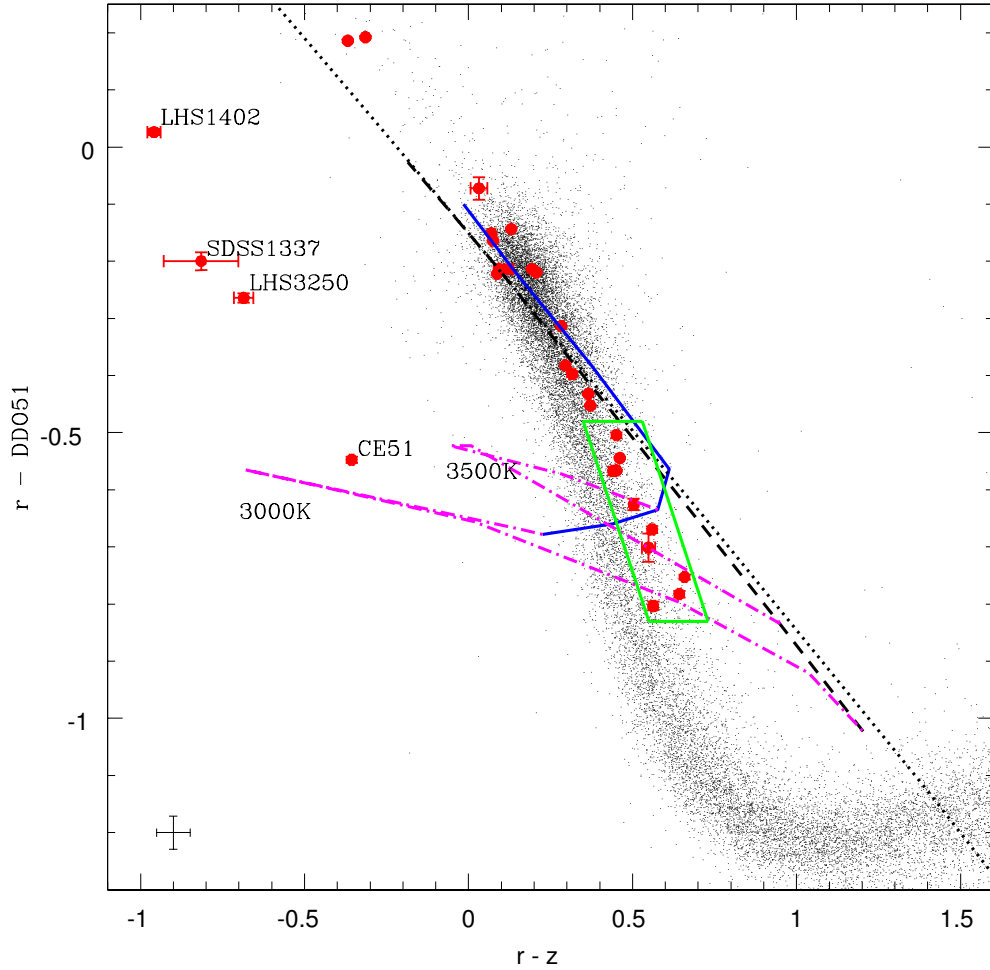


Figure 2.4:  $r - \text{DDO51}$  vs.  $r - z$  color-color diagram for 30 known white dwarfs (filled circles) and the surrounding field stars (black dots). Our synthetic photometry of pure H and pure He white dwarf models with  $7000 \geq T_{\text{eff}} \geq 3000$  K are shown as solid and dashed lines, respectively. Dashed-dotted lines represent mixed atmospheres for 3500 K and 3000 K white dwarfs with different compositions ( $\log [N(\text{He})/N(\text{H})] = -1$  through 6) and a blackbody is also shown as a dotted line. The green box marks a possible search region for cool white dwarfs.

Table 2.2: DDO51 photometry for previously identified white dwarfs

Object	R	r-z	$\sigma_{r-z}$	r-DDO	$\sigma_{r-DDO}$	$T_{\text{eff}}(\text{K})$
WD2323+157	15.04	-0.31	0.01	0.19	0.01	10170
LTT 9491	14.07	-0.37	0.01	0.19	0.01	...
CE157	15.64	0.03	0.03	-0.07	0.02	7000
WD1325+581	16.42	0.07	0.01	-0.15	0.01	6810
WD1633+572	14.68	0.08	0.01	-0.16	0.01	6180
WD2107-216	16.45	0.09	0.01	-0.21	0.01	5830
WD2347+292	15.41	0.13	0.01	-0.14	0.01	5810
WD0752-676	13.58	0.09	0.01	-0.22	0.01	5730
CE162	16.69	0.12	0.01	-0.21	0.01	5730
WD1257+037	15.46	0.21	0.01	-0.22	0.01	5590
WD2248+293	15.14	0.19	0.01	-0.21	0.01	5580
WD0121+401	16.67	0.28	0.01	-0.31	0.01	5340
WD1334+039	14.12	0.36	0.01	-0.43	0.01	5030
WD2002-110	16.36	0.29	0.01	-0.38	0.01	4800
WD0045-061	17.70	0.32	0.01	-0.40	0.01	...
WD1820+609	15.15	0.37	0.01	-0.45	0.01	4780
LHS 542	17.53	0.44	0.04	-0.57	0.01	4720
WD1108+207	17.17	0.45	0.01	-0.50	0.01	4650
WD1345+238	15.12	0.45	0.01	-0.57	0.01	4590
WD2251-070	15.10	0.46	0.01	-0.54	0.01	4580
CE40	18.82	0.50	0.01	-0.63	0.01	4580
CE142	18.59	0.55	0.02	-0.70	0.02	4390
CE16	17.59	0.64	0.01	-0.78	0.01	4330
WD1300+263	18.09	0.56	0.01	-0.67	0.01	4320
WD1247+550	17.03	0.66	0.01	-0.75	0.01	4050
F351-50	18.37	0.56	0.01	-0.80	0.01	3500:
CE51	17.50	-0.36	0.01	-0.55	0.01	2730:
LHS 3250	17.87	-0.69	0.03	-0.26	0.01	...
SDSS J1337+00	19.16	-0.82	0.11	-0.20	0.02	...
LHS 1402	17.86	-0.96	0.02	0.03	0.01	...

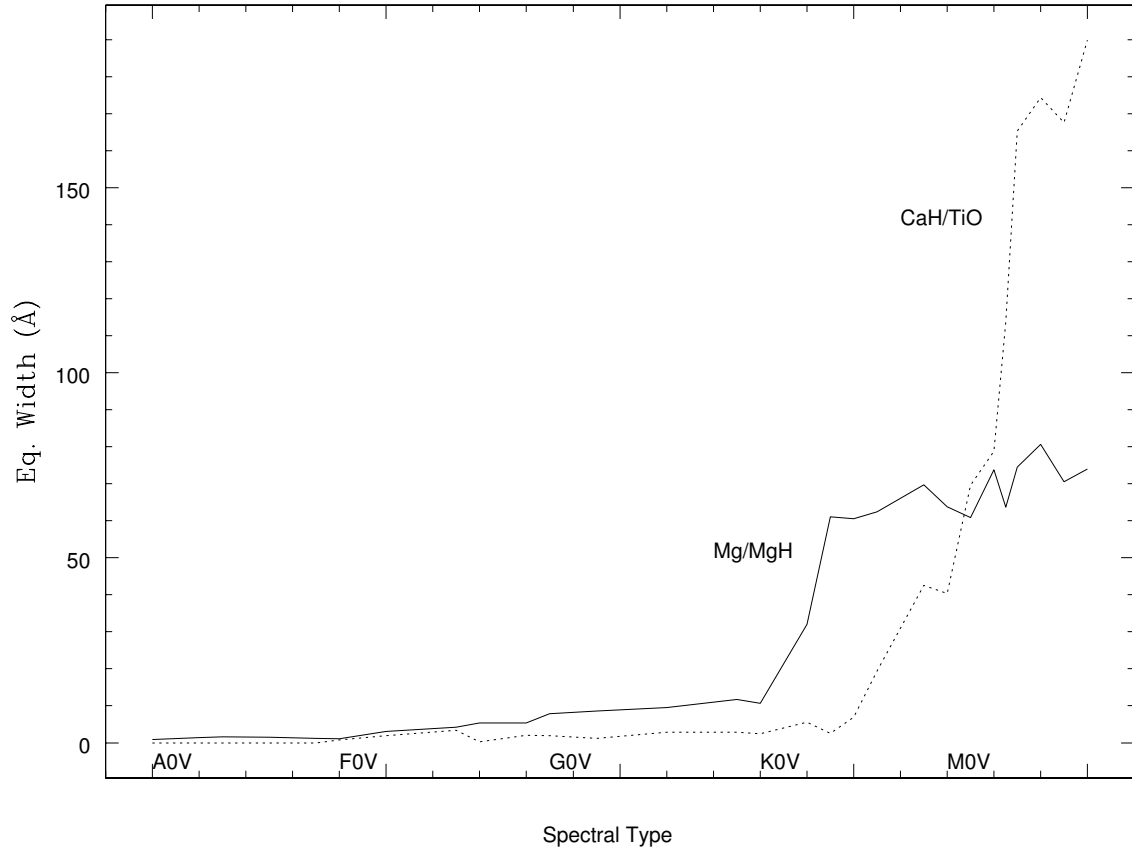


Figure 2.5: Equivalent width of the Mg/MgH and CaH+TiO features measured from Pickles (1998) template spectra. The Mg/MgH feature becomes strong enough to affect the photometry in K0 and later type stars, whereas the CaH+TiO feature dominates at  $\sim 6850$  Å for M0 and later type stars.

blackbodies from subdwarfs (see Figure 2.2 and Figure 2.4). Although subdwarfs have strong MgH absorption in this temperature range (Figure 2.5) and they deviate from blackbodies, observed white dwarfs deviate from blackbodies, too. The effects of collision induced absorption (CIA) due to molecular hydrogen are expected to be significant below 5000 K (Hansen 1998; Saumon & Jacobson 1999). Figure 2.4 shows that in these colors, there are no pure H white dwarfs with  $T_{\text{eff}} \leq 5000$  K and the observed white dwarf sequence actually continues along between the pure H and the pure He models. This is also seen in the  $B - V$  vs.  $V - K$  color-color diagrams of Bergeron, Ruiz & Leggett (1997) and Bergeron et al. (2001) which implies that either all cool white dwarfs have mixed H/He composition, the calculated CIA opacities are incorrect, or there are other neglected physical effects (more on this in Chapter 3). We note that Bergeron & Leggett (2002) suggested that all white dwarfs cooler than 4000 K have mixed H/He atmospheres.

The effective temperature range between 5000 and 3500 K is the most important regime for white dwarf luminosity function studies since it defines the turn-off of the white dwarf luminosity function, hence the age of the observed population. A single slit spectrograph would not be efficient in finding those objects preselected by the DDO51 photometry technique, but a wide field multi-object spectrograph, e.g. Hectospec (Fabricant et al. 1994) with 300 fibers on the converted Multiple Mirror Telescope, might be used productively to carve out regions from the  $r$ -DDO51 vs.  $r$ - $z$  color-color diagram to find cool white dwarfs in this range. Figure 2.4 shows a possible search box (shown in green) for cool white dwarfs. For a one square degree field at a Galactic latitude  $l = 38^\circ$ , the box includes 234 stars down to  $r = 21.5$ . Using the Liebert et al. (1988) white dwarf luminosity function and a disk scale height of 250 pc, we expect to find one cool white dwarf per square degree in the search box ( $5000 \text{ K} \geq T_{\text{eff}} \geq 3500 \text{ K}$ ). In other words, the average pointing with the MMT + Hectospec should yield a cool white dwarf. The above field has 660 stars

in the color range  $-0.80 \leq r\text{--}DDO \leq -0.45$  and 1014 stars in the range  $0.35 \geq r\text{--}z \geq 0.65$ . Even though the DDO51 filter technique is not as efficient as expected, it rejects at least 65% of main sequence stars in this temperature range. Therefore, it is  $\sim 3$  times more efficient than purely spectroscopic (i.e. no prior photometry) surveys. The DDO51 filter is widely used to identify halo stars and to distinguish between giants and dwarfs (Morrison et al. 2001). Thus, as a byproduct, DDO51 photometry from the Spaghetti Survey and similar surveys can be used to identify cool white dwarf candidates for follow-up spectroscopy.

Four ultra-cool white dwarfs (CE51, LHS3250, SDSS J1337+00, and LHS1402) lie to the left of the field stars and are clearly separated from the observed sequence of stars due to their depressed near-infrared colors which is thought to be the result of CIA absorption. DDO51 filter photometry is not necessary for finding ultra cool white dwarfs since these stars have broad molecular features and they can be found using broad-band photometry, e.g. in the Sloan Digital Sky Survey (Gates et al. 2004). On the other hand, it can help identify the elusive He-rich ultra cool white dwarfs because they approximate a blackbody spectral energy distribution.

Mg/MgH and CaH+TiO are the most prominent features in the optical spectra of subdwarf stars. In addition to the DDO51 filter, we have also investigated the use of an intermediate-band filter centered on the CaH+TiO band at  $\sim 6850\text{\AA}$  (Claver 1995) to test whether it can be used to identify white dwarfs. Equivalent width measurements of this band using the Pickles (1998) template spectra are shown in Figure 2.5. CaH+TiO absorption becomes strong in M0 ( $T_{\text{eff}} \sim 3800\text{ K}$ ) and later type stars. White dwarfs in this temperature range show depressed infrared colors due to CIA if they have pure-H or mixed H/He atmospheres, and they can be identified by using the DDO51 filter if they have pure-He atmospheres. The CIA exhibited by ultra cool white dwarfs is extremely broad-band and monotonically varies throughout the red-infrared region, whereas the CaH/TiO band is

very narrowly confined in wavelength. Thus, the CaH+TiO filter, if ratioed with another nearby pseudocontinuum filter, could show a much stronger dependency on temperature and metallicity in main sequence and subdwarf stars than it does in ultra cool white dwarfs. Therefore, the CaH+TiO filter and *JHK* infrared photometry may be useful for the identification of cool hydrogen-rich or mixed atmosphere white dwarfs, though broad-band photometry surveys are also successful in finding ultra cool white dwarfs (e.g. Sloan Digital Sky Survey; Harris et al. 2001; Gates et al. 2004).

### 2.3 Astrometric Identification of Cool White Dwarfs in the Sloan Digital Sky Survey

Our efforts to find a large number of cool white dwarfs through a photometric search were unsuccessful. DDO51 filter turned out to be less efficient than expected and we were forced to change our strategy to something more efficient; identification of white dwarfs astrometrically.

The reduced proper motion technique (Luyten 1918) offers an efficient means to identify cool white dwarfs, as well as halo white dwarfs, by their underluminosity in comparison to main sequence stars with similar colors and their high space motions, respectively. The reduced proper motion, defined as  $H = m + 5 \log \mu + 5$ , where  $m$  is the apparent magnitude and  $\mu$  is the proper motion in arcseconds per year, has long been used as a proxy for the absolute magnitude of a star, for a sample with similar kinematics.

When we were searching for a reliable method of identifying cool white dwarfs from the Sloan Digital Sky Survey (SDSS), Jeff Munn and his collaborators came to our help by presenting an improved proper-motion catalog combining the USNO-B (Monet et al. 2003; 5 epochs) and SDSS catalogs in the area of sky covered by SDSS

Data Release 1 (DR1; Abazajian et al. 2003). SDSS performs imaging in five broad optical bands ( $u, g, r, i$ , and  $z$ ) down to  $\sim 22$  magnitude in  $u, g$ , and  $r$  with 95% completeness for point sources. Munn et al. (2004) used SDSS astrometry to recalibrate the USNO-B plate astrometry, reducing both the statistical and systematic errors significantly. In addition, SDSS positions were used to eliminate the large number of false high proper motion objects in the USNO-B catalog. The combination of accurate SDSS photometry and SDSS+USNO-B astrometry enables us to construct a reduced proper motion diagram (RPM) and select cool white dwarf candidates from the disk and halo.

### 2.3.1 Target Selection

Munn et al. (2004) presented an RPM diagram for a portion of SDSS DR1 in their Figure 12. Their SDSS+USNO-B catalog is 90% complete to  $g = 19.7$ , with proper motion errors  $\sim 3.5 \text{ mas yr}^{-1}$  in right ascension and declination. Four populations are delineated as roughly parallel diagonal distributions in their diagram. The old Population I main sequence is seen in the top right, and the Population II main sequence separates fairly cleanly to the left and extends down past  $H_g = 21$  near  $g-i = 2$ . The white dwarf sequence appears to separate to the left of the Population II subdwarfs, and an unconfirmed extension of this appears as a sequence of objects to higher  $H_g$  and redder color.

Figure 2.6 presents the RPM diagram for all stars in SDSS Data Release 2 (DR2; Abazajian et al. 2004) with  $15 < g < 20$  and with reliably measured proper motions greater than  $20 \text{ mas yr}^{-1}$ . Individual stars are plotted only if they are bluer than  $g-i = 0$  or if  $H_g > 15.136 + 2.727(g-i)$ , a cut which should include all white dwarfs; the remaining vast majority of stars are represented by the contours, as there are too many stars to plot individually. Spectroscopically confirmed white dwarfs, white dwarf plus M dwarf binaries, subdwarfs, and QSOs are

plotted as blue triangles, green triangles, red squares, and cyan circles, respectively. The spectroscopic identifications are drawn from the SDSS Data Release 1 white dwarf catalog (Kleinmann et al. 2004) and QSO catalog (Schneider et al. 2003), and the McCook & Sion (2003) catalog. We also classified all currently available SDSS spectra for stars in the diagram with  $g - i > 0$  or  $H_g > 19$ , and which had not previously been classified (190 objects total). The expected sequences of white dwarfs (pure H atmospheres,  $\log g = 8$ ) for specific tangential velocities ( $V_T$ ) are shown as solid lines, where colors and absolute magnitudes are predicted using model atmospheres from P. Bergeron (private communication). The white dwarf cooling curves pass through the locus of hotter white dwarfs, then make a sharp turn due to the onset of collision-induced absorption (CIA) due to molecular hydrogen for the coolest stars with pure H atmospheres (Hansen 1998; Saumon & Jacobson 1999); this opacity depresses the  $i$  band, making the colors turn bluer.

Defining a “reliable” proper motion is important, as even a small fraction of stars with falsely measured large proper motions will scatter stars from the very densely populated subdwarf turnoff region of the RPM diagram into the sparsely populated region expected to contain the cool white dwarfs. We adopt a prescription for a reliably measured proper motion similar to that delineated by Munn et al. (2004) for their catalog: (1) the SDSS detection in both the  $g$  and  $i$  band must match the “clean” criteria as described in the DR1 documentation, (2) there must be a one-to-one match between the SDSS and USNO-B objects, and (3) the proper motion fit must have an rms residual of less than 525 mas in each coordinate. We further require the star to have been detected in all 5 epochs in USNO-B, and for the distance to the nearest neighbor with  $g < 22$  (Dist22) to exceed  $7''$ . The final two requirements are based on inspection of all the plate images used in the USNO-B catalog for a subsample of 562 stars in the portion of the RPM diagram expected to be populated by halo and cool disk white dwarfs ( $-1 < g - i < 1.5$

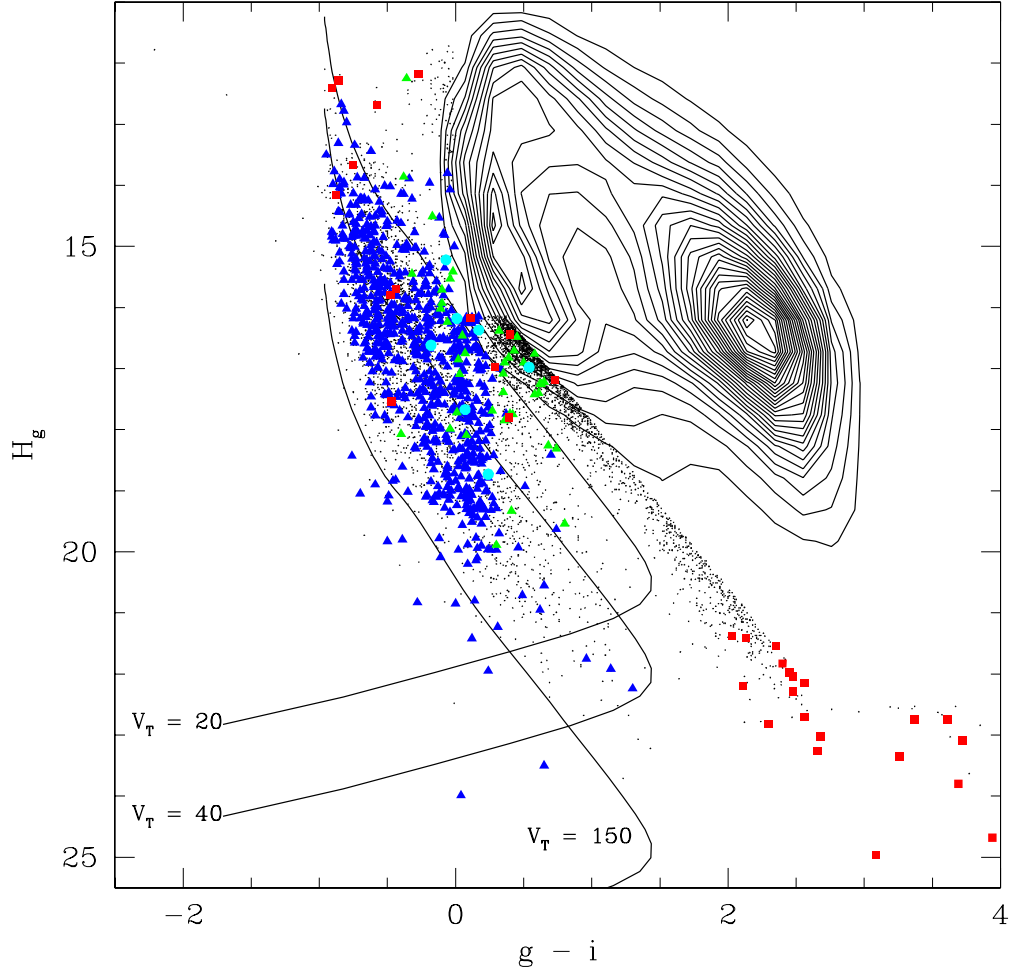


Figure 2.6: The reduced proper motion diagram for stars in the SDSS DR2. Individual stars are plotted only in the region of interest for white dwarfs, the remaining stars are represented by the contours. Previously known white dwarfs, white dwarf plus late type star binaries, subdwarfs, and quasars are shown as blue triangles, green triangles, red squares, and cyan circles, respectively. White dwarf cooling curves for different tangential velocities are shown as solid lines. The  $V_T = 20$ – $40$   $\text{km s}^{-1}$  curves mark the expected location of disk white dwarfs, whereas the  $V_T = 150$   $\text{km s}^{-1}$  curve represents the halo white dwarfs.

and  $H_g > 18$ ), and with proper motions greater than  $100 \text{ mas yr}^{-1}$  (the reality of measured proper motions smaller than that were too difficult to judge using the quick by-eye inspections we employed). Of the 201 inspected stars that were detected in all 5 USNO-B epochs, and whose nearest neighbor (brighter than  $g = 22$ ) is greater than  $7''$  away, only 3 were judged to have a falsely measured large proper motion, for a 1.5% contamination rate. On the other hand, of the 20 inspected stars that were detected in all 5 USNO-B epochs but had a neighbor closer than  $7''$ , 7 were judged to have an incorrectly measured proper motion, for a contamination rate of 35%. Objects separated by less than  $7''$  tend to be blended on the Schmidt plates, leading to incorrectly measured proper motions. All of the 208 inspected stars which were not detected in one or two of the USNO-B epochs and which have a nearest neighbor closer than  $7''$  had incorrectly measured proper motions. Even if the nearest neighbor is greater than  $7''$  away, the contamination rate of falsely measured large proper motions increases for stars not detected in all 5 USNO-B epochs. For such stars, 20 of 39 inspected stars not detected in one of the USNO-B epochs had incorrectly measured proper motions, for a contamination rate of 51%, while 81 of 91 not detected in two of the USNO-B epochs had incorrectly measured proper motions, for a contamination rate of 89%.

In Figure 2.6, it is clear that the hot white dwarfs previously targetted spectroscopically by SDSS are well separated from main sequence and subdwarf stars (represented by the contours) and are located where expected from the models. It is also clear that the white dwarf locus extends to redder  $g - i$  and to larger reduced proper motion, well separated from the subdwarf locus (the diagonal cut where we start to plot individual stars), and that SDSS has not spectroscopically observed most of these cooler white dwarf candidates. This drove our target selection. Our goal was to obtain spectroscopic identifications for a large sample of cool white dwarf candidates so as to understand the efficiency of using reduced proper motions

to select cool white dwarfs as well as the contamination due to subdwarfs. Thus we selected most of our targets from the region with  $g - i > 0$  and to the left of the  $V_T = 20 \text{ km s}^{-1}$  curve, though we also selected some to the right of the curve to better understand how cleanly the white dwarf and subdwarf loci separate.

### 2.3.2 Observations

Follow-up spectroscopy of the cool white dwarf candidates were obtained at the HET, the MMT, and the McDonald 2.7m Telescope between September 2003 and July 2006. We used the HET equipped with the Marcario Low Resolution Spectrograph (LRS) to obtain low resolution spectroscopy of 90 cool white dwarf candidates. Grism 2 with a  $1.5''$  slit produced spectra with a resolution of  $6 \text{ \AA}$  over the range  $4280 - 7340 \text{ \AA}$ . Spectroscopy for 56 additional stars was obtained at the MMT with the Blue Channel Spectrograph and the  $500 \text{ l/mm}$  grating, which produced spectra with a resolution of  $3.6 \text{ \AA}$  over the range  $3640 - 6800 \text{ \AA}$ . In addition, we obtained spectroscopy for 89 stars at the McDonald 2.7m Telescope with the Large Cassegrain Spectrograph (LCS) and TI1 camera using grating No. 43 ( $600 \text{ l/mm}$ ), which produced spectra with a resolution of  $5.2 \text{ \AA}$  over the range  $3870 - 5260 \text{ \AA}$ . In each case, a spectrophotometric standard star was observed each night for flux calibration. Ne–Cd, He–Ar–Ne, and Ar calibration lamp exposures were taken after each observation with the HET, the MMT, and the McDonald 2.7m Telescope, respectively. The data were reduced using standard IRAF routines.

The spectra for 39 white dwarfs observed at the HET and the MMT are shown in Figures 2.7 and 2.8. The spectra are ordered in decreasing  $g - r$  color. The majority of the objects observed at the HET and the MMT are featureless cool DC white dwarfs. The only features seen in these spectra are due to sky subtraction problems at  $5577$ ,  $5890/5896$ ,  $6300$ , and the atmospheric  $B$  band at  $6890 \text{ \AA}$ . Several white dwarfs show only a weak  $H\alpha$  line and are DA white dwarfs with probably

cool, H-rich atmospheres. Most of the brighter objects observed at the McDonald 2.7m are DA white dwarfs (see Kilic et al. 2006a). Three objects clearly show additional features due to late type star companions (J0929+5547, J1336+0017, J2340-1106). Two objects observed at the 2.7m are magnetic DAs (J1011+0029, J1144+6629), while two other objects observed at the 2.7m and an additional three objects observed at the MMT are DZAs with detectable Ca II H and K lines and Balmer lines (J0045+1420, J0748+3506, J1627+4859, J1654+3829, J2154+1300).

The biggest difficulty in classifying the spectra is to distinguish DZ, DZA and DAZ white dwarfs<sup>2</sup> with refractory heavy elements from nondegenerate probable-main sequence stars (subdwarf F, G, and K types) with low, scaled-solar heavy elements. Ca appears most frequently in DZ, DAZ and DZA stars, followed by Mg, Fe and occasionally Na. The white dwarfs apparently never show the CH band (4300 Å) which is detected for sdG and cooler stars ( $g - i > 0.4$ ), and do not show MgH and CaH which appear in progressively-cooler sdK stars.

Subdwarfs have Ca II (hence need MMT and McDonald 2.7m blue coverage), and usually many other metal features plus the CH molecular band. Additional MgH and CaH bands can be seen among cooler subdwarfs (without enough blue coverage, HET was mostly used to observe cool white dwarf candidates with similar colors to G and K type subdwarfs). We paid close attention to the  $u - g$  and  $g - r$  colors of each star, comparing colors of each candidate with white dwarf model colors to see if they were consistent with the strengths of the H lines, and the degree to which cool DA Balmer decrements steepen until for the coolest DA's only  $H\alpha$  is seen.

Our classifications and additional data for the 112 spectroscopically-confirmed white dwarfs and 55 subdwarfs from this study are given in Tables 2.3 and 2.4, respectively. Positions are those from the SDSS Astrometric pipeline (Pier et al.

---

<sup>2</sup>Note that the difference between DAZ and DZA stars is whether the dominant atmospheric constituent is hydrogen or helium, respectively. DZA stars show steep Balmer decrements at higher  $T_{\text{eff}}$  than DAZ stars.

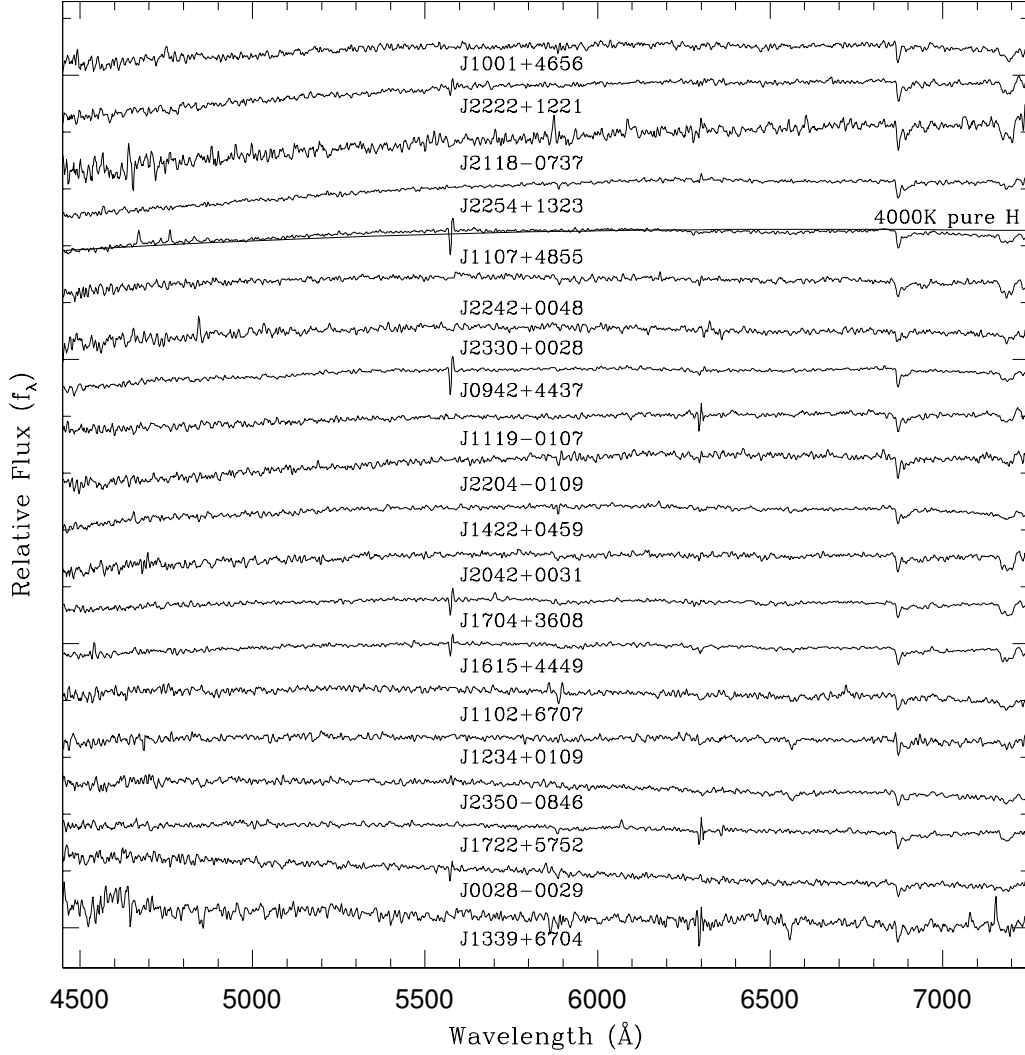


Figure 2.7: Optical spectra for 20 white dwarfs observed at the Hobby–Eberly Telescope. The spectra are normalized at 5500 Å, and are shifted vertically from each other by arbitrary units. The synthetic spectrum of a 4000 K pure H atmosphere white dwarf (D. Saumon, private communication) is also shown. The  $g - r$  color increases from bottom to top.

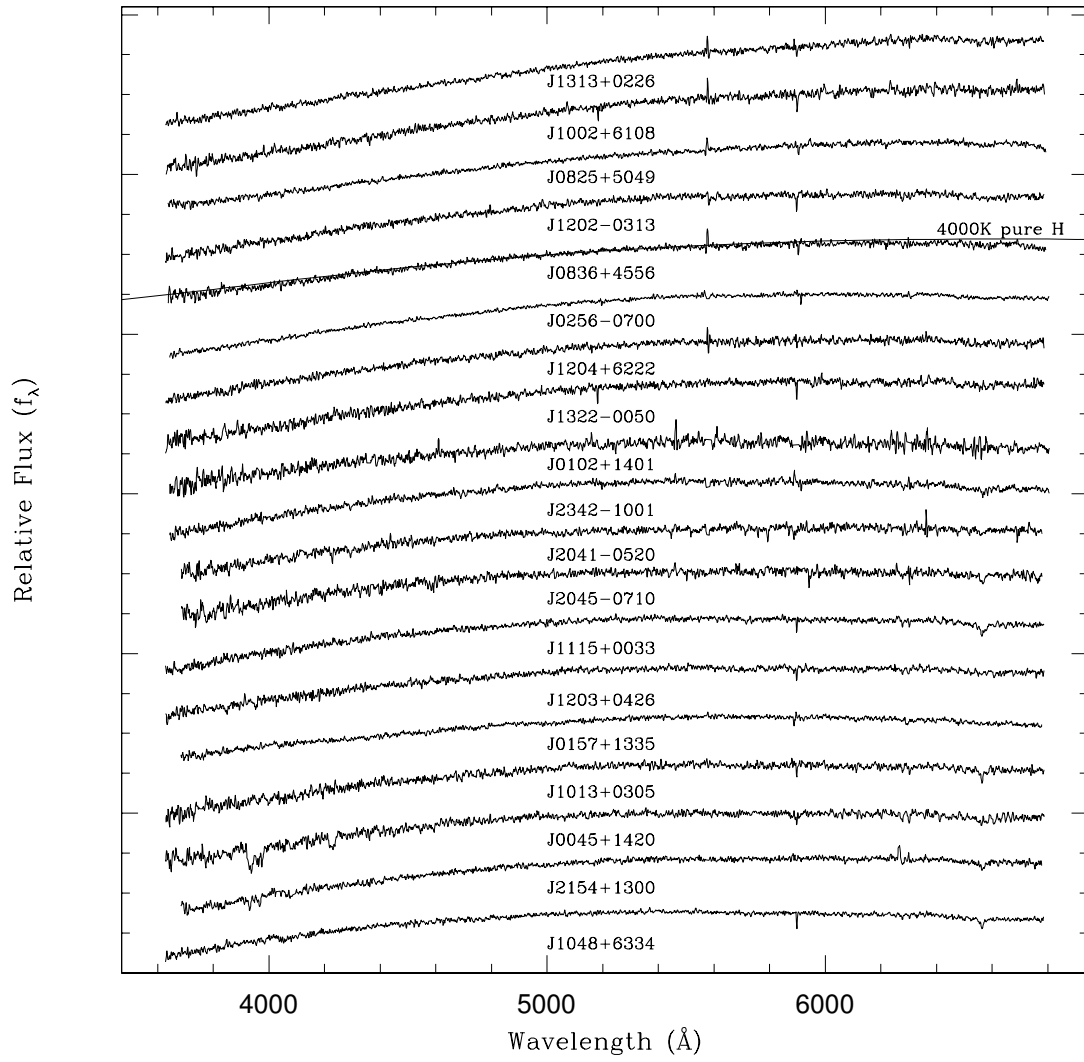


Figure 2.8: Same as figure 2.7, but for white dwarfs observed at the MMT.

2003). The photometric calibration is based on the SDSS standard star system (Smith et al. 2002) tied to the survey data with the Photometric Telescope (Hogg et al. 2001). Interstellar absorption  $A_u$  from Schlegel, Finkbeiner & Davis (1998), and fully dereddened magnitudes and colors are given for each object. Tables 2.3 and 2.4 also give the proper motions in each component and the number of epochs in which an object is detected. In addition, the effective temperatures, photometric distances and the tangential velocities for the newly discovered cool white dwarfs (see §2.3.3) are also given in Table 2.3.

A few stars in Table 2.3 were previously known as likely white dwarfs. The most certain case is SDSS J131313.12+022645.8 (LHS2696) which has a (preliminary) parallax in Dahn et al. (1989). There are 13 additional stars discovered in the NLTT catalog, (Luyten 1979), most with Luyten color class a, f, or g, that would have been considered to be nearly certain white dwarfs on the basis of the NLTT data alone; our spectra now confirm these classifications. The one very cool white dwarf in our sample that is also in the NLTT catalog is SDSS J075313.28+423001.6 (LP207-50). It has color class m in the NLTT, so would not be considered as a white dwarf from the NLTT data alone. In addition, three stars in our sample were identified from their proper motion by Lépine et al. (2003): SDSS J100225.85+610858.1 (LSR 1002+6108), SDSS J110731.38+485523.0 (LSR 1107+4855), and SDSS J222233.90+122143.0 (LSR 2222+1221). The first two were classified as probably white dwarfs and the third as probably a subdwarf on the basis of their reduced proper motion and photographic colors.

### 2.3.3 Results

#### Reduced Proper Motion Diagram

Figure 2.9 repeats the RPM diagram of Figure 2.6, except that the spectroscopic identifications from our work are indicated rather than previously known identifi-

Table 2.3: Spectroscopically Identified White Dwarfs

Object (SDSS J)	g	u-g	g-r	r-i	i-z	$A_u$	$\mu_{ra}$	$\mu_{dec}$	Ep	Type	$T_{\text{eff}}$ (K)	$M_{\text{bol}}$	$M_g$	D (pc)	$V_T$	Source
00 03 16.69-01 11 17.9	19.21	1.22	0.49	0.22	0.02	0.16	98	-16	6	DA	5351	14.57	15.14	69.19	32.57	MMT
00 11 42.67-09 03 24.3	17.73	0.64	0.31	0.12	0.01	0.21	4	-134	6	DA	6125	13.97	14.37	50.31	31.97	2.7m
00 28 37.06-00 29 28.9	19.68	0.54	0.36	0.04	-0.11	0.10	103	67	6	DC	6381	13.80	14.16	128.79	75.01	HET
00 43 16.02+15 40 59.5	18.11	0.53	0.18	0.01	-0.05	0.28	-37	25	6	DA	6844	13.49	13.82	79.16	16.76	2.7m
00 45 21.88+14 20 45.3	18.81	1.35	0.63	0.21	0.03	0.55	260	-53	6	DZA	4732	15.11	15.90	45.73	57.51	MMT
01 02 59.98+14 01 08.1	19.29	1.71	0.73	0.27	0.11	0.22	12	106	6	DC	4582	15.25	16.10	46.84	23.68	MMT
01 15 14.73+14 35 57.5	18.54	0.52	0.25	0.09	-0.02	0.31	-45	-55	4	DA	6320	13.84	14.21	81.60	27.49	MMT
01 28 27.47-00 45 12.6	17.74	1.02	0.37	0.15	0.00	0.16	147	-43	6	DA	5854	14.18	14.62	44.54	32.33	2.7m
01 57 43.25+13 35 58.2	19.15	1.19	0.64	0.16	0.05	0.25	87	-62	6	DC	5040	14.84	15.51	57.63	29.18	MMT
01 59 38.43-08 12 42.4	19.80	0.42	0.09	-0.10	0.01	0.13	322	-119	6	DA	8214	12.69	13.01	230.40	374.90	MMT
02 50 05.81-09 10 02.8	18.87	1.06	0.48	0.18	0.05	0.15	106	DA	6	DA	5474	14.47	15.00	62.59	31.45	MMT
02 56 41.62-07 00 33.8	18.81	1.73	0.80	0.34	0.08	0.26	373	-202	6	DC	4211	15.62	16.56	30.94	62.22	MMT
02 58 54.42+00 30 40.4	18.84	0.73	0.27	0.06	-0.07	0.42	-80	16	6	DA	6189	13.93	14.32	92.32	35.70	MMT
03 09 24.87+00 25 25.3	17.75	0.84	0.34	0.13	-0.02	0.57	-6	-106	6	DC	5637	14.34	14.83	46.60	23.45	2.7m
03 14 49.81-01 05 19.3	18.31	0.88	0.38	0.12	-0.04	0.39	-77	-71	6	DA	5709	14.29	14.76	58.48	29.03	2.7m
03 16 13.90-08 16 37.6	16.63	0.56	0.17	0.02	-0.04	0.48	90	-103	6	DA	6610	13.64	13.99	39.65	25.71	2.7m
03 30 54.88+00 37 16.5	19.33	0.81	0.34	0.10	0.01	0.57	77	34	6	DA	5690	14.30	14.78	98.78	39.41	MMT
04 06 32.39-04 32 50.4	17.02	0.53	0.17	0.00	-0.10	0.56	171	80	6	DA	6624	13.63	13.98	48.89	43.75	2.7m
04 06 47.32-06 44 36.9	17.70	0.74	0.34	0.07	0.03	0.45	67	27	6	DA	5884	14.15	14.59	48.70	16.67	2.7m
07 48 11.90+35 06 32.4	18.08	1.13	0.36	0.09	-0.07	0.30	-44	-141	6	DZA	5925	14.12	14.55	56.16	39.32	2.7m
07 53 13.28+42 30 01.6	17.91	1.84	0.84	0.30	0.10	0.23	113	-403	6	DC	4226	15.61	16.54	20.36	40.39	2.7m
07 56 31.11+41 39 50.9	16.76	0.52	0.18	0.03	-0.05	0.20	-9	-349	6	DA	6951	13.42	13.75	42.59	70.48	2.7m
08 20 36.99+43 10 05.3	17.40	0.49	0.08	0.03	-0.09	0.33	-63	-103	6	DA	7192	13.27	13.59	64.72	37.04	2.7m
08 20 56.07+48 03 52.9	17.16	0.62	0.24	0.12	-0.06	0.22	224	-80	6	DA	6388	13.79	14.16	42.91	48.37	2.7m
08 23 07.81+48 33 16.6	17.79	0.74	0.25	0.10	-0.02	0.22	-217	-72	6	DA	6378	13.80	14.16	57.26	62.06	2.7m
08 25 19.70+50 49 20.1	19.17	1.72	0.86	0.33	0.05	0.24	-331	-330	6	DC	4048	15.79	16.74	33.42	74.04	MMT
08 36 41.56+45 56 58.7	19.89	1.63	0.84	0.27	0.15	0.15	-64	-169	6	DC	4373	15.46	16.36	53.19	45.56	MMT
08 37 12.30+46 13 25.1	18.39	0.69	0.29	0.09	0.00	0.14	-80	-40	6	DA	6363	13.81	14.18	72.90	30.90	MMT
09 19 48.92+01 13 53.0	18.21	0.73	0.30	0.11	0.00	0.13	137	-193	6	DA	6227	13.90	14.29	63.81	71.58	2.7m
09 29 03.12+55 47 58.5	17.85	0.43	0.23	1.05	0.87	0.15	-350	-18	6	DA+M	6719	13.57	13.91	64.55	107.23	2.7m
09 34 38.94+53 29 37.4	17.47	0.51	0.20	0.04	-0.01	0.06	-151	-145	6	DA	6976	13.40	13.73	57.12	56.68	2.7m
09 42 44.96+44 37 43.1	19.44	1.92	0.88	0.37	0.19	0.06	-135	-189	6	DC	4052	15.79	16.73	35.66	39.25	HET
10 01 19.48+46 56 50.6	19.24	2.06	1.06	0.33	0.09	0.07	-17	-339	6	DC	3284	16.71	17.48	23.08	37.13	HET
10 02 25.85+61 08 58.1	19.34	2.32	0.96	0.38	0.18	0.08	-448	-328	6	DC	3581	16.33	17.20	27.79	73.15	MMT
10 05 21.05+53 54 08.4	18.02	0.50	0.24	0.05	-0.02	0.04	-145	-219	6	DA	6800	13.52	13.85	68.91	85.79	2.7m
10 11 05.63+00 29 44.4	17.23	0.69	0.31	0.11	-0.02	0.18	-219	55	6	DAH	6184	13.93	14.32	40.48	43.33	2.7m
10 13 59.85+03 05 53.8	18.60	1.37	0.63	0.23	0.10	0.16	107	-101	6	DA	4964	14.90	15.60	42.00	29.29	MMT
10 14 14.45+04 01 37.4	16.76	0.46	0.11	0.01	-0.06	0.11	-199	26	6	DA	7506	13.08	13.40	48.78	46.41	2.7m

Object (SDSS J)	g	u-g	g-r	r-i	i-z	$A_u$	$\mu_{ra}$	$\mu_{dec}$	Ep	Type	$T_{\text{eff}}(\text{K})$	$M_{\text{bol}}$	$M_g$	D (pc)	$V_T$	Source
10 22 10.36+46 12 49.2	16.42	0.42	0.20	0.05	-0.06	0.07	9	-121	6	DA	6993	13.39	13.72	35.38	20.35	2.7m
10 23 56.10+63 48 33.8	18.08	0.86	0.34	0.09	0.00	0.05	-344	-216	6	DA	6243	13.89	14.28	58.47	112.58	2.7m
10 48 01.84+63 34 48.9	17.90	1.43	0.61	0.29	0.02	0.04	-258	-142	6	DA	5004	14.87	15.55	29.94	41.79	MMT
11 02 13.70+67 07 52.6	19.55	1.74	0.65	0.29	0.03	0.09	-380	-185	6	DC	4840	15.01	15.76	59.24	118.67	HET
11 07 31.38+48 55 23.0	19.39	2.02	0.92	0.30	0.12	0.11	-726	-79	6	DC	4020	15.82	16.77	34.85	120.64	HET
11 11 54.54+03 37 26.2	18.22	0.91	0.37	0.11	0.06	0.21	-371	-127	6	DA	5899	14.14	14.57	57.72	107.28	2.7m
11 13 06.26+00 32 43.7	17.60	0.53	0.21	-0.07	-0.04	0.34	-363	-89	6	DC	6953	13.42	13.75	65.60	116.21	2.7m
11 15 36.96+00 33 17.3	17.75	1.52	0.66	0.24	0.05	0.23	37	-250	6	DA	4816	15.04	15.79	26.57	31.83	MMT
11 19 40.62-01 07 55.1	19.79	2.01	0.85	0.24	0.15	0.23	-291	-28	6	DC	4283	15.55	16.47	49.77	68.97	HET
11 36 55.18+04 09 52.6	16.98	0.45	-0.10	0.32	0.51	0.12	-96	-53	4	DA	10077	11.79	12.18	95.28	49.52	2.7m
11 43 52.16-01 31 49.4	17.36	0.72	0.24	0.09	-0.02	0.10	-277	-2	6	DA	6594	13.65	14.00	48.57	63.78	2.7m
11 44 39.54+66 29 28.5	17.47	0.62	0.22	0.04	-0.06	0.05	-145	-20	6	DAH	6919	13.44	13.77	55.76	38.68	2.7m
11 46 25.77-01 36 36.9	16.48	0.59	0.25	0.12	-0.06	0.07	358	-434	6	DA	6516	13.70	14.05	31.35	83.61	2.7m
12 02 00.48-03 13 47.4	19.86	2.37	0.85	0.32	0.06	0.15	-73	134	6	DC	4151	15.69	16.62	47.03	34.01	MMT
12 03 28.65+04 26 53.4	18.11	1.36	0.66	0.28	0.08	0.10	-252	156	6	DC	4852	15.00	15.75	30.66	43.07	MMT
12 04 39.54+62 22 16.4	19.16	1.69	0.78	0.29	0.10	0.10	-21	-159	6	DC	4528	15.31	16.17	40.92	31.11	MMT
12 05 29.15+04 49 35.6	18.45	0.89	0.48	0.19	0.07	0.09	-138	-53	6	DC	5524	14.43	14.94	51.65	36.19	MMT
12 33 22.45+06 07 10.7	18.21	1.32	0.55	0.19	0.03	0.09	-79	-352	6	DA	5302	14.61	15.19	41.41	70.80	2.7m
12 34 08.12+01 09 47.4	19.73	1.40	0.54	0.25	0.03	0.13	-284	-55	6	DA	5177	14.72	15.34	79.01	108.34	HET
12 38 47.85+51 22 07.4	17.32	0.46	0.12	-0.02	-0.13	0.07	-319	-21	6	DA	7710	12.96	13.29	65.38	99.06	2.7m
13 00 21.25+01 30 45.5	17.74	1.23	0.54	0.18	0.12	0.10	-374	145	6	DA	5297	14.61	15.20	33.48	63.66	2.7m
13 01 21.14+67 13 07.4	16.69	0.56	0.25	0.09	-0.04	0.06	151	52	4	DA	6629	13.63	13.97	35.51	26.88	2.7m
13 03 13.03-03 23 23.9	16.81	0.45	0.16	0.02	-0.09	0.13	32	-137	6	DA	7160	13.29	13.62	45.47	30.32	2.7m
13 13 13.12+02 26 45.8	18.84	2.04	1.07	0.37	0.18	0.14	-744	-116	6	DC	3394	16.56	17.38	20.23	72.21	MMT
13 22 54.60-00 50 42.8	18.82	1.75	0.76	0.31	0.09	0.14	-156	118	6	DC	4505	15.33	16.20	35.08	32.52	MMT
13 36 16.05+00 17 32.7	17.34	0.51	0.36	0.76	0.58	0.12	-278	-141	6	DA+M	6116	13.98	14.38	40.76	60.23	2.7m
13 39 39.55+67 04 49.8	19.79	0.75	0.28	0.12	-0.02	0.07	-194	235	5	DA	6409	13.78	14.14	137.61	198.77	HET
13 40 43.35+02 03 48.3	18.01	1.11	0.43	0.20	0.04	0.13	-534	28	6	DC	5600	14.37	14.87	44.45	112.66	2.7m
13 57 58.43+60 28 55.3	18.04	0.72	0.35	0.11	-0.05	0.07	-304	55	6	DC	6186	13.93	14.32	56.53	82.78	2.7m
14 22 25.73+04 59 39.7	19.34	1.54	0.83	0.30	0.08	0.15	-277	-62	6	DC	4365	15.47	16.37	41.08	55.27	HET
14 26 59.40+49 21 00.6	16.93	0.55	0.18	0.07	-0.09	0.11	-96	44	6	DC	6927	13.43	13.77	44.52	22.28	2.7m
14 52 24.95-00 11 34.7	18.25	1.36	0.58	0.20	0.07	0.27	155	129	6	DC	5052	14.83	15.49	38.98	37.26	2.7m
15 48 35.89+57 08 26.4	17.70	0.80	0.39	0.13	0.05	0.06	-220	-138	6	DC	5975	14.08	14.50	44.38	54.64	2.7m
15 55 34.18+50 25 47.8	16.70	0.75	0.31	0.13	0.00	0.10	-234	-5	6	DA	6204	13.92	14.31	31.13	34.54	2.7m
16 09 20.13+52 22 39.6	18.21	0.65	0.25	0.12	0.01	0.10	155	281	6	DA	6467	13.73	14.09	68.91	104.82	2.7m
16 15 44.67+44 49 42.5	19.56	1.63	0.75	0.27	0.08	0.05	44	-237	6	DC	4698	15.14	15.95	53.41	61.02	HET
16 23 24.05+34 36 47.7	17.18	0.39	0.11	0.08	0.45	0.10	-58	105	6	DA	7650	13.00	13.32	61.11	34.74	2.7m

Object (SDSS J)	g	u-g	g-r	r-i	i-z	$A_u$	$\mu_{ra}$	$\mu_{dec}$	Ep	Type	$T_{\text{eff}}$ (K)	$M_{\text{bol}}$	$M_g$	D (pc)	$V_T$	Source
16 27 12.99+00 28 18.6	17.38	0.78	0.31	0.06	-0.01	0.47	-194	-73	6	DA	5983	14.08	14.49	44.31	43.54	2.7m
16 27 31.09+48 59 19.0	19.19	1.51	0.59	0.24	0.05	0.07	-91	77	6	DZA	5105	14.78	15.43	58.01	32.78	MMT
16 48 47.07+39 39 17.0	18.81	1.29	0.54	0.16	0.06	0.07	-126	0	6	DC	5401	14.53	15.08	56.98	34.03	MMT
16 54 45.70+38 29 36.6	16.93	0.96	0.40	0.15	0.02	0.08	18	-325	5	DZA	5847	14.18	14.62	29.72	45.85	2.7m
16 59 40.00+32 03 20.1	17.56	0.63	0.28	0.07	0.01	0.16	-238	-244	6	DA	6428	13.76	14.12	51.35	82.96	2.7m
17 04 47.70+36 08 47.4	18.63	1.79	0.75	0.28	0.12	0.13	186	-175	6	DC	4560	15.28	16.13	33.21	40.20	HET
17 14 33.26+27 38 36.1	18.16	0.40	0.12	0.01	-0.11	0.24	49	-20	6	DC	7235	13.24	13.57	89.96	22.57	2.7m
17 22 57.78+57 52 50.7	19.17	1.14	0.46	0.23	0.06	0.15	-37	390	6	DC	5403	14.53	15.08	69.64	129.32	HET
17 24 13.32+27 56 55.2	17.47	0.78	0.30	0.11	0.00	0.26	47	-60	6	DA	6131	13.97	14.37	45.61	16.48	2.7m
17 28 07.29+26 46 20.1	18.02	0.97	0.42	0.16	0.04	0.23	-45	-255	6	DA	5619	14.36	14.85	46.57	57.15	2.7m
20 41 28.99-05 20 27.7	19.09	1.65	0.70	0.26	0.06	0.26	-149	-29	6	DC	4673	15.17	15.98	45.68	32.87	MMT
20 42 59.23+00 31 56.6	19.67	1.65	0.81	0.30	0.07	0.37	-71	-244	6	DC	4201	15.63	16.57	47.29	56.96	HET
20 45 06.97+00 37 34.4	19.43	0.59	0.25	0.12	0.00	0.45	32	-32	6	DA	6093	14.00	14.40	117.73	25.25	MMT
20 45 57.53-07 10 03.5	19.08	1.61	0.68	0.21	0.12	0.39	-73	-134	6	DC	4682	15.16	15.97	47.90	34.65	MMT
21 03 30.85-00 24 46.4	18.22	0.66	0.27	0.07	0.02	0.34	61	-139	6	DC	6223	13.91	14.29	68.61	49.36	MMT
21 16 40.30-07 24 52.7	17.93	1.67	0.69	0.25	0.05	0.70	111	-223	6	DC	4359	15.47	16.38	25.89	30.56	2.7m
21 18 05.21-07 37 29.1	19.85	2.42	0.98	0.33	0.11	1.17	115	-144	5	DC	3401	16.55	17.37	43.44	37.95	HET
21 18 58.65+11 20 17.7	18.13	0.77	0.27	0.09	0.01	0.42	359	-13	5	DA	6086	14.00	14.40	64.24	109.38	2.7m
21 25 01.48-07 34 56.0	19.48	0.74	0.26	0.08	0.01	0.56	64	13	5	DA	6063	14.02	14.42	122.54	37.93	MMT
21 36 43.08-07 06 38.2	19.43	0.60	0.25	0.08	-0.03	0.20	69	-11	5	DA	6520	13.70	14.05	125.93	41.71	MMT
21 47 52.10-08 24 36.8	17.59	0.75	0.32	0.14	-0.01	0.24	30	153	6	DA	6010	14.06	14.47	45.77	33.82	2.7m
21 54 30.69+13 00 26.7	18.75	1.55	0.61	0.25	0.10	0.41	367	-73	6	DZA	4768	15.08	15.86	43.76	77.62	MMT
21 55 01.53+12 01 16.4	18.47	0.65	0.25	0.07	-0.06	0.54	-76	-25	4	DA	6121	13.98	14.37	79.14	30.01	MMT
22 04 14.16-01 09 31.2	19.88	1.88	0.83	0.24	0.11	0.44	112	-303	6	DC	4189	15.65	16.58	52.87	80.95	HET
22 22 33.90+12 21 43.0	19.13	1.95	1.02	0.36	0.18	0.41	731	198	4	DC	3448	16.49	17.33	25.78	92.53	HET
22 41 57.63+13 32 38.8	17.36	0.82	0.35	0.10	0.02	0.26	61	-395	6	DA	5986	14.07	14.49	40.90	77.49	2.7m
22 42 06.19+00 48 22.8	19.38	2.43	0.91	0.34	0.08	0.36	132	-76	6	DC	3407	16.55	17.37	29.12	21.02	HET
22 54 08.64+13 23 57.2	19.33	2.04	0.97	0.33	0.10	0.26	329	-199	6	DC	3356	16.61	17.41	26.72	48.71	HET
23 12 06.08+13 10 57.6	17.45	1.38	0.56	0.16	0.08	0.38	-132	-256	6	DA	5078	14.80	15.46	28.40	38.78	2.7m
23 25 19.89+14 03 39.7	16.30	1.55	0.57	0.27	0.09	0.23	336	115	6	DC	4941	14.92	15.63	14.80	24.92	2.7m
23 30 40.47+01 00 47.4	17.36	0.64	0.17	0.06	0.02	0.20	-255	-125	6	DA	6768	13.54	13.88	53.63	72.19	2.7m
23 30 55.20+00 28 52.3	19.77	1.96	0.89	0.30	0.11	0.17	151	91	6	DC	4126	15.71	16.65	44.42	37.12	HET
23 37 07.68+00 32 42.3	18.13	1.01	0.45	0.14	-0.02	0.18	305	162	6	DA	5629	14.35	14.84	48.35	79.15	2.7m
23 40 41.47-11 06 36.9	18.46	0.53	0.25	0.74	0.85	0.15	19	-87	6	DA+M	6612	13.64	13.99	82.58	34.86	MMT
23 42 45.75-10 01 21.4	18.83	1.52	0.71	0.26	0.04	0.16	-28	-95	6	DA	4719	15.12	15.92	40.18	18.86	MMT
23 50 42.52-08 46 18.9	19.03	1.04	0.50	0.22	0.08	0.18	209	-139	6	DA	5298	14.61	15.20	62.18	73.97	HET
23 54 16.59+00 30 01.2	19.25	0.71	0.20	0.10	0.04	0.20	53	18	5	DA	6568	13.67	14.02	119.10	31.60	MMT

Table 2.4: Spectroscopically Identified Subdwarf Stars

Object (SDSS J)	g	u-g	g-r	r-i	i-z	$A_u$	$\mu_{ra}$	$\mu_{dec}$	Ep	Dist22
00 18 13.74-08 54 58.6	19.48	0.73	0.24	0.07	-0.03	0.23	-41	-33	5	15.1
00 29 58.84+15 18 41.1	19.20	0.84	0.29	0.08	0.07	0.34	-46	-31	4	30.4
00 53 31.26+00 05 09.8	19.38	2.18	1.09	0.53	0.23	0.13	137	-22	6	24.4
01 05 02.05+14 01 54.4	19.40	1.00	0.43	0.15	0.08	0.37	-11	48	5	25.4
01 31 19.61+00 02 57.6	17.93	2.18	1.14	0.45	0.25	0.17	230	-115	6	31.0
01 48 33.19-01 10 43.3	17.98	1.91	0.85	0.36	0.15	0.17	152	-106	6	13.8
01 56 32.67+14 47 29.7	17.48	1.52	0.66	0.27	0.07	0.29	111	-95	5	7.8
02 12 13.80+00 00 42.1	18.81	1.33	0.51	0.21	0.10	0.16	81	61	5	12.9
02 29 47.61-08 50 20.2	16.80	1.62	0.74	0.24	0.14	0.17	151	-95	6	6.4
02 38 07.99-09 30 33.6	18.61	1.87	0.77	0.30	0.19	0.15	80	-46	6	29.4
03 00 48.83-00 44 08.0	17.21	1.20	0.60	0.26	0.19	0.60	83	-113	6	12.6
03 07 22.43+00 34 05.2	15.68	1.18	0.49	0.18	0.08	0.55	156	-109	6	41.2
03 10 43.74-08 18 48.7	17.49	0.86	0.25	0.08	0.03	0.36	-32	48	5	13.4
03 18 45.08-06 12 36.3	16.56	1.51	0.73	0.28	0.18	0.33	159	-104	6	35.0
03 51 47.74-05 33 02.9	15.94	1.54	0.74	0.28	0.12	0.56	237	-264	6	31.9
07 36 36.05+29 02 22.7	17.41	1.11	0.34	0.13	0.05	0.24	-18	-71	5	4.6
07 38 56.39+32 25 18.9	17.52	1.73	0.80	0.33	0.16	0.22	5	-144	6	17.0
07 52 17.25+25 21 55.6	16.79	1.03	0.27	0.07	0.00	0.40	146	214	4	26.2
08 00 05.13+46 08 01.1	16.64	1.13	0.55	0.16	0.11	0.38	-2	309	4	19.6
08 13 06.76+02 34 25.9	17.15	1.30	0.45	0.19	0.09	0.14	309	-45	5	7.7
08 30 49.85+02 50 18.6	18.24	1.55	0.53	0.12	0.12	0.17	45	87	6	5.5
08 37 43.43+02 01 01.7	17.91	2.14	0.78	0.30	0.11	0.25	-15	-443	4	5.5
09 05 13.97+47 37 28.5	18.67	2.79	1.33	0.51	0.31	0.08	-159	-344	6	35.1
09 19 09.52+56 41 00.1	17.03	2.09	0.70	0.24	0.14	0.17	1	-263	5	10.0
09 35 59.33+60 13 23.0	17.22	1.40	0.55	0.25	0.09	0.15	-4	-275	4	11.3
09 59 26.92-00 08 49.7	16.82	2.03	0.79	0.31	0.09	0.16	-315	90	5	6.0
10 05 37.72+52 59 13.2	17.30	0.95	0.24	0.08	-0.01	0.04	-3	131	5	12.1
10 06 33.59-00 27 32.4	17.95	1.01	0.47	0.16	0.08	0.19	-237	-72	5	4.1
10 17 39.82+02 09 33.8	16.79	1.40	0.59	0.21	0.12	0.25	-240	190	4	16.5
10 41 49.72+62 44 55.6	16.69	0.98	0.29	0.08	0.05	0.03	55	161	5	12.2
10 51 57.48+02 03 00.4	19.74	1.97	1.05	0.46	0.28	0.22	166	-105	5	32.0
11 07 23.94+62 26 06.0	16.29	0.97	0.33	0.11	0.03	0.05	46	239	4	25.4
11 13 27.37+58 58 48.5	17.09	2.32	1.24	0.48	0.31	0.05	-296	-472	6	59.0
11 22 04.68+65 53 59.7	17.54	1.08	0.36	0.17	0.04	0.06	-63	-152	5	39.5
11 31 02.89+66 57 51.2	16.66	1.64	0.52	0.25	0.11	0.05	-116	206	5	42.9
11 35 12.08+03 28 41.2	19.24	2.80	1.18	0.47	0.31	0.11	-163	-255	6	20.1
11 52 06.86+67 02 04.2	16.33	0.87	0.21	0.08	0.02	0.06	-117	143	4	19.8
12 09 45.96+63 02 43.9	16.96	0.86	0.25	0.08	0.01	0.10	-71	196	5	26.5
12 50 47.35+03 26 52.8	18.28	2.17	0.98	0.43	0.19	0.16	-97	-221	4	12.5
12 52 26.29+02 28 38.8	16.78	1.44	0.49	0.16	0.05	0.16	155	-100	5	19.1
13 05 07.26+04 14 08.1	16.81	0.92	0.32	0.12	0.02	0.13	-135	-47	5	9.3
13 42 33.44+58 00 19.7	17.16	1.08	0.32	0.13	0.04	0.04	15	196	5	15.7
14 06 35.95+61 53 35.6	19.70	1.96	1.03	0.42	0.25	0.07	-84	296	5	36.2
16 37 16.86+45 17 01.8	17.79	0.95	0.33	0.08	0.05	0.06	-83	-414	4	13.6
17 02 06.35+31 47 49.9	17.71	1.57	0.58	0.19	0.13	0.21	246	-99	5	9.6
17 17 37.03+62 34 48.1	18.26	1.10	0.32	0.16	0.00	0.12	-36	43	6	28.5
17 19 18.54+29 15 38.6	17.52	1.55	0.59	0.14	0.08	0.20	72	142	5	11.1
17 35 52.77+57 38 14.3	17.88	2.07	1.00	0.40	0.19	0.33	-89	156	6	20.0
20 58 59.24-05 57 03.8	19.16	1.51	0.59	0.19	0.08	0.23	-51	51	4	12.1
21 34 27.61-08 15 11.0	18.41	1.34	0.49	0.15	0.08	0.18	-75	19	5	23.0
21 42 39.11-00 55 50.3	18.69	2.41	1.19	0.47	0.26	0.27	103	-173	6	13.6
21 48 19.02+00 39 43.2	18.30	0.99	0.35	0.10	0.01	0.81	-55	79	6	9.7
22 14 28.87+13 53 41.9	17.66	1.04	0.39	0.14	0.06	0.33	90	50	6	8.7
22 54 49.68+12 59 22.6	19.23	1.75	1.00	0.31	0.21	0.20	226	-125	5	7.2
22 58 03.60-10 07 02.0	19.33	2.73	1.08	0.57	0.29	0.20	108	-145	6	28.8

cations. Again, this is limited to stars with reliable proper motions; that is, stars detected in all 5 USNO-B epochs and with no neighbor brighter than  $g = 22$  within  $7''$ . There is a clean separation between the white dwarfs and subdwarfs. Of the 95 spectroscopically confirmed stars bluer than  $g - i = 1.5$  and below the  $V_T = 20 \text{ km s}^{-1}$  curve, corresponding to the region we expect to find only white dwarfs, 91 are certain white dwarfs, 2 are certain subdwarfs, and two are probable white dwarfs for which a classification of subdwarf can not be ruled out. Visual inspection of the plate images reveals that the two subdwarfs had falsely measured large proper motions, consistent with the contamination rate derived earlier for our adopted reliable proper motion criteria, while the two probable white dwarfs had correctly measured proper motions.

We also observed stars that did not meet our criteria for a reliable proper motion, having either not been detected in 1 or 2 USNO-B epochs or having a neighbor within  $7''$ . Of these, 16 were white dwarfs (plotted as blue asterisks in Figure 2.9), all located within the white dwarf region of the RPM diagram; upon visual inspection of the plates used in USNO-B, all of the measured proper motions were correct. Another 37 were subdwarfs (see Table 2.4), located both in the white dwarf and subdwarf regions of the RPM diagram; visual inspection shows all but three of these to have incorrectly measured proper motions, and the proper motions of the remaining three were too small to determine their validity by eye.

The RPM diagram, using our conservative criteria for a reliable proper motion, can thus be used to define a statistically complete sample of white dwarfs, including the coolest white dwarfs which are difficult to efficiently select using other techniques. There is a roughly 1.5% contamination rate due to incorrectly measured proper motions. There is likely no contamination due to subdwarfs with correctly measured proper motions, though contamination of a few percent is still possible. True white dwarfs that fail to meet the proper motion criteria must be accounted

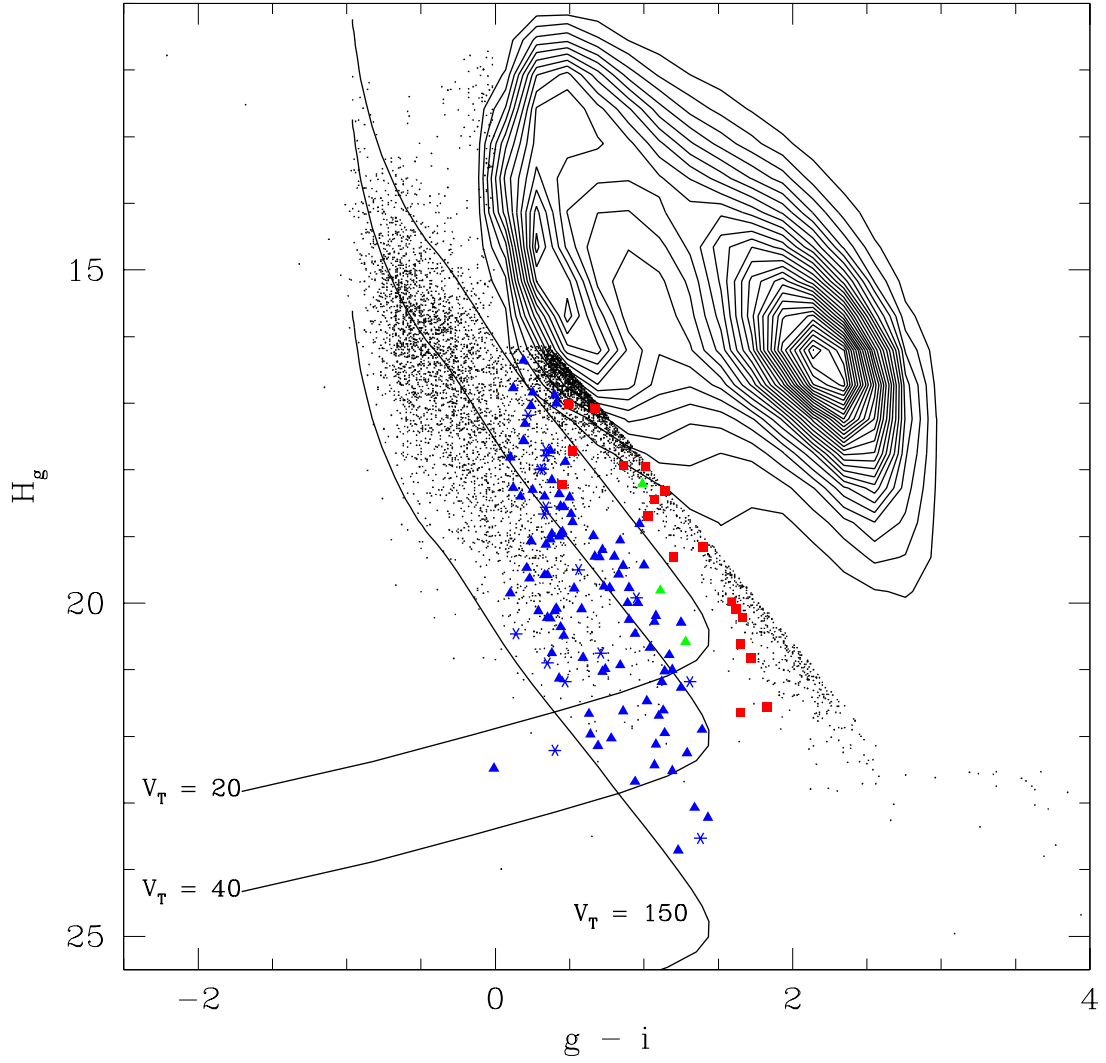


Figure 2.9: Same as figure 2.6, but for the spectroscopically confirmed white dwarfs, white dwarf + late type star binaries, subdwarfs, and quasars found in our study. White dwarfs that did not meet our criteria for reliable proper motions are plotted as blue asterisks.

for, either statistically or by using visual inspection to verify proper motions for all candidates. This result is used in Harris et al. (2006) to construct the white dwarf luminosity function using the SDSS Data Release 3 imaging and USNO-B astrometry.

### Color-Color Diagrams

SDSS color-color diagrams for spectroscopically identified proper motion objects are shown in Figure 2.10. The spectral classifications are indicated in the diagrams, and contours that show the colors of nondegenerate stars in the SDSS are included for comparison. The curves show the colors of white dwarf model atmospheres of pure H (solid curves) and pure He (dashed curves) composition with  $\log g = 7, 8$ , and  $9$ , kindly made available to us by P. Bergeron.

Figure 2.10 shows that the cool white dwarf model atmospheres cannot predict the  $u - g$  colors below 6,000 K accurately, though the  $g - r$ ,  $r - i$ , and  $i - z$  colors agree reasonably well with the observed sequence of cool white dwarfs. Bergeron et al. (1997) were the first to introduce a UV opacity source in the coolest hydrogen-rich white dwarf models in terms of a pseudo continuum opacity to fit the observed hydrogen-rich cool white dwarf sequence. They found that this opacity source is needed to explain the observed UV colors of cool hydrogen-rich white dwarfs below 5,300 K. This is also seen in the  $B - V$  versus  $V - K$  color-color diagram of Bergeron et al. (2001), and our  $r - \text{DDO51}$  vs.  $r - z$  color-color diagram in Figure 2.4. Wolff, Koester, & Liebert (2002) showed that this UV flux deficiency (relative to model atmosphere predictions) extends even more strongly into the space ultraviolet region (2000 – 3200 Å). Here, we find that the  $u - g$  colors for neither cool DA nor cool DC white dwarfs can be explained with the current model atmospheres. Significant improvements are needed in the cool white dwarf model atmospheres to understand the unexplained UV opacity which is crucial for the coolest white dwarfs (Bergeron

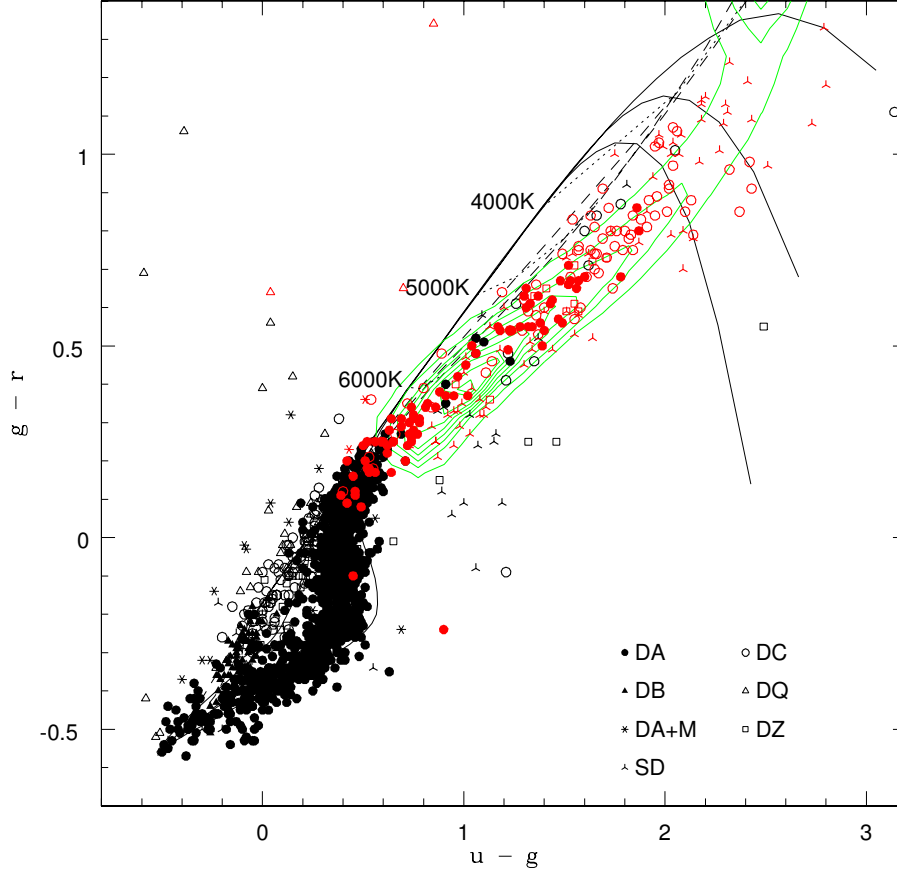


Figure 2.10: Color-color diagrams showing the white dwarfs and subdwarfs from our study (red symbols) and the literature (black symbols). Different types of white dwarfs are shown with different symbols. The contours represent objects without spectroscopic confirmation. The curves show the colors of white dwarf model atmospheres (P. Bergeron, private communication) of pure H (solid curves) and pure He (dashed curves) with  $\log g = 7, 8$ , and  $9$ , where the  $\log g = 9$  curve is the bottom and  $\log g = 7$  is the top curve. The dotted lines with labels connect models with the same effective temperature.

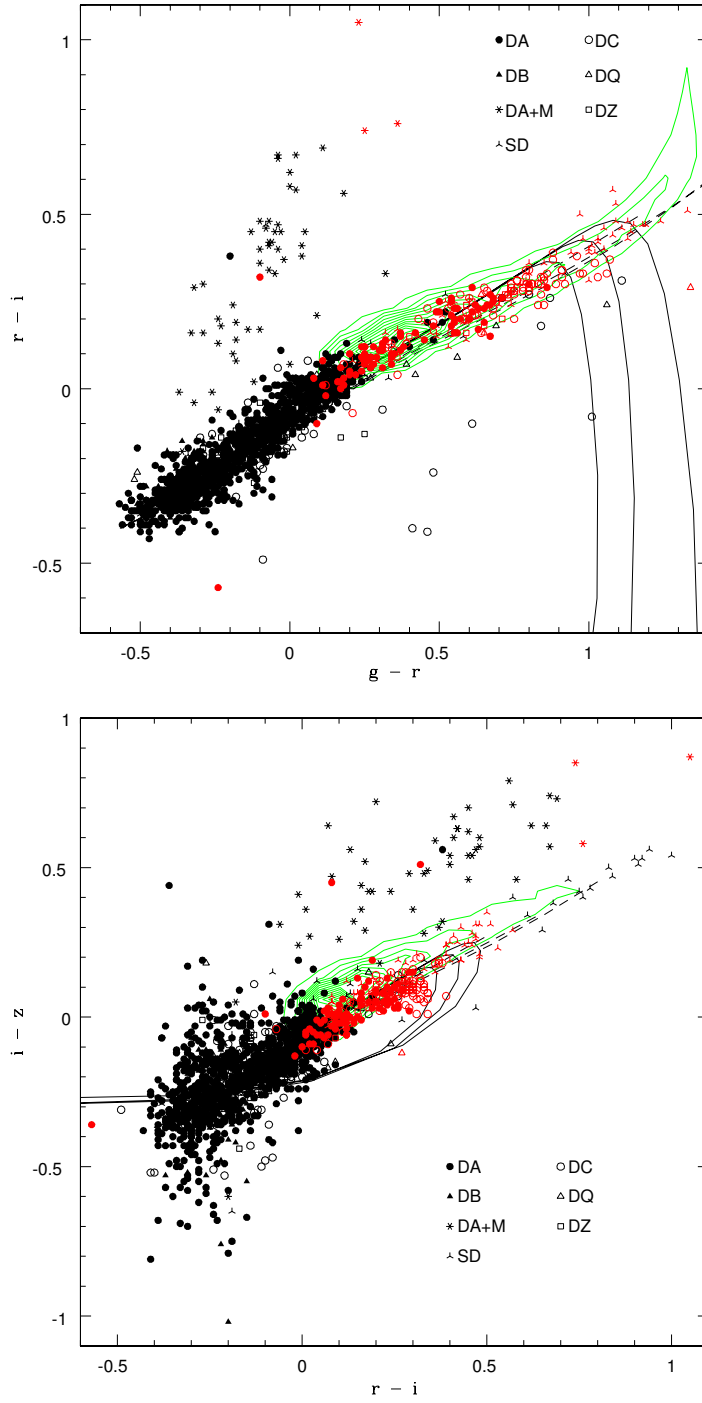


Figure 2.10: Continued

2001).

The majority of the cool white dwarfs with  $r - i > 0.25$  ( $T_{\text{eff}} < 5000$  K) tend to have bluer  $i - z$  colors compared to the model predictions; the observed blue turn-off of cool white dwarfs is at a bluer color than expected from the models. Most of the cool white dwarfs occupy a region to the left of the  $\log g = 9$  (left-most line) white dwarf models. This implies that either all of the very cool white dwarfs are massive, they have mixed H/He atmospheres, or our understanding of the CIA opacities are incomplete. For all these white dwarfs to be massive is statistically unlikely as the average mass for the cool white dwarfs ( $T_{\text{eff}} \leq 5000$  K) with trigonometric parallax measurements is  $0.61 \pm 0.2 M_{\odot}$  (Bergeron et al. 2001). Mixed atmosphere white dwarfs are expected to show stronger flux deficits in the infrared than pure H white dwarfs (Bergeron, Saumon, & Wesemael 1995), which could explain the observed blue turn-off of cool white dwarfs in Figure 2.10. Bergeron & Leggett (2002) argued that white dwarfs cooler than 4000 K have mixed H/He atmospheres. In addition, Kilic et al. (2004b) suggested that all white dwarfs cooler than 5000 K may have mixed atmospheres. Therefore, this figure presents further evidence that the coolest white dwarfs indeed have mixed atmospheres.

### Non-DA Gap

The  $H\alpha$  and  $H\beta$  equivalent widths of all DA and DC white dwarfs in our sample are shown against  $g - r$  in Figure 2.11. White dwarf models predict  $H\alpha$  to disappear around  $V - I \sim 1.1$  (see Figure 7 of Bergeron et al. 1997). Although there is a large scatter in our equivalent width measurements in this figure, it is apparent that the  $H\alpha$  and  $H\beta$  equivalent widths decrease with increasing  $g - r$  color and they vanish around  $g - r \sim 0.7$  (or  $V - I \sim 1.1$ ), in good agreement with the model predictions. The scatter in the equivalent width measurements may partly be due to variations in gravities and the use of spectra with different signal-to-noise ratios from four

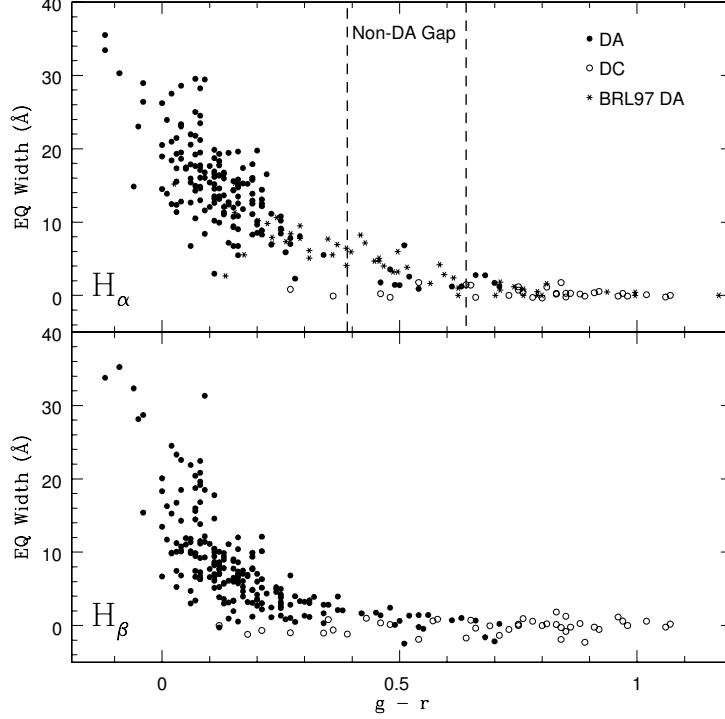


Figure 2.11: Equivalent width measurements of  $H\alpha$  and  $H\beta$  as a function of  $g - r$  for the DA and DC white dwarfs in our sample. The top panel also includes  $H\alpha$  equivalent width measurements of the Bergeron et al. (1997) DA sample. The predicted non-DA gap for  $\log g = 8$  DA white dwarfs is marked by the dashed lines. Since McDonald 2.7m spectra do not cover  $H\alpha$ , we do not have  $H\alpha$  equivalent width measurements for some of our objects.

different telescope + instrument combinations.

Bergeron et al. (1997; 2001) argued that most of the white dwarfs with  $T_{\text{eff}}$  in the range 6000 K – 5000 K are of DA type, and they found evidence for a so-called non-DA gap. Even though non-DA stars are seen above and below this temperature range, they found only two peculiar non-DA stars inside the gap. Bergeron et al. (1997), Bergeron et al. (2001), and Hansen (1999) tried to explain the existence of this gap in terms of different physical mechanisms, i.e. convective mixing and

different evolutionary timescales of hydrogen-rich and helium-rich white dwarfs. The existence of the non-DA gap is apparent in Bergeron et al.'s (2001)  $V - I$  vs.  $V - K$  color-color diagram. Figure 2.12 shows  $u - g$  vs.  $g - r$  (left panel),  $g - r$  vs.  $r - i$  (middle panel), and  $r - i$  vs.  $i - z$  (right panel) color-color diagrams for white dwarfs in our sample. The data set is divided into DA (upper panels) and non-DA (lower panels, DC and DQ) stars. The pure H (DA panels) and pure He (non-DA panels) model sequences with  $6000 \text{ K} \geq T_{\text{eff}} \geq 5000 \text{ K}$  are also shown for  $\log g = 7$  (solid line),  $\log g = 8$  (dotted line), and  $\log g = 9$  (dashed line). The two differences between these color-color diagrams and Figure 2.10 are that (1) DC white dwarfs discovered at the McDonald 2.7m are not included in Figure 2.12 since the 2.7m spectra do not cover  $\text{H}\alpha$ , and so some of the white dwarfs observed with the 2.7m and classified as DCs may turn out to be DAs showing  $\text{H}\alpha$  only, and (2) ultra-cool white dwarfs discovered in the SDSS are not included. SDSS J1001+3903, an ultra-cool white dwarf discovered by Gates et al. (2004), falls in the non-DA gap in the  $u - g$  vs.  $g - r$  diagram, but not in the other two diagrams. Even though ultra-cool white dwarfs are expected to have  $T_{\text{eff}} \leq 4000 \text{ K}$ , they can mimic bluer/warmer objects in the various color-color diagrams and therefore are not included in this discussion.

DA white dwarfs show  $\text{H}\alpha$  absorption for  $g - r \leq 0.7$  ( $\geq 5000 \text{ K}$ ) and we should have detected  $\text{H}\alpha$  for DCs with  $6000 \text{ K} \geq T_{\text{eff}} \geq 5000 \text{ K}$  if they had pure H atmospheres. The  $\text{H}\alpha$  panel in Figure 2.11 shows exactly 3 DC stars in the gap (The gap, marked by the dashed lines, is  $g - r = 0.39$  to  $0.64$  for hydrogen atmospheres). Based on  $ugriz$  photometry (Figure 2.12), we see DC stars above and below the non-DA gap, but we find only 3 to 5 DC stars (shown as filled red circles in lower panels) in the gap. All of these white dwarfs (SDSS J0157+1335, J1203+0426, J1205+0449, J1648+3939, J1722+5752) are observed at the MMT and HET, and Balmer lines cannot be seen in their spectra. Assuming pure He composition, we

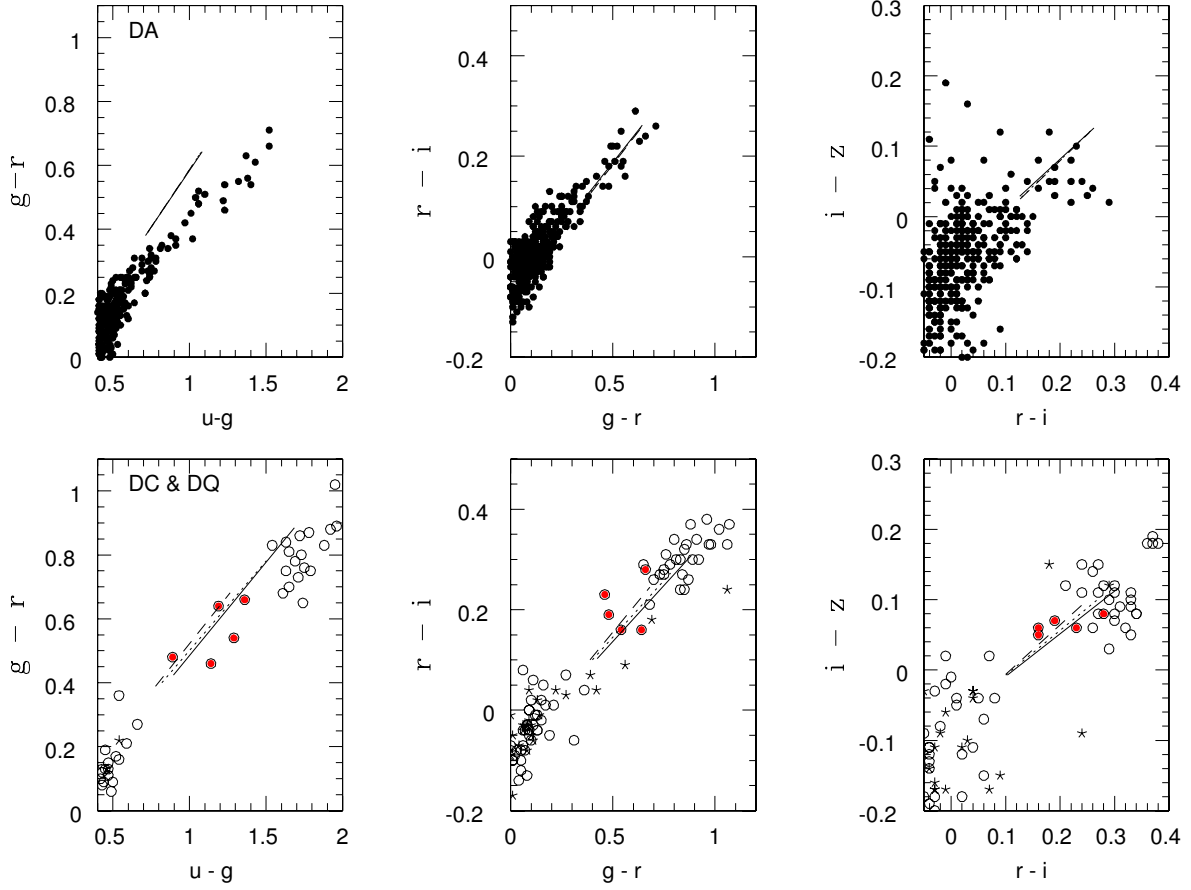


Figure 2.12: The  $u-g$  vs.  $g-r$  (left panel),  $g-r$  vs.  $r-i$  (middle panel), and  $r-i$  vs.  $i-z$  (right panel) color-color diagrams for white dwarfs in our sample. Upper panels show DA white dwarfs, whereas lower panels show DC (open circles) and DQ (star symbols) white dwarfs. The pure H (DA panels) and pure He (non-DA panels) model sequences with  $6000 \text{ K} \geq T_{\text{eff}} \geq 5000 \text{ K}$  are also shown for  $\log g = 7$  (solid line),  $\log g = 8$  (dotted line), and  $\log g = 9$  (dashed line). Probable DC white dwarfs in the non-DA gap are shown as filled red circles.

estimate their temperatures to be 5254 K, 5144 K, 5635 K, 5536 K, and 5555 K (see the next section for temperature estimates). These stars appear to be non-DA stars in the 5000-6000K temperature range, and fill in the Bergeron et al non-DA gap to some extent. The fraction of DA/non-DA stars in this temperature range is still seen to be large in our data, and further data are needed to quantify the ratio. Moreover, Bergeron et al. (1997) have identified a group of DC white dwarfs which lie close to  $T_{\text{eff}} = 6000$  K whose energy distributions are better reproduced with pure hydrogen models. Therefore, some or all of these stars may be explained with H-rich compositions. Bergeron et al. (2001) and Ruiz & Bergeron (2001) showed that infrared photometry is needed to discriminate between hydrogen-rich and helium-rich atmospheres for cool white dwarfs; infrared photometry is needed to reliably determine the atmospheric composition and temperatures for these stars. In any case, our data supports at least a deficit in the number of non-DA white dwarfs in the non-DA gap observed by Bergeron et al. (1997; 2001).

### Model Atmosphere Analysis

The  $u, g, r, i$ , and  $z$  photometry for each of the new spectroscopically confirmed white dwarfs has been fitted with synthetic photometry calculated from model atmospheres (P. Bergeron, private communication), using a minimum  $\chi^2$  fit. Since trigonometric parallax measurements are not available for these white dwarfs, a value of  $\log g = 8.0$  has been assumed for all objects. Due to larger uncertainties in  $u$  and  $z$ , and the fact that the  $u$  magnitudes of cool white dwarfs are affected by an unexplained UV opacity source,  $u$  and  $z$  magnitudes are given lower weight in our fits. The fits have been done using only  $u, g$ , and  $r$  magnitudes for white dwarf + late type star binaries, though some of these binaries may have contaminated  $u, g$ , and  $r$  magnitudes.

While spectra of bluer white dwarfs allow us to determine whether the at-

mosphere is hydrogen-rich or helium-rich,  $H\alpha$  and  $H\beta$  disappear around  $g - r \sim 0.7$  and so IR photometry is needed to determine the atmospheric composition for DCs. We assume hydrogen-rich composition for the analysis of all of the DA and DC white dwarfs in our sample. Both hydrogen-rich and helium-rich models give similar answers for stars with  $T_{\text{eff}}$  in the range 10000 – 5500 K ( $g - i < 0.7$ ), though the difference in temperature estimates drastically increases below 5500K due to the onset of collision induced absorption. Pure He models predict warmer temperatures than the pure H models; the optical colors of a 4000 K pure H atmosphere white dwarf can be fit with a 4700 K pure He white dwarf model.

We assumed zero reddening for white dwarfs with estimated distances  $\leq 100$  pc, and used the full reddening value from Schlegel, Finkbeiner, & Davis (1998) if the estimated distance from the Galactic plane is larger than 250 pc. For white dwarfs with estimated distances between 100 and 250 pc, we used a linear interpolation between zero and the full reddening coefficient.

Results of the model atmosphere fits are summarized in columns 12–16 of Table 2.3. For each white dwarf, we give (assuming pure H composition with  $\log g = 8.0$ ) the effective temperature, the predicted bolometric magnitude, the absolute magnitude in  $g$ , the distance, and the estimated tangential velocity. According to our fits, there are seven white dwarfs with  $T_{\text{eff}} \leq 4000$  K in our sample, but these temperature estimates are questionable, and near-IR photometry is needed to obtain reliable results for these objects. Although most of the newly found white dwarfs show disk kinematics, there are 16 objects with  $V_T \geq 150 \text{ km s}^{-1}$  that may be halo white dwarfs. Halo membership of these objects and several others from the SDSS Data Release 3 are discussed in Harris et al. (2006).

## 2.4 A New White Dwarf Luminosity Function

We showed in the previous section that white dwarfs occupy a locus in the RPM diagram, cleanly separated from most subdwarfs, and that samples of white dwarfs can be defined using the RPM diagram with contamination by subdwarfs and QSOs of only a few percent. Harris et al. (2006) used this result to create statistically complete catalogs of white dwarfs. A sample of white dwarfs is defined by taking all stars below and blueward of one of the model curves (for example, the  $V_{\text{tan}} = 30 \text{ km s}^{-1}$  curve for pure-H atmosphere white dwarfs). Using  $V_{\text{tan}}$  cutoffs of 20, 30, and 40  $\text{km s}^{-1}$  yields samples of 7116, 6000, and 4501 stars, respectively.

### 2.4.1 Construction of a Luminosity Function

The luminosity function is calculated based on temperatures, absolute magnitudes, and distances to each star derived from the model atmosphere analysis described in the previous section. The Galactic disk scale height of the white dwarf population must be known before deriving the luminosity function, because luminous white dwarfs near the SDSS magnitude limit are at distances of several hundred pc from the Galactic plane where their space density is significantly reduced. Harris et al. (2006) adopted the commonly used value of the scale height of the disk, 250 pc. They also used a tangential velocity limit of 30  $\text{km s}^{-1}$  in order to minimize the contamination from subdwarfs. The luminosity function is derived from the list of identified white dwarfs by using the  $1 / V_{\text{max}}$  method (summing the inverse volume of space in which each star potentially would have been included within the sample limits and calculating each luminosity bin separately; see Geijo et al. 2006). The new white dwarf luminosity function is shown in Figure 2.13.

The new luminosity function is remarkably smooth and featureless. The only noticeable feature in the range  $8 < M_{\text{bol}} < 15$  is the small plateau near  $M_{\text{bol}} = 10.5$ . The ZZ Ceti instability strip is at slightly fainter  $M_{\text{bol}}$ , so it is probably not related

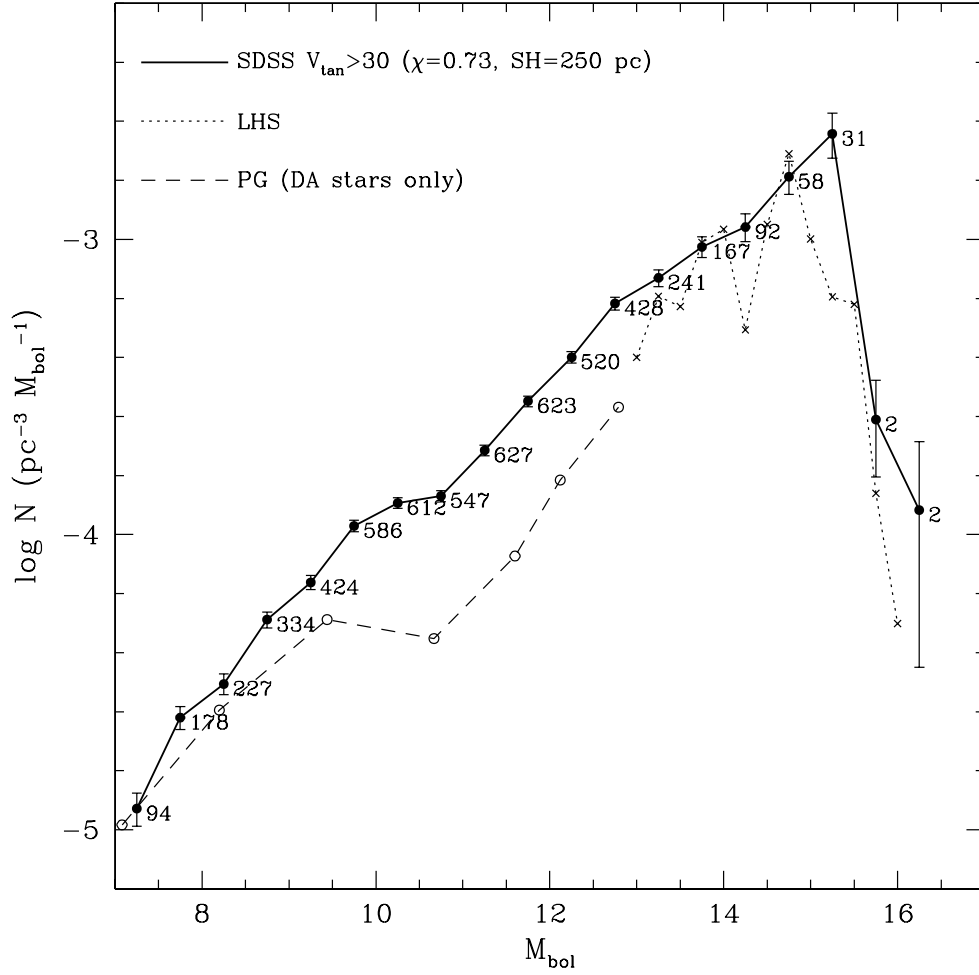


Figure 2.13: The white dwarf luminosity function from SDSS Data Release 3 (Harris et al. 2006). The number of stars used for each data point is indicated. Two results from the literature are shown for comparison: the dotted line at the faint end is taken from Leggett et al. (1998), based on the LHS Catalog; the dashed line at the bright end is taken from Liebert et al. (2005), based on analysis of the PG Survey, including DA white dwarfs only.

to this feature. The feature could be an artifact caused by incorrect models of stars near this temperature, which could in turn cause incorrect photometric distances to be assigned and/or cause incorrect values of  $M_{\text{bol}}$  to be assigned. However, the models are believed to be quite accurate in this temperature range. No feature is predicted (Fontaine et al. 2001) from a pause in white dwarf cooling and dimming. If the feature is real, it could reflect a nonuniform rate of production of white dwarfs in the Galactic disk. The cooling time for a normal-mass white dwarf to reach  $M_{\text{bol}} \sim 10.5$  is 0.3 Gyr, and the main-sequence lifetime of a likely progenitor is  $\sim 2.5$  Gyr, suggesting that a drop in star formation about 3 Gyr ago (after a burst or a long-duration higher rate of star formation) might be the cause of the plateau seen in Figure 2.13.

The result at the bright end is in acceptable agreement with results from the hydrogen-rich (DA) stars from the Palomar-Green (PG) survey (Liebert et al. 2005). Accounting for non-DA stars, as was done by Leggett et al. (1998), will raise the densities from the PG survey by a small amount. The PG survey gives densities in agreement with SDSS results for  $7 < M_{\text{bol}} < 10$ , but smaller than SDSS by factors of 2–3 for  $10 < M_{\text{bol}} < 13$  or  $11.3 < M_V < 13.2$ . This is exactly the range where Liebert et al. (2005) suspect the PG-survey results are incomplete.

The result at the faint end is in excellent agreement with that from the local sample selected from the LHS Survey (Leggett et al. 1998). The abrupt drop in the luminosity function occurs at  $M_{\text{bol}} = 15.40$  (for a  $0.6M_{\odot}$  pure H atmosphere white dwarf, this corresponds to an age of 7.8 Gyr; Bergeron et al. 1995), although the exact shape of the drop and the exact luminosity at which it occurs both depend on the unknown H/He type of white dwarfs in this sample. Also evident in this plot is a rise in the luminosity function at  $M_{\text{bol}} = 15.1\text{--}15.2$ . This rise appears to be marginally significant. It is at a luminosity consistent with the predicted onset of convective coupling between the convective hydrogen atmosphere and the degenerate

core (Fontaine et al. 2001) causing temporary additional release of internal energy and delayed cooling. Observationally, the rise in this figure, like the following drop, is sensitive to the assumptions on H/He types and to the luminosity of the coolest stars. We are obtaining near-infrared photometry of these stars at the NASA Infrared Telescope Facility and Gemini-North in order to verify the reality and exact shape of this feature.

The integral of the Harris et al. luminosity function in Figure 2.13 gives a space density of white dwarfs in the solar neighborhood of  $0.0046 \pm 0.0005 \text{ pc}^{-3}$ . The assumptions about the scale height and the fraction of He-atmosphere stars affect this result, but not drastically. The space density is somewhat higher than found by Leggett et al. (1998),  $0.0034 \text{ pc}^{-3}$ , but consistent with that found by Holberg et al. (2002),  $0.0050 \text{ pc}^{-3}$ .

Assuming that all the high-velocity candidates are halo stars, Harris et al. (2006) constructed a luminosity function. Figure 2.14 shows the luminosity function using the restricted sample of 32 high-velocity white dwarfs for three different  $V_{\text{tan}}$  cutoffs. The fact that the luminosity function derived using the higher cutoffs does not drop much suggests that the sample is not dominated by a rapidly dropping high-velocity tail of the thick disk or the thin disk. However, the sample can have significant numbers of runaway white dwarfs from the thin disk or thick disk that have acquired a velocity kick somehow, and therefore do not follow the velocity distributions assumed in the models. Therefore, the luminosity function in this figure should be considered as an upper limit for the halo until the actual composition of the sample is better understood. The shape of the luminosity function (rising toward lower luminosities) and the integrated space density ( $4 \times 10^{-5} \text{ pc}^{-3}$ ) are both consistent with models of an old, single-burst population (e.g. Hansen 2001).

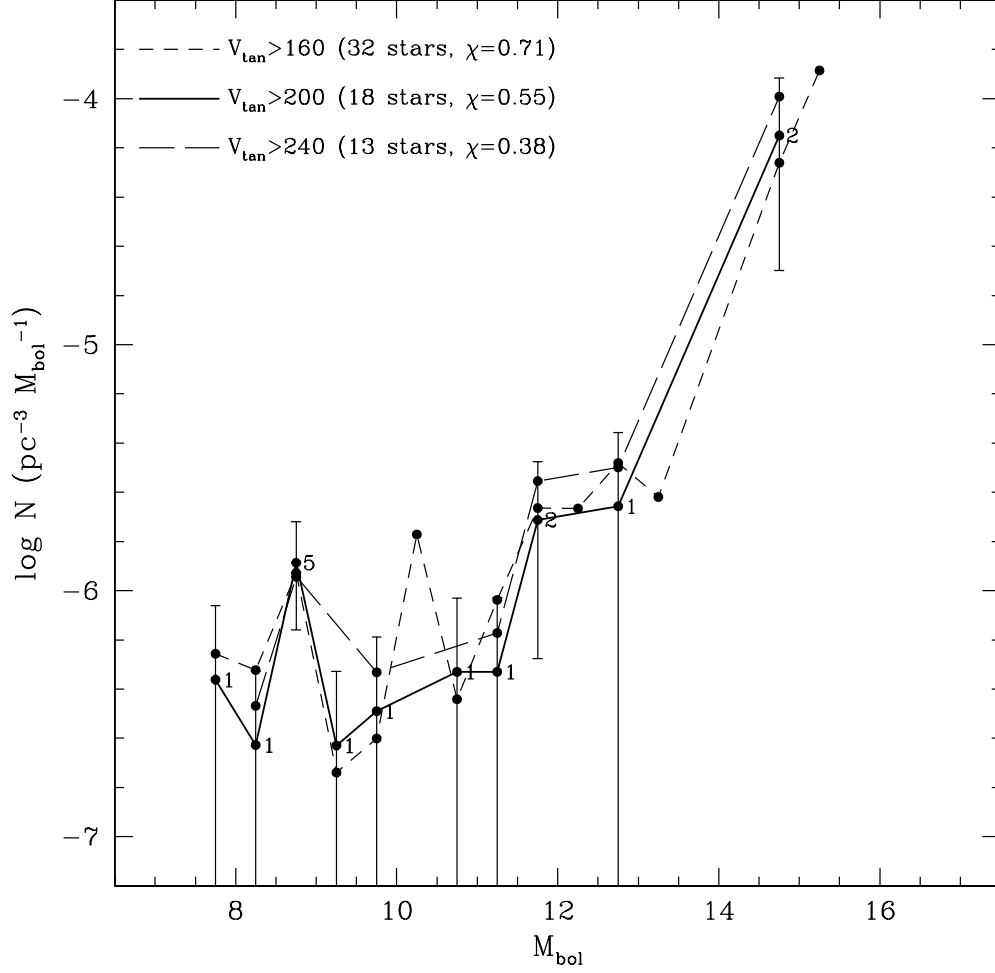


Figure 2.14: A preliminary luminosity function for high-velocity white dwarfs. The three curves show the luminosity function using different selection limits of tangential velocity, and after correction for incompleteness using the values listed as  $\chi$ . The sample may be dominated by halo white dwarfs, but probably includes some fractions of disk, thick-disk, and high-mass white dwarfs.

## 2.5 Conclusion

We have succeeded in creating a large sample of cool white dwarfs including 6000 stars from the SDSS. Harris et al. (2006) used this sample to create a new white dwarf luminosity function, and found that the luminosity function rises monotonically until it drops abruptly at about  $M_{\text{bol}} \sim 15.4$  ( $\tau_{\text{cooling}} \sim 7.8$  Gyr). Due to the lack of near-infrared photometry for our sample, we cannot determine the exact shape of the faint end of the luminosity function right now. However, our results are consistent with the analysis of Leggett et al. (1998), which found the age of the Galactic disk to be  $8 \pm 1.5$  Gyr. Our Gemini and the IRTF observations will be completed by the end of 2006 which will enable us to improve the faint end of the new luminosity function.

To first order, our preliminary luminosity function for the Galactic halo shows that the halo is older than the Galactic disk. Nevertheless, we have only detected the bright end of the halo luminosity function, and the age of the halo cannot be determined from our sample of 32 stars. Hansen et al. (2004) and Richer et al. (2006) presented age estimates for the globular clusters M4 and NGC 6397 based on their respective white dwarf sequences and found that these two clusters are about 12 Gyr old. Our preliminary luminosity function for the halo is qualitatively consistent with the results from the globular cluster age estimates.

Our efforts to create a larger sample of halo white dwarfs will be further discussed in Chapter 6.

## Chapter 3

# The Mystery Deepens: Mid-infrared Observations of White Dwarfs

*“The job of the artist is to deepen the mystery.”*

*– Francis Bacon, Sr.*

The previous chapter focused on the use of white dwarfs as cosmic chronometers. We usually observe white dwarfs in the optical and near-infrared and assume that we know how much flux they emit at all wavelengths by applying bolometric corrections. Using the estimated total fluxes, we determine cooling ages for white dwarfs. However, these bolometric corrections depend on our understanding of cool white dwarf atmospheres unless we acquire empirical constraints at *all* wavelengths. Recent discoveries of  $\sim 10$  ultra-cool white dwarfs are puzzling. We are unable to fit *any* theoretical model to the optical and near-infrared spectral energy distributions of these stars; we do *not* know their atmospheric compositions, temperatures, or ages. This chapter will focus on our efforts to understand the cool white dwarf

atmospheres.

### 3.1 Introduction

The Sloan Digital Sky Survey (Adelman-McCarthy et al. 2006) has increased the number of known field cool white dwarfs from tens of objects to thousands (Kilic et al. 2006a; Harris et al. 2006). In addition, Hubble Space Telescope observations of the globular clusters M4 (Hansen et al. 2004) and  $\omega$  Cen (Monelli et al. 2005) resulted in the discovery of more than two thousand white dwarfs. A careful analysis of these large datasets require a complete understanding of the structure and evolution of the white dwarf stars. The main uncertainty in the white dwarf luminosity functions derived from these datasets is caused by the inadequate description of energy transport in white dwarf atmospheres, which affects both the cooling rate and observational appearance of these stars (Hansen 1998).

Cool white dwarfs have atmospheres dominated by hydrogen or helium. Both hydrogen and helium are neutral below 5000 K and the primary opacity source in H-rich cool ( $T_{\text{eff}} \leq 5500$  K) white dwarf atmospheres is believed to be collision induced absorption (CIA; Frommhold 1993) of molecular hydrogen (Bergeron et al. 1995; Hansen 1998; Saumon & Jacobson 1999). H-rich white dwarfs are predicted to become redder as they cool until the effects of CIA become significant below 5500 K. CIA opacity is strongly wavelength dependent and is expected to produce broad absorption features in the near-infrared. This flux deficiency can be seen in several stars, designated as ultracool white dwarfs (Oppenheimer et al. 2001; Harris et al. 2001; Gates et al. 2004; Farihi 2004; Farihi 2005).

There are two known opacity mechanisms in pure He white dwarf atmospheres: Rayleigh scattering and  $\text{He}^-$  free-free absorption. Rayleigh scattering is thought to be the dominant opacity source. On the other hand, Kowalski, Saumon & Mazevet (2005) argued that  $\text{He}^-$  free-free absorption may be 2-3 orders of magnitude

more significant, which would make it the dominant opacity source. In addition, Kowalski & Saumon (2004) showed that the atmosphere of He-rich white dwarfs with  $T_{\text{eff}} < 10000$  K should be treated as a dense fluid rather than an ideal gas, and that refraction effects become important. The density can be as high as  $2 \text{ g cm}^{-3}$  in these atmospheres and the index of refraction departs significantly from unity. Kowalski, Saumon, & Mazevet (2005) used their updated models to match the observed sequence of cool white dwarfs from Bergeron et al. (1997; hereafter BRL) and suggested that the coolest white dwarfs have mixed H/He atmospheres.

Bergeron & Leggett (2002) tried to fit the optical and near-infrared photometry of two ultracool white dwarfs, LHS 3250 and SDSS 1337+00, and ruled out their models for pure hydrogen atmospheric composition for these stars. They found that the overall spectral energy distributions (SEDs) of these stars can be better fitted with mixed H/He models, yet the peak of the SEDs near  $6000 \text{ \AA}$  is predicted to be too narrow. There are only three white dwarfs with significant CIA that fit the current white dwarf models in the optical and near-infrared. WD0346+246 (Oppenheimer et al. 2001) and GD392B (Farihi 2004) both require mixed H/He model atmosphere solutions. In addition, Bergeron et al. (1994) found a  $5400 \text{ K}$ ,  $\log g = 7.9$ , and  $\log N(\text{He})/N(\text{H}) = 0.8$  model atmosphere solution for LHS1126. BRL used new CIA opacity calculations and suggested that the helium abundance in this white dwarf is  $\log N(\text{He})/N(\text{H}) = 1.86$ .

The *Spitzer* Space Telescope (Werner et al. 2004) opened a new window into the Universe by enabling accurate mid-infrared photometry of faint objects (microjansky-level sensitivity). In order to understand the CIA opacity, and other unrecognized sources of opacity in cool white dwarf atmospheres, we used the *Spitzer* Space Telescope to observe nearby, relatively bright, cool white dwarfs.

### 3.2 Target Selection and Observations

We selected our targets from the spectroscopically-confirmed white dwarf catalog (McCook & Sion 2003) and required that they have  $K_S \leq 15$  mag. as measured by the Two Micron All Sky Survey (2MASS; Cutri et al. 2003). Observations reported here were obtained as part of the Spitzer Cycle 1 GO-Program 2313 (PI: Marc Kuchner). We used the Infrared Array Camera (IRAC; Fazio et al. 2004) to obtain 4.5 and 8  $\mu$ m (effective wavelengths of 4.493 and 7.782  $\mu$ m) photometry of 18 cool white dwarfs with  $5000 \text{ K} < T_{\text{eff}} < 9000 \text{ K}$ . An integration time of 30 seconds per dither, with five dithers for each target, was used (150 seconds total integration time).

We used the products of the Spitzer Science Center pipeline, the Basic Calibrated Data (BCD) Frames and the Post-BCD frames (mosaics), for our analysis. We used the IRAF PHOT routine to perform aperture photometry on individual BCD frames. Experience showed that the Point Response Function for the IRAC instrument is not well defined, and we obtained better results with aperture photometry than with PSF-fitting photometry. In order to maximize the signal-to-noise ratio, we used a 5 pixel aperture for bright, isolated objects, and 2 or 3 pixel apertures for faint objects or objects in crowded fields. We corrected the resultant fluxes by the aperture correction factors determined by the IRAC team (see the IRAC Data Handbook). We checked the results from 2, 3, and 5 pixel apertures for each object, and found them to be consistent within the errors.

Following the IRAC calibration procedure, corrections for the location of the source in the array were taken into account before averaging the fluxes of each of the five frames at each wavelength. We also performed photometry on the mosaic images and found the results to be consistent with the photometry from individual frames. We divided the estimated fluxes by the color corrections for a Rayleigh-Jeans spectrum (Reach et al. 2005a). These corrections are 1.0121 and 1.0339 for the 4.5

$\mu\text{m}$  and  $8\mu\text{m}$ -bands, respectively. Based on the work of Reach et al. (2005a), we expect that our IRAC photometry is calibrated to an accuracy of 3%. The average fluxes measured from the Spitzer images along with the 2MASS photometry, spectral types, and temperatures for our objects are given in Table 3.1. The error bars were estimated from the observed scatter in the 5 images (corresponding to 5 dither positions) plus the 3% absolute calibration error, added in quadrature.

### 3.3 Results

Figures 3.1 and 3.2 show the optical and infrared spectral energy distributions (filled triangles) of the 18 cool white dwarfs (ordered in  $T_{\text{eff}}$ ) that we observed with the IRAC instrument. Most of our objects were observed by Bergeron et al. (2001; hereafter BLR), and therefore have accurate  $BVR$  photometry, and temperature determinations. For the four DA white dwarfs not included in BLR’s analysis (WD0018-267, WD0141-675, WD0839-327, and WD1223-659), we used the  $UBV$  photometry from McCook & Sion (2003) catalog. The near-infrared photometry comes from the 2MASS All-Sky Point Source Catalog.

The expected fluxes from synthetic photometry of white dwarf model atmospheres (integrated over the filter bandpasses; kindly made available to us by D. Saumon and D. Koester) are shown as open circles in Figure 3.1. These models include CIA opacities for H-rich objects with  $T_{\text{eff}} < 7000$  K. We normalized the model atmospheres to the observed SEDs in the  $V$ -band ( $0.55 \mu\text{m}$ ), with the exception of WD1748+708 (G240-72). WD1748+708 shows a 15% deep,  $2000 \text{ \AA}$  wide absorption feature centered at  $\sim 5300 \text{ \AA}$  that affects its  $BVR$  photometry (BRL). Hence, we matched its model to the observations in the  $I$ -band. Solid lines represent the same models normalized to the observed SEDs in the  $J$ -band. Changing the normalization of the models to the  $J$ -band does not change our results significantly since the models and observations agree fairly well between the  $V$  and  $J$  bands.

Table 3.1: Infrared Photometry of Cool White Dwarfs

Object	Type	$T_{\text{eff}}(\text{K})^1$	$F_J(\text{mJy})$	$F_H(\text{mJy})$	$F_K(\text{mJy})$	$F_{4.5\mu}(\text{mJy})$	$F_{8\mu}(\text{mJy})$
WD0009+501	DAP	6540/6683	$6.40 \pm 0.12$	$5.14 \pm 0.10$	$3.53 \pm 0.07$	$0.94 \pm 0.05$	$0.32 \pm 0.02$
WD0018-267	DA	... /5498	$15.88 \pm 0.29$	$14.72 \pm 0.30$	$10.51 \pm 0.20$	$2.79 \pm 0.09$	$1.02 \pm 0.04$
WD0038-226	C <sub>2</sub> H:	5400/ ...	$7.34 \pm 0.14$	$4.14 \pm 0.09$	$2.13 \pm 0.05$	$0.48 \pm 0.02$	$0.19 \pm 0.03$
WD0101+048 <sup>2</sup>	DA	8080/8160	$6.32 \pm 0.12$	$4.49 \pm 0.09$	$2.86 \pm 0.06$	$0.75 \pm 0.03$	$0.29 \pm 0.03$
WD0126+101 <sup>2</sup>	DA	8500/8700	$3.89 \pm 0.07$	$2.69 \pm 0.06$	$1.73 \pm 0.04$	$0.45 \pm 0.02$	$0.16 \pm 0.07$
WD0141-675	DA	... /6469	$11.37 \pm 0.20$	$8.85 \pm 0.18$	$6.20 \pm 0.12$	$1.64 \pm 0.06$	$0.59 \pm 0.03$
WD0552-041	DZ	5060/5016	$9.63 \pm 0.18$	$7.35 \pm 0.15$	$5.17 \pm 0.10$	$1.80 \pm 0.06$	$0.72 \pm 0.07$
WD0553+053	DAP	5790/5853	$10.73 \pm 0.19$	$8.36 \pm 0.17$	$5.79 \pm 0.11$	$1.64 \pm 0.05$	$0.51 \pm 0.04$
WD0752-676	DA	5730/5774	$12.94 \pm 0.23$	$10.47 \pm 0.21$	$7.57 \pm 0.15$	$2.06 \pm 0.08$	$0.77 \pm 0.04$
WD0839-327 <sup>2</sup>	DA	... /8978	$37.26 \pm 0.68$	$24.81 \pm 0.51$	$16.04 \pm 0.32$	$4.01 \pm 0.14$	$1.45 \pm 0.06$
WD0912+536	DCP	7160/7273	$7.57 \pm 0.14$	$5.32 \pm 0.11$	$3.72 \pm 0.07$	$1.10 \pm 0.04$	$0.41 \pm 0.03$
WD1055-072	DC	7420/7252	$4.95 \pm 0.09$	$3.45 \pm 0.07$	$2.69 \pm 0.06$	$0.64 \pm 0.02$	$0.25 \pm 0.03$
WD1121+216 <sup>3</sup>	DA	7490/7540	$5.93 \pm 0.11$	$4.39 \pm 0.09$	$2.91 \pm 0.06$	$0.81 \pm 0.03$	$0.34 \pm ...$
WD1223-659	DA	... /7793	$7.39 \pm 0.14$	$5.10 \pm 0.12$	$3.20 \pm 0.07$	$0.90 \pm 0.04$	$0.36 \pm 0.07$
WD1748+708	DXP	5590/5964	$13.15 \pm 0.24$	$9.98 \pm 0.20$	$6.62 \pm 0.13$	$1.89 \pm 0.06$	$0.70 \pm 0.04$
WD1756+827	DA	7270/7285	$5.61 \pm 0.10$	$4.18 \pm 0.09$	$2.83 \pm 0.06$	$0.75 \pm 0.02$	$0.26 \pm 0.04$
WD1953-011	DAP	7920/7851	$9.43 \pm 0.17$	$6.29 \pm 0.13$	$4.15 \pm 0.09$	$1.13 \pm 0.04$	$0.41 \pm 0.02$
WD2140+207	DQ	8860/9407	$10.24 \pm 0.18$	$6.90 \pm 0.14$	$4.52 \pm 0.09$	$1.19 \pm 0.05$	$0.41 \pm 0.03$

(1) Estimated  $T_{\text{eff}}$  from BLR vs. this study. (2) Suspected or known double degenerate. (3) 8  $\mu\text{m}$  photometry of WD1121+216 is affected by a nearby star.

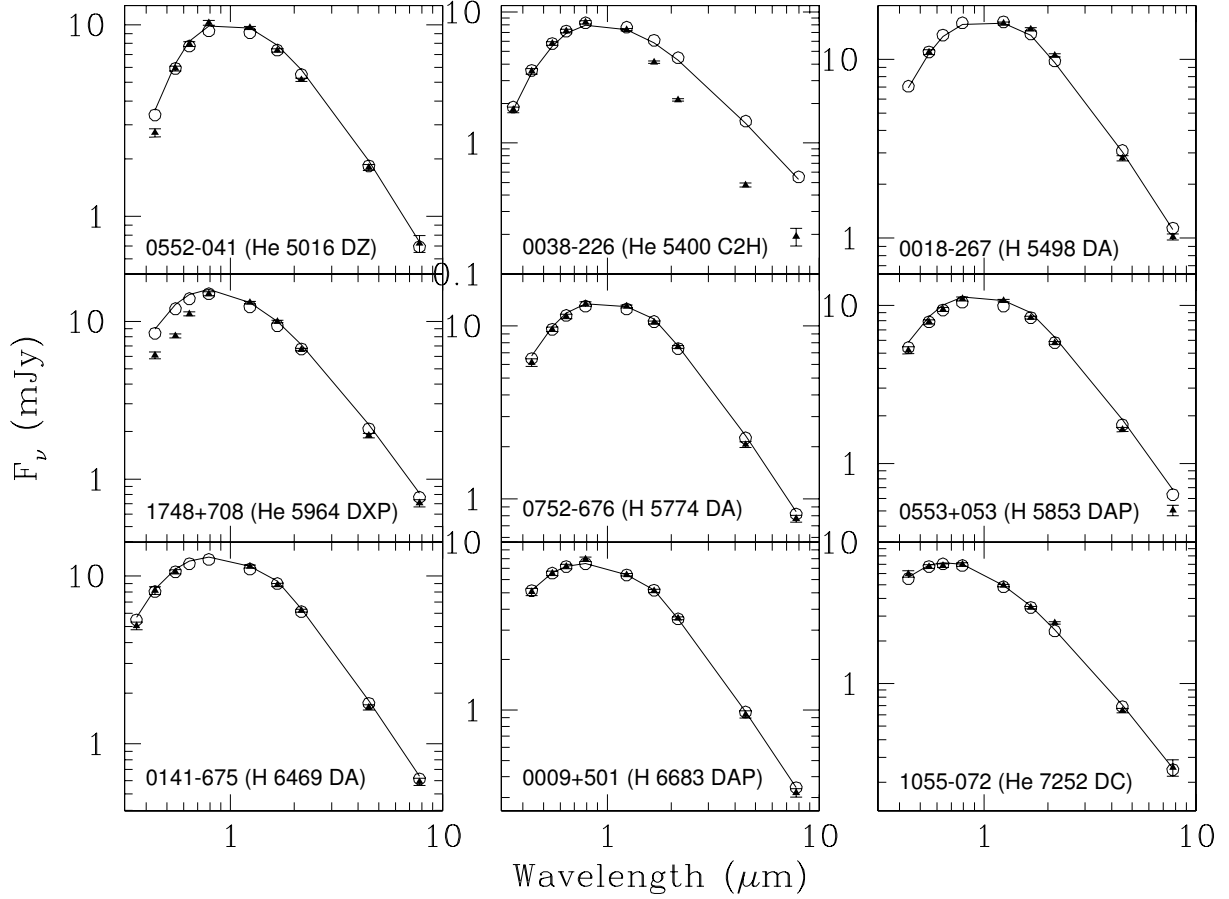


Figure 3.1: Spectral energy distributions of cool white dwarfs observed with the Spitzer Space Telescope. The observed fluxes are shown as filled triangles with error bars, whereas the expected flux distributions from synthetic photometry of white dwarf models (kindly made available to us by D. Saumon and D. Koester) are shown as open circles. Solid lines represent the same models normalized to the observed SEDs in the  $J$ -band. The object name, atmospheric composition,  $T_{\text{eff}}$ , and spectral type are given in each panel.

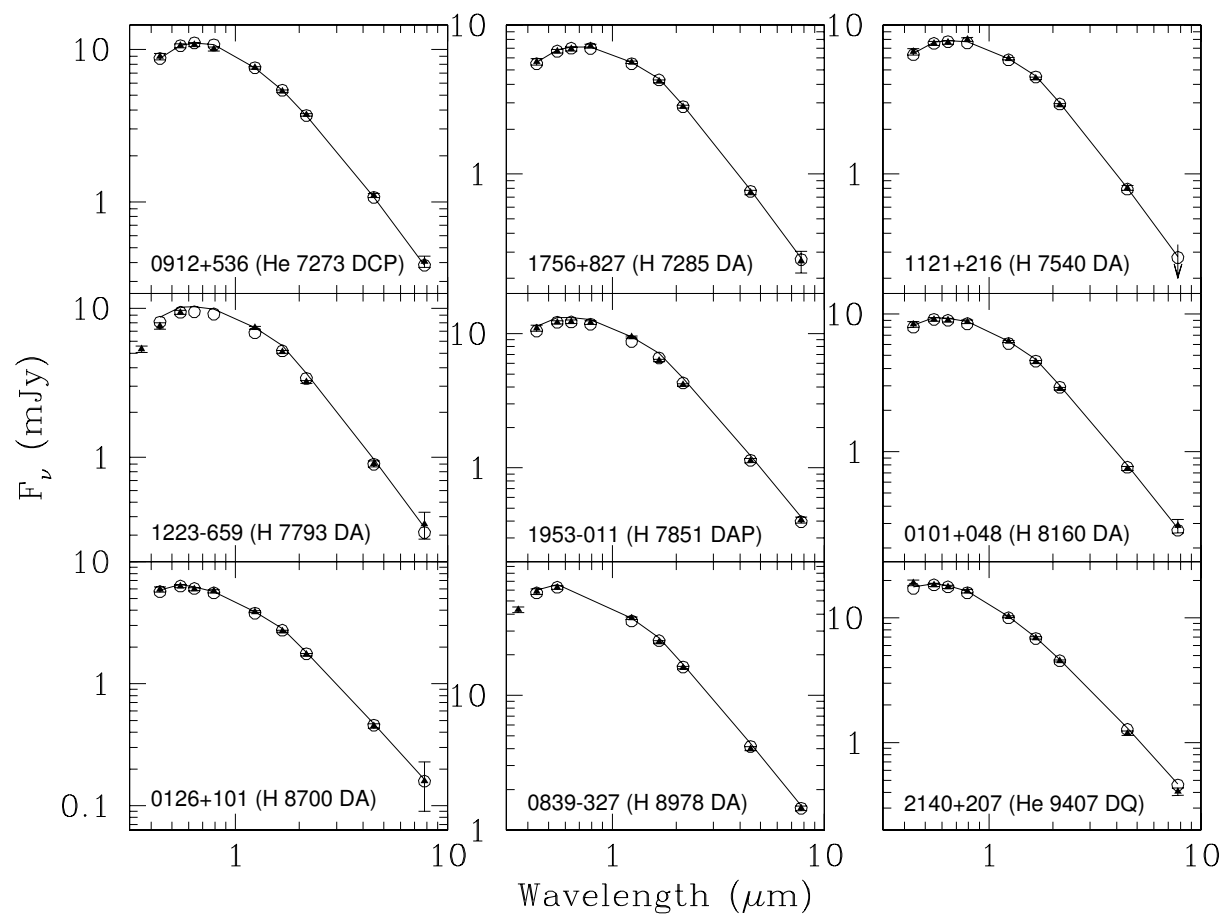


Figure 3.2: Same as Figure 3.1

In order to derive new  $T_{\text{eff}}$  values for our objects, we used pure-H and pure-He white dwarf models ( $\log g = 8$ ) and employed a  $\chi^2$  minimization technique to fit  $V$ ,  $RI$  (if available),  $JHK$ ,  $4.5\mu\text{m}$ , and  $8\mu\text{m}$  photometry.  $V$  and  $R$  photometry was omitted in our analysis of WD1748+708 because of the strong absorption feature observed in these filters. Our estimated  $T_{\text{eff}}$  values for the 8 DA white dwarfs that are in common with the BLR sample are on average slightly hotter ( $+66 \pm 81$  K) than the BLR temperatures, though they are consistent within the errors.

### 3.3.1 White Dwarfs with $T_{\text{eff}} < 7000$ K

A comparison of observed versus expected SEDs from white dwarf model atmospheres shows that all of the cool white dwarfs with  $T_{\text{eff}} < 6000$  K (except the DZ white dwarf WD0552-041) show slightly depressed mid-infrared fluxes relative to white dwarf models. In addition, WD0038-226 (LHS 1126) displays significant flux deficits (more than  $5\sigma$  in each band) in the mid-infrared. There are also two more stars with  $6000 \text{ K} < T_{\text{eff}} < 7000 \text{ K}$  (WD0009+501 and WD0141-675) that display  $\sim 1\sigma$  flux deficits. Figures 3.3 and 3.4 show the observed flux ratios in different filters for the white dwarfs in our sample. H and He rich white dwarfs are shown as filled and open circles, respectively. White dwarfs with uncertain atmospheric compositions (LHS 1126 and WD1748+708) are shown as filled triangles. Cooling tracks for H (solid line) and He rich (dashed line) white dwarfs, along with a black-body cooling track (dotted line) are also shown. Figure 3.3 shows that H-rich white dwarfs with  $T_{\text{eff}} < 7000$  K emit less flux at  $8\mu\text{m}$  than predicted from the white dwarf models. In addition, their infrared colors (Figure 3.4) require most of them to be warmer than 6500 K; they mimic warmer/bluer objects in the infrared.

LHS 1126 shows strong molecular features in the optical that are thought to be due to  $\text{C}_2\text{H}$ . These absorption features are blueshifted by about  $150 \text{ \AA}$  compared to the  $\text{C}_2$  Swan bands. Several investigators tried to explain these features in terms

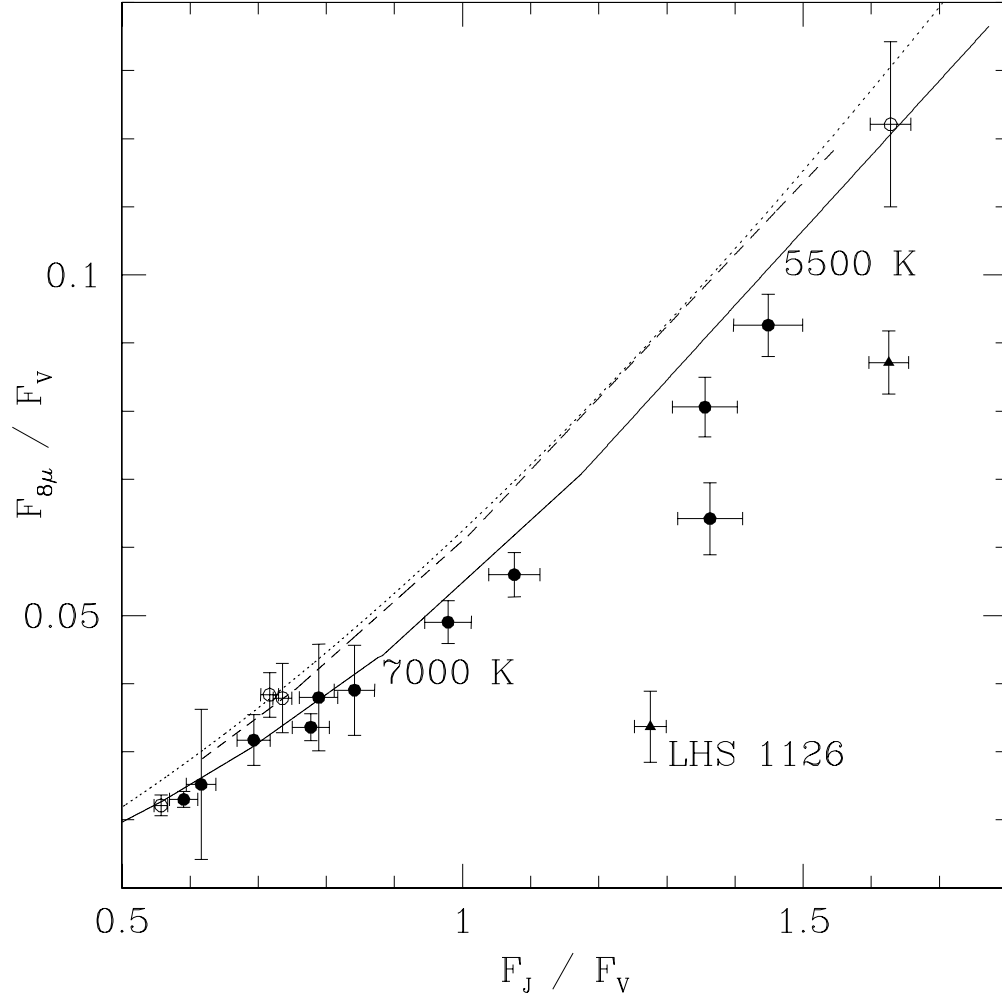


Figure 3.3: Ratio of observed fluxes in  $V$ ,  $J$ , and  $8\mu\text{m}$  bands for pure H (filled circles) and He (open circles) white dwarfs. White dwarfs with uncertain atmospheric compositions are shown as filled triangles. Model cooling tracks for pure H (5000 – 60000 K, solid line) and pure He white dwarfs (5000 – 8000 K, dashed line) are also shown. A dotted line shows the expected sequence for a blackbody (5000 – 10000 K).

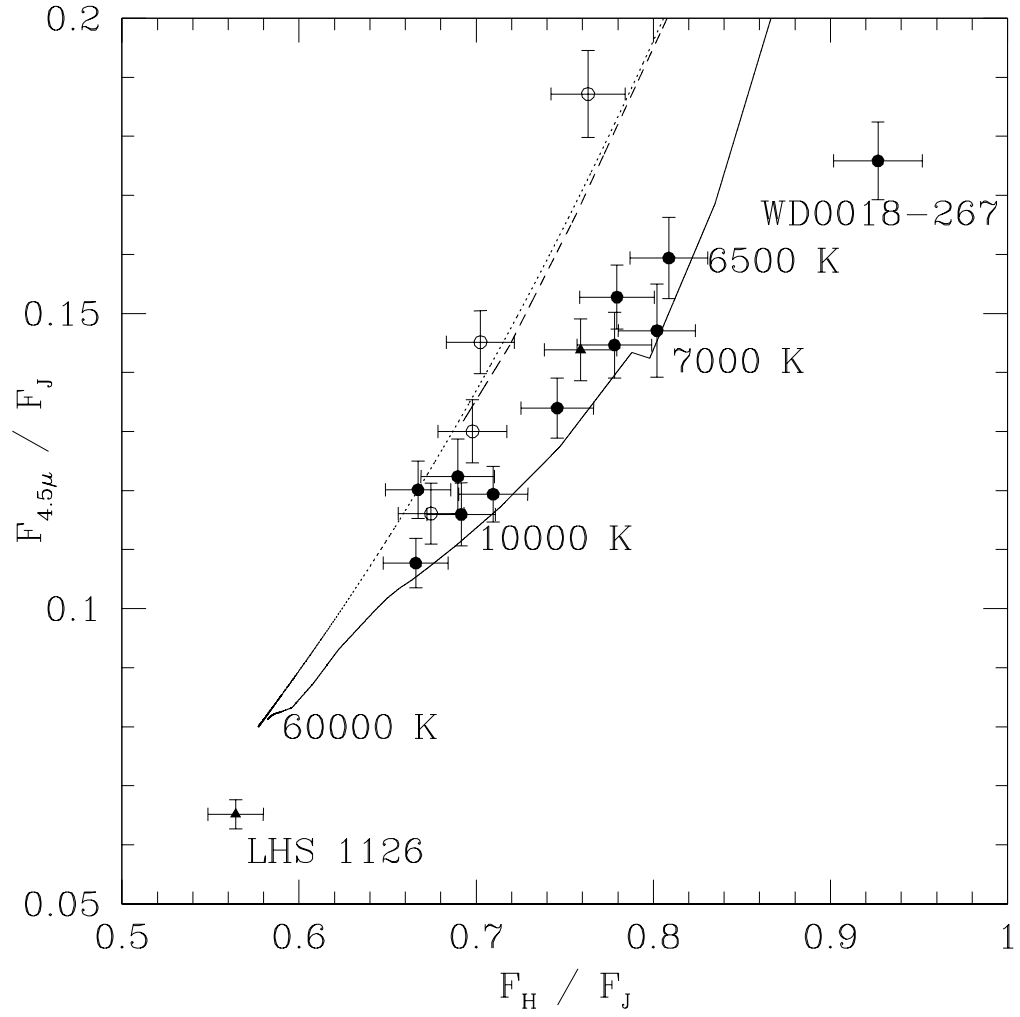


Figure 3.4: Ratio of observed fluxes in  $J$ ,  $H$ , and  $4.5\mu\text{m}$  bands. The symbols are the same as in Figure 3.3. Note that the discontinuity at 7000 K is due to the transition from Koester models to Saumon models.

of either pressure shifts in a He-dominated atmosphere or magnetic displacements of the Swan bands (see Schmidt et al. 1995). However, Bergeron et al. (1994) and Schmidt et al. (1995) showed that both scenarios fail for this star. In addition, Schmidt et al. (1995) suggested that  $\text{C}_2\text{H}$  is the most probable molecule to form under the conditions in LHS 1126. The mid-IR flux deficit of LHS 1126 is discussed below. WD1748+708 shows a very broad feature in the optical (see the discussion above) and has a  $\sim 200$  MG magnetic field (Angel 1977). BLR suggested that this broad feature may be explained as the  $\text{C}_2\text{H}$  molecular feature broadened by the strong magnetic field. Hence, all of the stars with mid-infrared flux deficits have either H-rich atmospheres or show trace amounts of hydrogen.

The coolest white dwarf in our sample is a DZ white dwarf, WD0552-041, with an estimated  $T_{\text{eff}} = 5016$  K. The observed SED fits the model predictions fairly well for this star with the exception of  $B$  photometry which is probably affected by the metals in the photosphere (Wolff et al. 2002). The origin of metals in white dwarf atmospheres has been a mystery for a long time (Zuckerman et al. 2003). The discovery of debris disks around the white dwarfs G29-38 (Zuckerman & Becklin 1987; Reach et al. 2005b) and GD362 (Becklin et al. 2005; Kilic et al. 2005a) suggest that accretion from a debris disk may explain the observed metal abundances in at least some DAZ white dwarfs. Nevertheless, we do not see any mid-infrared excess around the cool DZ white dwarf WD0552-041.

### 3.3.2 White Dwarfs with $T_{\text{eff}} > 7000$ K

The remaining ten objects with  $T_{\text{eff}} > 7000$  K do not show any excess or deficit in their flux distributions. There are three known or suspected double degenerate stars in our sample (WD0101+048, WD0126+101, and WD0839-327; Maxted et al. 2000). We do not see any evidence of a composite SED for these objects; if they are equal mass binaries, the primary and secondary stars must have similar temperatures.

Limits on possible substellar companions or debris disks around these stars as well as  $\sim 100$  other white dwarfs will be discussed in a future publication (Mullally et al., in preparation). One caveat seen in Figure 3.2 is that WD1121+216 is near a brighter source, and even a 2 pixel aperture on the white dwarf is contaminated by the light from the nearby star. Hence, we provide only an upper limit for  $8\mu\text{m}$  photometry of this object.

WD2140+207 is a DQ star showing molecular  $\text{C}_2$  swan bands in the optical. The presence of carbon in cool He white dwarf atmospheres is thought to be the result of convective dredge up of carbon that diffused upward into the He envelope (Pelletier et al. 1986). Figure 3.2 shows that the spectral energy distribution of WD2140+207 fits a blackbody distribution reasonably well. The absence of metal lines in the optical spectrum of this star, plus the absence of excess infrared radiation provide further evidence that the carbon was not accreted from the interstellar medium or a circumstellar debris disk. One caveat between our analysis and BLR’s analysis is that using pure-He model atmospheres, BLR estimated  $T_{\text{eff}} = 8860 \pm 300$  K for this star. Fitting  $VRIJHK$ ,  $4.5\mu\text{m}$  and  $8\mu\text{m}$  photometry of this star with a blackbody, we estimate the temperature of this star to be 9407 K. None of the other stars in our sample that are in common with the BLR sample show this discrepancy. Dufour et al. (2005) reanalyzed the DQ stars in the BLR sample and demonstrated that the inclusion of carbon in model atmosphere calculations reduces the estimated effective temperatures and surface gravities for DQ white dwarfs. They obtained even a lower  $T_{\text{eff}}$  measurement ( $8200 \pm 250$  K) for WD2140+207.

### 3.4 Discussion

Our Spitzer observations showed that all H-rich white dwarfs with  $T_{\text{eff}} < 7000$  K show slight mid-infrared flux deficits. Having several stars with small deficits makes these deficits significant. Moreover, LHS 1126 shows significantly depressed

mid-infrared fluxes relative to white dwarf models. Debes et al. (2005, private communication) have also found 10-20% flux deficits ( $\geq 3\sigma$  significance) at 4.5, 5.6, and  $8\mu\text{m}$  in two DAZ white dwarfs with  $T_{\text{eff}} = 6820$  K and 7310 K. Combining the facts that WD0552-041 (with a pure-He atmosphere) does not show a clear flux deficit, and all H-rich white dwarfs cooler than 7000 K do exhibit mid-infrared flux deficits, LHS1126 and WD1748+708 are likely to have mixed H/He atmospheres. This is also consistent with Bergeron et al.'s (1994) and Wolff et al.'s (2002) analysis. However, one question remains to be answered: can these flux deficits be explained by CIA?

The atmospheres of M, L, and T dwarfs are known to exhibit CIA (Borysow et al. 1997). Roellig et al. (2004) obtained mid-infrared spectroscopy of M, L, and T dwarfs in the  $5 - 15 \mu\text{m}$  range. Their Figure 2 shows that the observed spectra are in good agreement with the model atmosphere calculations, with only a few minor deviations. Hence, CIA calculations for low density atmospheres seem to be accurate.

The near-infrared ( $1-2 \mu\text{m}$ ) flux deficit in LHS 1126 was discovered by Wickramasinghe et al. (1982). Bergeron et al. (1994) and BRL explained this deficit as CIA by molecular hydrogen due to collisions with helium and found the H/He ratio to be  $\sim 0.01$ . Wolff et al. (2002) used Faint Object Spectrograph data plus optical and infrared photometry of LHS1126 to model this star's SED in the  $0.2 - 2.2 \mu\text{m}$  range. They found that the hydrogen abundance reported by Bergeron et al. (1994) would result in extremely strong Lyman  $\alpha$  absorption, and the SED is best fitted with an abundance ratio of  $\text{H/He} = 3 \times 10^{-6}$ . Wolff et al. (2002) and Bergeron et al. (1994) models do not give a consistent picture for the H/He ratio and neither model is adequate. We revisit this problem by extending the observations to  $8\mu\text{m}$ . Figure 3.5 shows the ultraviolet spectrum (kindly made available to us by D. Koester) and optical and infrared photometry of LHS 1126 along with a 5400 K blackbody (dot-

ted line). Mixed atmosphere white dwarf models (kindly made available to us by D. Saumon) with  $T_{\text{eff}} = 5400$  K,  $\log g = 7.9$ , and  $\log N(\text{He})/N(\text{H}) = 1.5$  (lower solid line) and  $\log N(\text{He})/N(\text{H}) = 1$  (upper solid line) are also shown. These white dwarf models include CIA opacities but not Lyman  $\alpha$  absorption, therefore they cannot be used to match the ultraviolet data. If we just use the optical and near-infrared photometry (as in Bergeron et al. 1994), we could fit the observations with a  $\log N(\text{He})/N(\text{H}) = 1 - 1.5$  model. However, these models cannot explain the observed flux deficits in the Spitzer observations. Bergeron et al. (1995) and Hansen (1998) models cannot explain these flux deficits either (B.M.S. Hansen and P. Bergeron 2005, private communication). CIA is expected to create features in the spectrum up to  $3\mu\text{m}$ , and the SEDs of cool white dwarfs are expected to return to normal in the mid-infrared (Figure 3.5; see also Figure 6 of Jorgensen et al. 2000).

Figure 3.5 also shows a power law distribution with  $\alpha = 2$ , i.e. a Rayleigh-Jeans spectrum (dashed line). The infrared spectral energy distribution of LHS 1126 follows a Rayleigh-Jeans spectrum fairly well. It is striking to note that we can fit the ultraviolet and optical part of the SED with a 5400 K blackbody, and the infrared part of the SED with  $T_{\text{eff}} > 10^5$  K. The power law is a reasonable but not a perfect fit to the infrared spectral energy distribution of this object, and spectroscopy with the Spitzer Telescope may reveal more structure in the mid-infrared, but the current data suggest the following:

1 – The CIA opacity calculations are incomplete, and there is an unexplained flux deficit in the mid-infrared. As the densities in white dwarf atmospheres approach liquid state densities, molecular absorption ( $\text{H}_2\text{-H}_2$ ,  $\text{H}_2\text{-He}$ ) and light scattering are expected to become increasingly important. Current CIA opacity calculations in dense media may be incomplete in certain wavelength regimes, for example the roto-vibrational band of  $\text{H}_2$  CIA may be enhanced compared to predictions (L. Frommhold and D. Saumon 2005, private communication). On the other hand,

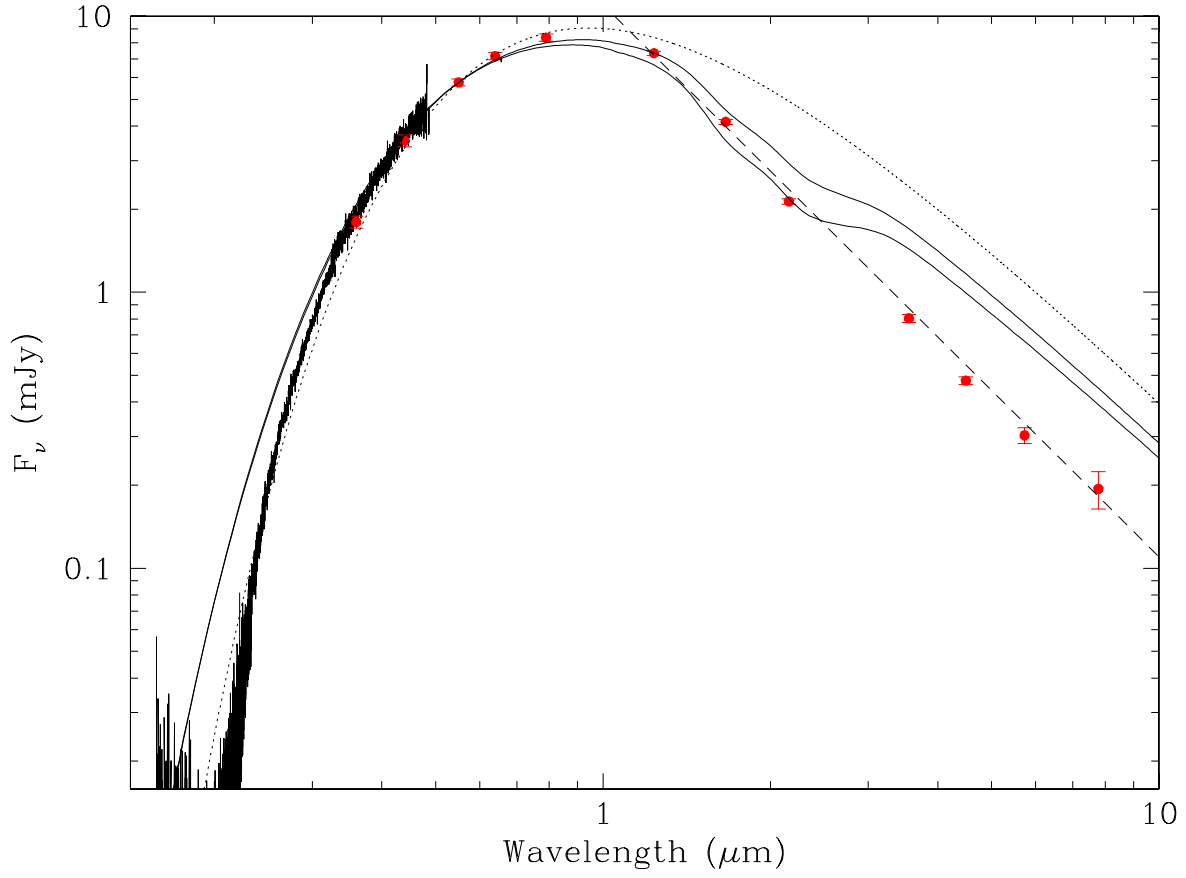


Figure 3.5: Spectral energy distribution of LHS 1126, along with a 5400 K blackbody (dotted line). IRAC1 ( $3.6\mu\text{m}$ ) and IRAC3 ( $5.8\mu\text{m}$ ) photometry of this star from Cycle2 Spitzer observations is also shown. White dwarf models with  $T_{\text{eff}} = 5400$  K,  $\log g = 7.9$ , and  $\log N(\text{He})/N(\text{H}) = 1.5$  (lower solid line) and  $\log N(\text{He})/N(\text{H}) = 1$  (upper solid line) are also shown. The dashed line shows a power law with  $\alpha = 2$ .

the featureless spectra of the ultracool white dwarfs (Gates et al. 2004), and the reasonably good fit of a Rayleigh-Jeans distribution to the LHS 1126 SED in the infrared suggest that another mechanism is required to explain the mid infrared flux deficits observed in white dwarfs. CIA is expected to disappear with the dissociation of molecules when  $T_{\text{eff}}$  increases past 5500 K. Therefore, white dwarfs with  $T_{\text{eff}} > 6000$  K that show infrared flux deficits could not be explained by changing the CIA opacities.

2 – The mid-infrared flux deficits are caused by some as-yet unrecognized physical process(es). The problem may be caused by an unknown or poorly understood absorption process, or it may be the result of a different source function operating in these dense atmospheres.  $\text{H}^-$  bound-free absorption is thought to be the most important source of opacity in warmer DA white dwarfs. More work is required to test if possible changes in this absorption could help explain the mid-infrared flux deficits. The input physics used in white dwarf model atmospheres is mostly based on the ideal gas approximation. The extreme conditions in white dwarf atmospheres require a new look at dense medium effects on the equation of state, chemistry, opacities, and radiative transfer. Refractive opacities, the presence of heavy elements, formation of trace species, and many other factors can change the opacity sources in white dwarf atmospheres (see Kowalski 2006 for a detailed discussion).

Near/mid-infrared photometry and spectroscopy of ultracool white dwarfs and the so-called  $\text{C}_2\text{H}$  stars will be useful to test these ideas.

### 3.5 Conclusion

At this time, we only report and do not understand the observed mid-infrared flux deficits. The most extreme white dwarf in our sample, LHS 1126, is missing 13% of the flux between  $0.3 - 10 \mu\text{m}$  compared to a 5400 K blackbody. For a 5400 K pure He

atmosphere white dwarf, 13% difference in luminosity corresponds to a difference of  $\sim 16\%$  in age. However, the flux deficits are not as severe for the other white dwarfs in our sample. Observations of cooler white dwarfs with  $T_{\text{eff}} \leq 5000$  K are required to check if the observed mid-infrared flux deficit in LHS 1126 is the rule or the exception. These observations may force us to revise the bolometric corrections for cool white dwarfs, and are crucial for white dwarf cosmochronology.

Our current/future efforts to resolve the mysteries of cool white dwarf atmospheres are discussed in Chapter 6.

## Chapter 4

# White Dwarfs and Dark Matter

*“Duct tape is like the force. It has a light side, a dark side, and it holds the universe together.”*

*– Oprah Winfrey*

Our current understanding of the matter and energy in the Universe is as follows: 4% of the matter in the Universe is visible,  $\sim 70\%$  is in the form of dark energy and  $\sim 26\%$  is in the form of dark matter. We have no idea of what the dark energy or dark matter is. We can see their effects in large scale structure of the Universe, yet we cannot directly see them. One of the recent ideas for the nature of dark matter is to explain it by faint halo white dwarfs that have not been discovered in previous surveys. These white dwarfs would be unaccounted for in the total mass budget of the Galaxy and therefore could explain part of the dark matter. In order to test this claim, we looked at the deepest images of the Universe taken with the Hubble Space Telescope. If there were a large number of faint halo white dwarfs in the Galaxy, we would find them in the Hubble Deep Field and Ultra Deep Field.

## 4.1 Introduction

Major observational campaigns have searched for dark matter in the form of massive compact halo objects (MACHOs) using microlensing events (e.g. Alcock et al 1997; Afonso et al. 2003; Udalski et al. 1992). The detection of 13–17 microlensing events toward the Large Magellanic Cloud during 6 years by the MACHO collaboration implies that a significant fraction (20%) of the halo of the Galaxy may be in the form of compact halo objects (Alcock et al. 2000). The time scale of these lensing events eliminates the possibility of MACHOs having substellar masses. The MACHO collaboration finds a most probable mass of  $0.5 M_{\odot}$ , which supports the idea of a massive halo comprised of baryonic matter in the form of low luminosity white dwarfs (Kawaler 1996). Recent observations by the EROS group provide further evidence that less than 25% of a standard dark matter halo can be composed of objects with a mass between  $2 \times 10^{-7} M_{\odot}$  and  $1 M_{\odot}$  (Afonso et al. 2003).

Halo white dwarf stars are expected to have large proper motions as a result of their high velocities relative to the Sun. HST proper motion studies of the Globular Cluster NGC 6397 showed that most of the required dark matter in the solar vicinity can be accounted for by a population of old white dwarfs representing the thick disk and halo of the Galaxy (Mendez 2002). Claims by Oppenheimer et al. (2001) and Ibata et al. (2000) that they had found a significant population of halo white dwarfs from kinematic surveys were tantalizing. Their discoveries seemed to be consistent with earlier findings of an old population of white dwarfs in the Hubble Deep Field (Mendez & Minniti 2000). However, further analysis by several groups showed that the sample of Oppenheimer et al. (2001) could also be interpreted as the tail of a kinematically warmer white dwarf component, better explained by the thick disk population of the Galaxy (Reid et al. 2001; Reyle et al. 2001; Mendez 2002; Bergeron 2003).

The Hubble Deep-Field (HDF) provides a unique window on the Universe

(Williams et al. 1996; Flynn et al. 1996). The extreme depth of the HDF provides an unprecedented advantage to find faint stellar objects as well as to study very distant galaxies. The advantage of going deep is that it allows us to search for faint stellar components of the Galaxy in the regions of the color–magnitude diagram that are devoid of any contamination by standard Galactic stars. The lack of ordinary disk stars is due to the finiteness of the Galaxy (Flynn et al. 1996). Mendez & Minniti (2000) claimed that the faint blue objects found in the HDF–North and HDF–South are Galactic stars based on the observed number of blue sources and extragalactic sources in the two fields. Independent proper motion measurements for five of these faint blue sources by Ibata et al. (1999) suggested that they are cool halo white dwarfs which could account for the entire missing mass in the solar neighborhood. Third epoch data on these five objects, however, did not show any significant proper motion (R. Ibata, private communication; Richer 2001).

We used the original HDF North data and images of the same field taken 7 years later for the Great Observatories Origin Deep Survey (GOODS) to measure proper motions of the point sources analyzed by Ibata et al. (1999) and Mendez & Minniti (2000). We also extended this work to the HDF South by using the original HDF South data and images of the same field taken 3 years later for the GO-9267 proposal (WFPC2 Supernova Search, PI: S. Beckwith).

## 4.2 Hubble Deep Field North

### 4.2.1 Proper Motion Measurements

GOODS is a multi-wavelength, multi-facility deep survey designed to study galaxy formation and evolution over a large redshift range. It includes deep imaging with the Advanced Camera for Surveys (ACS) in the B, V, i, and z bands, and reaches down to  $AB = 28.1, 28.4, 27.7,$  and  $27.6$  in the four bands, respectively (10 sigma,

point source; Giavalisco et al 2003). The second epoch data, acquired with the HST and the ACS as part of the GOODS ACS Treasury program, provide a baseline of 7 years. The GOODS team released version 1.0 of the reduced, calibrated, stacked, and mosaiced images of the HDF – North in 17 sections. Section 32 (total integrations of 34.9 ks in V and 36.9 ks in I) and section 33 (48.9 ks in V and 51.9 ks in I) overlap with the original HDF–North images.

The source catalogs for the first epoch were produced by the Space Telescope Science Institute (STScI) from the combined and drizzled images. We note that the first epoch HDF–North catalogue is based on rereduced HDF–North images by Casertano et al. (2000), providing a 10% increase in depth. We used the SExtractor package (Bertin & Arnouts 1996), version 2.3, to build source catalogues from the second epoch data. The major motivation for using SExtractor was its incorporation of weight maps in modulating the source detection thresholds. Source detection was carried out on the inverse-variance-weighted sum of the V and I band drizzled images. The combined V + I image is deeper than any of the individual images (Casertano et al. 2000). Only those objects matching the positions of the objects in the first epoch data with differences less than  $0.2''$  are included in our final catalogue. Furthermore, we visually inspected all of the sources used for our proper motion study to avoid any mismatches. Although the GOODS Team released version r1.0 of the ACS multi-band source catalogs, their catalogs are based on z–band detection only (Giavalisco et al. 2004). Hence the released catalogs are not appropriate for the study of faint blue objects. The GOODS data are 0.5 – 0.8 mag shallower than the original HDF images, therefore we use the first epoch images for photometry. Astrometric and photometric data for the point sources in the HDF–North are given in Table 1. We adopted the calibrated V and I photometry of Mendez & Minniti (2000).

Although the effective point spread function (ePSF) fitting procedure (An-

Table 4.1: Point Sources in the Hubble Deep Field North

Object	X(HDF)	Y(HDF)	X(GOODS)	Y(GOODS)	$V$	$V - I$
HDF2272	869.387	989.094	3952.627	838.889	19.78	1.04
HDF2234	2903.711	1129.655	6500.462	8114.658	20.78	0.20
HDF101	315.227	3788.366	4778.925	4538.35	21.45	1.12
HDF1583	1026.935	1803.079	4580.210	1742.69	22.19	1.47
HDF1828	2448.822	1573.769	6184.354	704.792	24.30	2.38
HDF3072	1877.251	349.952	4837.550	7714.658	24.27	1.29
HDF2134	1194.967	1255.044	4489.335	987.877	24.74	2.52
HDF2258	247.806	1117.993	3264.773	1328.88	24.95	2.91
HDF1470	2440.850	1935.845	6368.745	1148.24	25.33	1.50
HDF1481	3424.519	1920.592	7554.512	601.04	25.87	2.22
HDF161	1388.682	3818.963	6098.469	4001.02	25.74	0.77
HDF684	956.369	2845.424	5052.038	3049.25	26.70	1.82
HDF3031	3380.128	403.175	6688.739	6975.563	26.50	0.44
HDF759	534.482	2774.917	4501.172	3190.23	26.66	0.46
HDF3000	1306.869	420.559	4178.915	8105.979	27.36	3.19
HDF995	642.304	2475.111	4471.563	2767.75	27.08	0.52
HDF1022	401.701	2504.499	4195.475	2932.52	27.87	0.29
HDF861	537.648	2643.861	4434.536	3028.95	27.87	0.06
HDF1705	2113.471	1690.358	5839.241	1025.76	28.11	0.46
HDF2729	1746.126	710.752	4866.870	31.945	28.30	0.70
HDF2217	2766.571	1181.931	6359.981	59.073	28.26	0.34
HDF806	1171.947	2699.015	5235.329	2756.72	28.57	0.61
HDF1135	1064.710	2306.869	4895.408	2337.47	28.78	1.16
HDF2991	291.521	436.858	2951.714	479.141	28.58	0.24
HDF1288	926.550	2096.186	4613.698	2154.15	28.53	-0.07
HDF946	351.213	2538.371	4151.918	2999.19	28.49	-0.37
HDF1196	1030.595	2279.031	4839.458	2321.74	28.79	0.74
HDF723	938.652	2806.484	5008.853	3012.2	28.92	0.94
HDF1816	3006.002	1601.085	6874.624	438.659	29.02	0.45
HDF1039	593.115	2432.467	4388.899	2741.84	28.43	-1.35
HDF774	445.116	2747.477	4378.614	3204.48	28.82	0.03

derson & King 2000) is the most precise astrometric technique for HST images, well-exposed star images are required to accurately sample the PSF. There are not many stars in the Hubble Deep Field, and the main source of error in our proper motion measurements is the positions of the reference compact objects (galaxies). Therefore the ePSF method is not necessary and was not used for our analysis.

The original HDF images were rereduced and corrected for distortion by Casertano et al. (2000). The second epoch data were corrected for distortion by the GOODS team using the latest (July 2003) coefficients released by the ACS group at STScI. Even with these distortion corrections, however, some distortion remains (Bedin et al. 2003). The effect of the remaining distortion is larger if a global coordinate transformation is used. Instead of performing a global transformation, we have used the IRAF routine GEOMAP to derive a quadratic local transformation for each star, using a surrounding net of several dozen compact objects (isolated, low residuals, and not fuzzy). After mapping the distortions with the GEOMAP package, object coordinates were transformed to the second epoch positions with the GEOXYTRAN routine.

Figure 4.1 shows the contour maps for the two bright stars HDF2272 and HDF3072. The immediate field around each object is shown with dashed lines crossing at the first epoch position. The second epoch position is marked with an asterisk. This figure shows that SExtractor works very well for bright compact objects and these two objects are apparently moving.

#### 4.2.2 Results

Proper motion measurements are mainly affected by distortion mapping and selection of reference objects. The RMS error of the transformations are larger than the positional errors of the objects. In order to check our distortion solution we have used the GEOMAP package with different polynomial terms. We started with

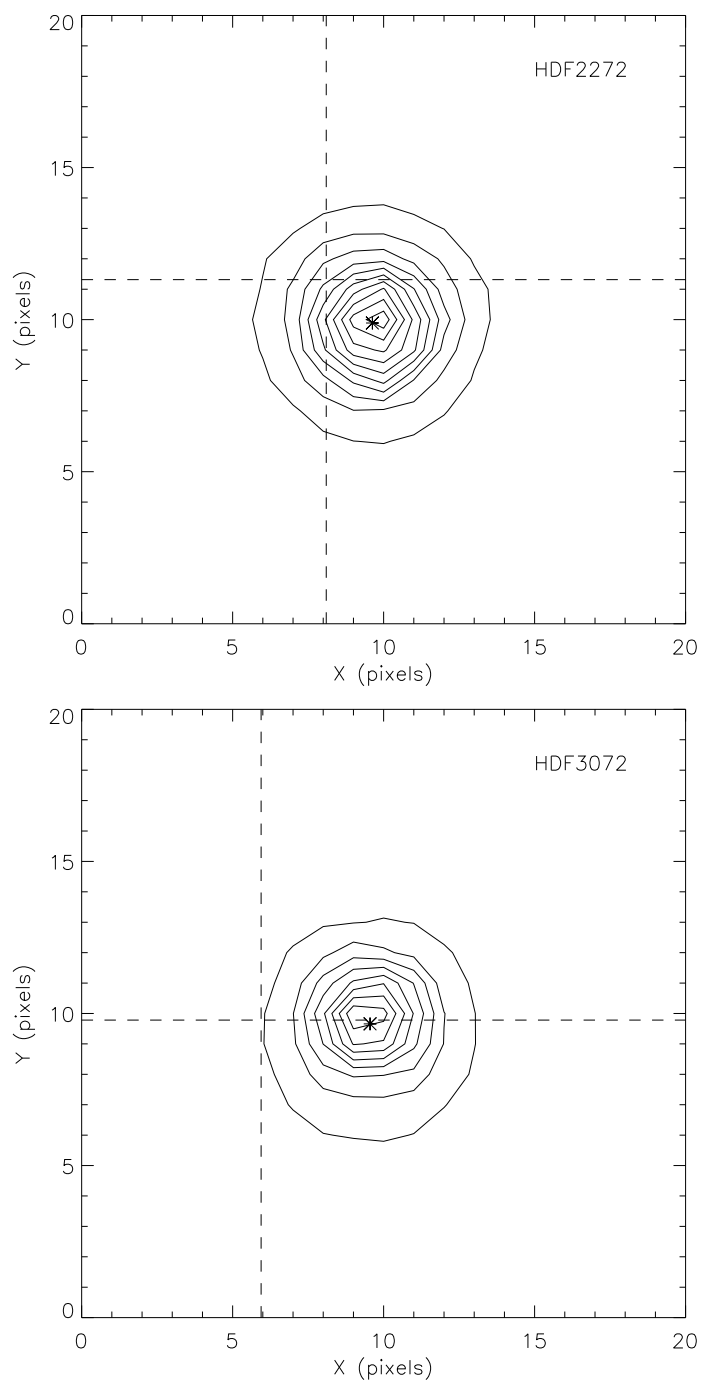


Figure 4.1: Two bright, apparently moving objects. The panels show contour maps and first and second epoch positions of the stars HDF2272 and HDF3072. The contour maps show the flux distribution around each object (20 x 20 pixels,  $0.6'' \times 0.6''$ ). Dashed lines cross at the first epoch position. An asterisk marks the second epoch position.

no distortion correction and deleted deviant points using a  $3\sigma$  rejection algorithm. Rejection of very deviant points is required due to the fact that our reference objects are compact galaxies and centroiding errors are larger for galaxies. We used quadratic, quadratic with one cross-term, and quadratic with 4 cross-terms local transformations. For most of the objects, the results from higher-order transformations were very similar to the results from the quadratic (with no cross-term) local transformation. This gave us confidence in the stability of our procedure. For two objects, the use of the higher-order terms made the distortion solution unstable because of the relative positioning of the reference objects. To be conservative, we adopted the quadratic with no cross-term local transformation for distortion mapping for all of our objects.

Figure 4.2 shows the differences between second epoch coordinates and transformed first epoch coordinates for one of our stars, HDF1583, and the surrounding 40 reference objects. A  $3\sigma$  rejection algorithm is later used to eliminate outliers from the sample. Error bars include positional errors from the SExtractor first and second epoch coordinates and the RMS error of the transformation. It is clear from this figure that HDF1583 is statistically well separated from the reference objects, most or all of which are galaxies: it is moving with respect to this external reference frame.

In order to further test our transformations, we have also used all compact objects with positional differences between the two epochs of less than 0.4 pixels to perform a global transformation. We found 377 compact galaxies matching our criteria, and fit a quadratic polynomial to map the distortions. As described above, we have measured proper motions in four to six different ways. Our conservative estimate of the proper motions, their significance ( $\mu/\sigma$ ), and position angle are given in Table 4.2, along with the observed range of proper motions from different transformation versions. A comparison of the observed ranges and errors for the

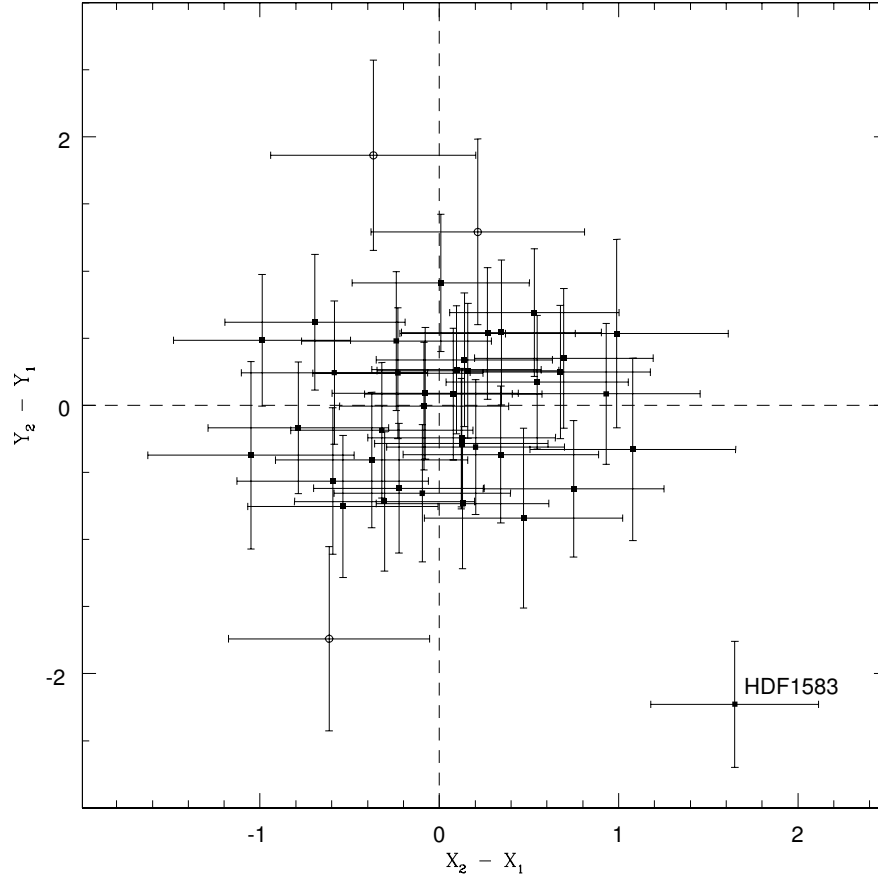


Figure 4.2: Difference between second epoch coordinates  $(X_2, Y_2)$  and transformed first epoch coordinates  $(X_1, Y_1; \Delta X = 1$  corresponds to 30 mas) for HDF1583 and the surrounding reference compact objects. Reference objects that are not included in our transformations are shown as open circles. Error bars include centroiding errors from the first and second epochs, and the RMS error of the GEOMAP transformation. HDF1583 is an example of an object that is clearly exhibiting proper motion.

Table 4.2: Proper Motions

Object	$\mu$ (mas/yr)	$\sigma$	$\mu/\sigma$	$\mu$ (range)	Pos. Angle
HDF2272	8.95	2.48	3.61	8.30–10.09	227.0
HDF2234	10.05	2.46	4.09	8.67–11.08	298.3
HDF101	6.03	2.50	2.41	5.00–6.34	238.0
HDF1583	11.60	2.25	5.17	11.48–11.97	215.3
HDF1828	2.47	2.06	1.20	1.21–3.08	281.7
HDF3072	15.47	3.83	4.04	15.40–17.51	268.0
HDF2134	3.28	2.65	1.24	2.84–4.44	184.4
HDF2258	8.34	2.92	2.86	8.02–8.86	204.2
HDF1470	4.06	3.06	1.33	3.40–4.06	230.6
HDF1481	10.53	2.51	4.19	10.32–11.38	156.1
HDF161	1.72	1.53	1.12	1.27–2.42	96.5
HDF684	3.71	2.19	1.69	3.33–4.42	191.0
HDF3031	1.53	2.68	0.57	1.53–3.76	211.3
HDF759	1.37	2.56	0.53	0.29–1.73	206.6
HDF3000	3.66	2.35	1.56	3.43–5.24	230.7
HDF995	1.24	1.64	0.76	1.21–1.44	190.5
HDF1022	3.27	3.06	1.07	2.19–4.14	251.7
HDF861	2.22	2.93	0.76	1.56–2.22	160.8
HDF1705	3.64	3.00	1.21	1.83–5.53	235.1
HDF2729	3.45	1.99	1.73	2.88–3.78	106.6
HDF2217	2.01	2.79	0.72	1.78–2.86	358.0
HDF806	1.15	2.91	0.40	0.88–2.36	90.4
HDF1135	3.45	2.00	1.73	3.45–4.11	297.6
HDF2991	3.77	3.28	1.15	2.84–3.86	36.6
HDF1288	3.55	2.89	1.23	2.17–4.25	206.1
HDF723	2.76	2.42	1.14	2.32–3.69	98.4
HDF1816	5.49	1.89	2.91	4.77–6.30	129.2
HDF1039	3.13	2.50	1.25	2.28–4.44	200.8
HDF774	4.80	2.38	2.02	3.56–5.22	251.3

proper motion measurements show that the errors are consistent with the variations between fitting techniques. Typical errors in our measurements are  $\sim 2.5$  mas  $\text{yr}^{-1}$ . Hence, only those objects having proper motions larger than 5 mas  $\text{yr}^{-1}$  have significance greater than two. The bright objects HDF2272, HDF2234, HDF101, HDF1583, HDF3072, HDF2258, and HDF1481 are definitely moving, and the faint objects HDF1816 and HDF774 might be moving.

Star–galaxy confusion becomes worse at faint magnitudes. Only objects  $15\sigma$  above the sky level were analyzed by Mendez & Minniti (2000). Proper motions pro-

vide further star-galaxy separation since anything with a significant proper motion cannot be very distant (e.g. Ibata et al. 1999).

We calculated photometric distances for all objects in our sample assuming that they are either main sequence stars, white dwarfs, or white dwarfs on the blue hook of the cooling sequence. For a given  $V - I$  color, we estimate three absolute magnitudes for each object by linearly interpolating the  $V - I$  and  $M_V$  relation for main sequence stars (Table 15.7 of Allen’s *Astrophysical Quantities*, 2000), white dwarfs, and cool white dwarfs (Hansen et al. 1999).

Cool white dwarf colors can be quite different in Johnson/Kron-Cousins and the HST filters since  $H_2$  opacity produces sharp flux peaks in the white dwarf spectra. The observed colors of the white dwarfs depend on the transmission peaks of the filters. Richer et al. (2000) calculated the HST colors for white dwarfs using the Holtzmann et al. (1995) bandpasses and the transformations they use to express fluxes in V, R and I. Hubble Deep Field photometry is calibrated using the Holtzmann et al. (1995) transformations (Mendez & Minniti 2000). Therefore we used Richer et al. (2000) white dwarf cooling tracks instead of Chabrier et al. (2000b) models. We use the apparent magnitudes of the objects and the adopted absolute magnitudes to estimate photometric distances.

Proper motion measurements and derived distances can be used to calculate tangential velocities using the equation

$$\mu = \frac{V_{tan}}{4.74d} \quad (4.1)$$

where  $\mu$  is the proper motion in arcsec yr<sup>−1</sup>,  $d$  is the distance in parsecs, and  $V_{tan}$  is the tangential velocity in km s<sup>−1</sup>. With the assumption that the objects are either main sequence stars, DA white dwarfs, or cool white dwarfs, derived distances and tangential velocities are given in Table 4.3. The differences between Chabrier et al. (2000b) and Richer et al. (2000) white dwarf colors are equivalent to absolute

magnitude differences of 0 to 0.5 mag. This corresponds to 0–25% difference in estimated distances and velocities with an average difference of about 10%.

### 4.2.3 Objects brighter than $V = 27$

Mendez & Minniti (2000) analyzed sources brighter than  $V=27$ , for which SExtractor gives reliable star–galaxy separation. The same sources have stellarity indices  $\geq 0.97$  in the GOODS data (Giavalisco et al. 2004) which has better spatial resolution than the original HDF images. The morphology of these sources as point-like is well supported. HDF2272, HDF2234, HDF101, HDF1583, HDF1828, HDF2134 and HDF2258 are further confirmed to be stars with Keck LRIS spectroscopy (Cohen et al. 2000).

We have searched the 503 X-ray point sources detected in the 2 Ms Chandra exposure of the region around the Hubble Deep Field North called the Chandra Deep Field North (Barger et al. 2003) for possible matches with the point sources analyzed here. We did not find any sources matching our objects within a search radius of  $0.5''$ ; we could not confirm if we had any quasars among our objects.

A comparison of the distances, tangential velocities, and photometric colors show that HDF1828, HDF2134, HDF2258, HDF1481, HDF684, and HDF3000 are halo main sequence stars (Table 4.3). Their  $V - I$  colors are too red to be white dwarfs. HDF2272, HDF101, HDF1583, and HDF1470 can be either main sequence stars or white dwarfs. Since we are sampling a larger volume for main sequence stars, these four stars are likely to be main sequence stars. Cohen et al. (2000) classified HDF2272 and HDF1583 as stars showing Mg absorption and Balmer lines, and HDF2234, HDF101, HDF1828, HDF2134 and HDF2258 as stars showing TiO or CaH bands.

HDF2234, HDF3072, HDF161, HDF3031, and HDF759 would have to be at very large distances and moving with velocities higher than the escape velocity of

Table 4.3: Photometric Distances and Tangential Velocities

Object	d(MS)	$\sigma_d$	$V_{tan}$ (MS)	$\sigma_v$	d(WD)	$\sigma_d$	$V_{tan}$ (WD)	$\sigma_v$	d(CWD)	$\sigma_d$	$V_{tan}$ (CWD)	$\sigma_v$
HDF2272	6194	141	263	73	100.0	1.0	4.24	1.18	29.65	0.04	1.26	0.35
HDF2234	61094	2339	2911	720	554.6	7.6	26.43	6.46	43.65	0.02	2.08	0.51
HDF101	11803	240	338	140	189.7	2.6	5.42	2.25	66.68	0.24	1.91	0.79
HDF1583	10965	177	603	117	115.3	2.4	6.34	1.23	...	...	...	...
HDF1828	10375	167	122	101	...	...	...	...	...	...	...	...
HDF3072	34674	630	2542	631	505.8	9.6	37.09	9.20	264.24	0.64	19.37	4.79
HDF2134	11015	178	172	139	...	...	...	...	...	...	...	...
HDF2258	7482	174	296	104	...	...	...	...	...	...	...	...
HDF1470	44874	1044	864	651	472.1	7.6	9.09	6.85	...	...	...	...
HDF1481	25119	553	1254	301	...	...	...	...	...	...	...	...
HDF161	214783	27485	1748	1575	2228.4	74.6	18.13	16.19	428.55	1.13	3.49	3.11
HDF684	58614	2236	1030	610	...	...	...	...	...	...	...	...
HDF3031	599791	55449	4359	7627	5128.6	513.7	37.27	65.23	594.29	1.65	4.32	7.55
HDF759	628058	58264	4079	7635	5248.1	566.2	34.08	63.83	639.73	1.80	4.15	7.77
HDF3000	15276	895	265	171	...	...	...	...	...	...	...	...
HDF995	580764	257760	3420	4756	5728.0	430.5	33.73	44.53	779.83	2.26	4.59	6.05
HDF1022	1.39e06	332181	21556	20807	12416.5	2541.7	192.56	184.34	1132.4	6.92	17.56	16.42
HDF861	2.28e06	1.65e06	24031	36146	19588.4	5296.6	206.46	277.90	1153.45	7.06	12.16	16.03
HDF1705	1.22e06	313129	21039	18175	10232.9	2995.5	176.47	154.46	1247.38	11.59	21.51	17.74
HDF2729	812831	302641	13276	9129	8053.8	1321.2	131.54	79.05	1386.76	13.07	22.65	13.10
HDF2217	1.55e06	546469	14754	21179	13740.4	3411.5	130.79	184.87	1348.96	16.89	12.84	17.87
HDF806	1.02e06	134633	5564	14085	10139.1	2030.9	55.30	140.26	1555.97	19.87	8.49	21.46
HDF1135	326588	111650	5341	3589	5128.6	1655.4	83.87	55.56	1995.26	151.44	32.63	19.04
HDF2991	2.06e06	780649	36825	34953	18793.2	6184.8	335.95	312.56	1577.61	20.18	28.20	24.54
HDF1288	4.79e06	6.39e06	80608	125961	30338.9	7070.9	510.55	432.17	1570.36	15.06	26.43	21.51
HDF723	508159	281257	6652	6889	7585.8	1206.8	99.30	88.34	1923.09	75.78	25.17	22.06
HDF1816	1.89e06	717666	49213	25202	15995.6	7053.9	416.51	232.85	1896.71	88.67	49.39	17.13
HDF1039	...	...	...	...	...	...	...	...	...	...	...	...
HDF774	3.89e06	4.61e06	88595	113808	31477.5	9203.1	716.90	412.59	1786.49	17.43	40.69	20.17

(1) Assuming that the object is either a main sequence star (MS), a white dwarf (WD), or a very cool white dwarf (CWD,  $T_{eff} \leq 3500K$ ).

(2) Distances are in parsecs, and velocities are in  $\text{km sec}^{-1}$ .

our Galaxy if they were main sequence stars. A comparison of the observed colors of HDF2234 with the white dwarf models shows that it is hotter than 10000 K. J. Cohen kindly provided us the Keck/LRIS spectrum for HDF2234. The same object is also observed by the Team Keck Treasury Redshift Survey (Wirth et al. 2004) who made their data publicly available. The object shows  $H\alpha$  at its rest wavelength; it is a star in our Galaxy. Although Cohen et al. (2000) classified this object as a late-type star showing CaH or TiO, its colors indicate that HDF2234 is too hot to show CaH and/or TiO. Absence of  $H\beta$  and Mg absorption eliminates the possibility of the object being a main sequence star. The star could be a cool DA white dwarf showing only  $H\alpha$ . However, the colors indicate that this should be a white dwarf hotter than 10,000 K which is inconsistent with such weak H lines, unless the star is a DC white dwarf at a position just too cool to show He I (11,000K) but then  $H\alpha$  alone cannot be explained. Follow-up spectroscopy of this object at Keck by Daniel Stern (2005; private communication) showed that it is a white dwarf.

HDF3072 displays even higher apparent proper motion than HDF2234,  $15.47 \pm 3.83$  mas yr<sup>-1</sup>. Its colors are consistent with a  $\sim 4500$  K white dwarf at  $d \approx 500$  pc. Follow-up low signal-to-noise spectroscopy by D. Stern showed that it is more likely to be a late type star.

The faint blue objects in Mendez & Minniti (2000) are HDF684, HDF161, HDF3031, HDF759, and HDF995. We have classified HDF684 as a main sequence star. The rest of the faint blue objects, HDF161, HDF3031, HDF759, and HDF995 do not seem to exhibit any proper motion. HDF161 is consistent with being a QSO under the given photometric uncertainties. Therefore we believe that HDF161, HDF3031 and HDF759 are probably AGN. These objects cannot be low-mass main sequence stars, brown dwarfs, or free floating planets due to their blue colors (see Chabrier et al. 2000a). Also, they cannot be comets or asteroids in our solar system due to their small proper motions (A. Cochran, private communication). Due to

the large errors in the estimated distance and velocity for HDF995, its nature is unclear.

#### 4.2.4 Objects with $27 \geq V \geq 29$

Star–galaxy separation becomes ambiguous below  $V \sim 27$ . Proper motions can be used to identify stars fainter than 27th magnitude since a moving object has to be in our Galaxy. We find that only two of the objects in our sample, HDF1816 and HDF774, have significant movement. These two objects are most likely Galactic white dwarfs. The rest of the faint objects do not show any significant movement ( $\mu/\sigma \leq 2$ ). For these objects, distances and velocities are consistent with halo white dwarfs or extragalactic sources. Mendez & Minniti (2000) found 566 extragalactic sources in the same magnitude and color range as the 5 faint blue sources that are brighter than 27th magnitude. The ratio of the number of extragalactic objects to the number of stars increases at fainter magnitudes. Therefore, we believe that the vast majority of the faint sources, with no significant apparent proper motion, are extragalactic objects.

#### 4.2.5 Previously Identified High Proper Motion Objects

Ibata et al. (1999) obtained second-epoch exposures of the HDF in 1997, and derived proper motions using a 2-year baseline. They found that two blue, faint objects displayed proper motions  $\sim 25 \text{ mas yr}^{-1}$  and three other stars at the detection limit of the second-epoch observations might be moving. Third epoch data on these objects showed that these objects are not moving (R. Ibata, private communication; Richer 2001).

Two of the objects in the Ibata et al. (1999) sample are in common with Mendez & Minniti (2000) objects. These two objects, HDF806 and HDF1816, have stellarities larger than 0.9, therefore are classified as stars by SExtractor. Mendez

& Minniti (2002) found that all objects with stellarity  $< 0.85$  are clearly extended, and used a conservative cut at stellarity  $> 0.90$  to identify point sources. We find that HDF806 and HDF1816 have proper motions of  $1.15 \pm 2.91 \text{ mas yr}^{-1}$  and  $5.49 \pm 1.89 \text{ mas yr}^{-1}$ , respectively. The other three objects are classified as galaxies by the SExtractor. Visual inspection of the first and second epoch images shows that these three objects are extended, and clearly not stars. We conclude that 3 of the objects (2-766, 4-141, 4-551) in the Ibata et al. (1999) sample are galaxies, HDF806 (2-455) is not moving, and HDF1816 (4-492) is probably moving ( $2.9 \sigma$  significance).

#### 4.2.6 Discussion

The nature of the faint blue objects in the Hubble Deep Field may be crucial to understanding the contribution of low luminosity halo white dwarfs to micro-lensing events and the dark matter content of the Galaxy. Apparent proper motions for 5 faint blue objects (Ibata et al. 1999) was enough to explain the entire missing mass in the halo of the Milky Way. Mendez & Minniti (2000) claimed that the faint blue objects are white dwarf stars located at heliocentric distances of up to 2 kpc and belong to the Galactic halo. They found a local halo white dwarf mass density of  $4.64 \times 10^{-3} M_{\odot} \text{ pc}^{-3}$ , which would account for about 30–50% of the dark matter in the Galaxy.

With the advantage of a 7-year baseline, we are able to place better limits on the proper motion measurements of the faint blue objects. Using the proper motion information, we also derived distances and tangential velocities for these objects. All of the main sequence stars exhibit halo kinematics and distances, whereas all of the likely white dwarfs exhibit disk kinematics and distances.

Following Gilmore, King, & van der Kruit (1989; see also von Hippel & Bothun 1990) we use the analytical form of the density profile for the thin disk and

thick disk

$$\frac{\nu_0(z)}{\nu_0(0)} = 0.96 e^{-z/250pc} + 0.04 e^{-z/1000pc} \quad (4.2)$$

with a local normalization of  $0.11 M_\odot \text{ pc}^{-3}$  (Pham 1997). We use the form

$$\nu_{halo}(r) \propto \frac{\exp[-7.669 (R/R_e)^{(1/4)}]}{(R/R_e)^{(7/8)}} \quad (4.3)$$

for the halo (Young 1976), where  $R$  is the distance from the Galactic center, and  $R_e$  is the scale factor.  $R$  is related to the distance  $r$  from the observer to a star by

$$R^2 = R_0^2 + r^2 - 2rR_0 \cos b \cos l \quad (4.4)$$

with  $R_0$  the solar Galactocentric distance, and  $b$  and  $l$  the Galactic coordinates for the HDF–North. We use  $R_0 = 7.8 \text{ kpc}$  (Gilmore, King, & van der Kruit 1989),  $R_e = 2.7 \text{ kpc}$  (de Vaucouleurs & Pence 1978) and a local normalization for the halo of  $(1/800) \times 0.11 M_\odot \text{ pc}^{-3}$  (Chen et al. 2001; Gilmore, King, & van der Kruit 1989). Using equations 4.2, 4.3, and 4.4, we calculated the expected number of stars in the HDF. We expect to find 2 thin disk, 3 thick disk, and 11 halo objects in the HDF–North.

We have also used Reid & Majewski (1993) star count models to predict the number of stars in the HDF–North. We found that 2 thin disk, 4 thick disk, and 14 halo objects are expected in the HDF–North. Both simple analytical models and more sophisticated star count models, when extrapolated to the photometric depth of the HDF, predict similar number of stars (16–20) in the HDF–North.

There are 14 stars brighter than  $V = 27$  and 17 objects fainter than  $V = 27$  classified as stars by SExtractor. The observed number of stars and the predictions of star count models are in good agreement for  $V \leq 27$  (see also Mendez et al. 1996 and Mendez & Minniti 2000). On the other hand, there seems to be an excess of point sources in the Hubble Deep Field – North for  $V \geq 27$ . Unfortunately,

SExtractor classification cannot be trusted at these magnitudes. Furthermore, we did not detect significant proper motion for all but two of these objects. The two faint, possibly moving objects, HDF774 and HDF1816, may be halo white dwarfs. One of the problems with any analysis using these objects is that the observations are beyond the completeness limit, and any calculation based on them is subject to a significant completeness correction. The rest of the objects fainter than  $V = 27$  are probably extragalactic objects.

The five faint blue objects analyzed by Mendez & Minniti (2000) do not exhibit any significant proper motion; they are not halo white dwarfs. These objects do not account for the MACHO optical depth and are not the source of the Galactic dark matter. Their stellar nature is not confirmed either. The colors of HDF161 are consistent with being a QSO. The faint blue objects may be distant AGN.

Holberg et al. (2002) used a local sample of white dwarfs complete out to 13 pc, and found the local mass density of white dwarf stars to be  $3.4 \pm 0.5 \times 10^{-3} M_{\odot} \text{ pc}^{-3}$ . Using this normalization factor in equations 4.2 and 4.3, we estimate the expected number of white dwarfs in the Hubble Deep Field. We expect to find 0.05 disk white dwarfs, 0.09 thick disk white dwarfs, and 0.33 halo white dwarfs in the Hubble Deep Field North. We have also used Reid & Majewski (1993) star count models to predict the number of white dwarfs in the HDF. The results are roughly consistent: 0.10 disk, 0.25 thick disk, and 0.5 halo white dwarfs are expected.

We have discovered only one white dwarf, HDF2234, brighter than  $V = 27$  in the HDF–North. It is located at a distance of  $\sim 500$  pc and have a tangential velocity  $\sim 30 \text{ km s}^{-1}$ . Its kinematic properties are consistent with being a thin disk or thick disk object (see Table 4.3). The expected number of thin disk + thick disk white dwarfs is found to be 0.14 – 0.35. Finding one white dwarf, when the expected number of white dwarfs is 0.14–0.35, is not surprising.

Mendez & Minniti (2000) have found 22 Galactic stars and 10 faint blue

objects in the Hubble Deep Field – South. A natural test to check the space density of disk and halo white dwarfs is to search for high proper motion objects in the HDF – South.

### 4.3 Hubble Deep Field South

The HDF South data provides another opportunity to test whether the faint blue objects in deep Hubble images can be old halo white dwarfs and if they can explain part of the Galactic dark matter. If the 10 faint blue objects discovered in the HDF South by Mendez & Minniti (2000) are halo white dwarfs, they would explain 30–50% of the dark matter in the solar neighborhood. We extend our work to the HDF South by using the original HDF South data and images of the same field taken 3 years later for the GO-9267 proposal (WFPC2 Supernova Search, PI: S. Beckwith) to measure the proper motions of the point sources in the HDF South.

The HDF South was imaged using the Wide Field Planetary Camera 2 (WFPC2) and the F300W ( $U_{300}$ ), F450W ( $B_{450}$ ), F606W ( $V_{606}$ ), and F814W ( $I_{814}$ ) filters in 1998, and imaged again in 2001 using the WFPC2 and the F814W filter in order to search for high redshift supernova. The original images taken in 1998 reach down to  $AB = 26.8, 27.7, 28.3$ , and  $27.7$  in the four bands, respectively ( $10\sigma$ , point source; Casertano et al. 2000). The (version 2) source catalogs for the first epoch are produced by the Space Telescope Science Institute (STScI) from the combined and drizzled images. Source detection was carried out on the inverse-variance-weighted sum of the F606W and F814W drizzled images. The combined F606W + F814W (hereafter  $V + I$ ) image is significantly deeper than any of the combined images (Casertano et al. 2000).

### 4.3.1 Identification of Point Sources

In our analysis of the point sources in the HDF North, we relied on Mendez & Minniti’s (2000) morphological classifications. Due to historical reasons, our analysis of the point sources in the HDF South differ slightly from the HDF North; we used a different criteria to identify the point sources in the HDF South. This slight difference between the analysis of HDF North and South does not affect our conclusions.

Mendez & Minniti (2000) used the stellarity index from Source Extractor (SExtractor; Bertin & Arnout 1996) to identify point sources and claimed that the star/galaxy separation is reliable for objects brighter than  $V + I = 29$ . They visually inspected the objects with stellarity index  $< 0.85$  and found that they are extended. Mendez & Minniti (2000) identified all objects with stellarity index  $> 0.90$  as stars, and found 98 point sources in  $4.062 \text{ arcmin}^2$  of the HDF South. They analyzed objects with  $I < 27$  ( $15\sigma$  detections) and found 22 late type stars and 10 faint blue objects.

Kilic et al. (2006d) showed that the SExtractor stellarity index fails at faint magnitudes. Instead, they suggested the use of the half light radius (R50) and the full width at half maximum (FWHM) measurements along with the empirical point spread function (PSF) distributions to identify the unresolved objects in deep HST images. Figure 4.3 shows the distribution of R50 with  $V + I$  magnitude for all HDFS objects (top panel) and for the objects with the stellarity index  $> 0.85$ . Objects brighter than  $V + I = 20$  are saturated and therefore have higher R50 and lower stellarity values. It is clear from this figure that the point sources are well separated from the extended objects in this diagram down to  $V + I = 28.5$ . A solid line (R50=3.0) marks the separation between the resolved and the unresolved objects. We note that we trimmed the source catalog to avoid spurious detections near the detector boundaries, and we also exclude the Planetary Camera (PC)

observations because the PC has a different plate scale and the PSFs are different from the PSFs for the Wide Field Cameras.

We use the IRAF task PRADPROF and the object centroids from Source Extractor to plot the radial profile of each object (see Kilic et al. 2005 for radial profiles). A comparison of the PSF for each object with our template PSF (for a bright unsaturated and unresolved source, HDFS 10617) shows that HDFS 126 (FWHM=6.03), 2003 (FWHM=5.38), and 497 (FWHM=5.28) are clearly resolved. The typical FWHM for the unresolved objects is  $< 5$ . In addition, HDFS 1812, 1827, 2129, and 567 have shallower PSF distributions than the template PSF, therefore are resolved, as well. Six of these seven objects have stellarity indices larger than 0.9, therefore would be classified as point sources based on the stellarity index. Our empirical PSF distribution analysis shows that the stellarity index from the SExtractor should not be used by itself to identify point sources in deep HST images. Instead, as Kilic et al. (2006d) suggested, a combination of the R50, FWHM, stellarity index, and empirical PSF distributions is required to identify unresolved objects. This analysis leaves us with 39 unresolved objects with  $21 < V + I < 28.5$ , and  $I < 27$ , plus 7 brighter point sources ( $V + I < 21$ ) in the HDF South.

We note that we may have a few barely resolved objects in our sample, e.g. HDFS 191. Some extra galactic sources, e.g. Luminous Compact Blue Galaxies (LCBGs), can be quite small (half light radius=1–3 kpc) and blue ( $B - V < 0.6$ ; Werk et al. 2004). Nevertheless, HST is able to resolve almost every galaxy if enough signal to noise is obtained. For example, Hoyos et al. (2004) could resolve four LCBGs at intermediate redshifts ( $z=0.1-0.44$ ,  $R50 = 0.7-2.7$  kpc) using WFPC2 ( $R50 = 0.23'' - 0.47''$ ). In addition, using low resolution spectroscopy from the GRAPES survey, Pirzkal et al. (2005) showed that none of the unresolved objects in the HUDF ( $I < 27$ ) are LCBGs. Therefore, the number of compact galaxies that are classified as unresolved should be small. Even if our sample is contaminated by

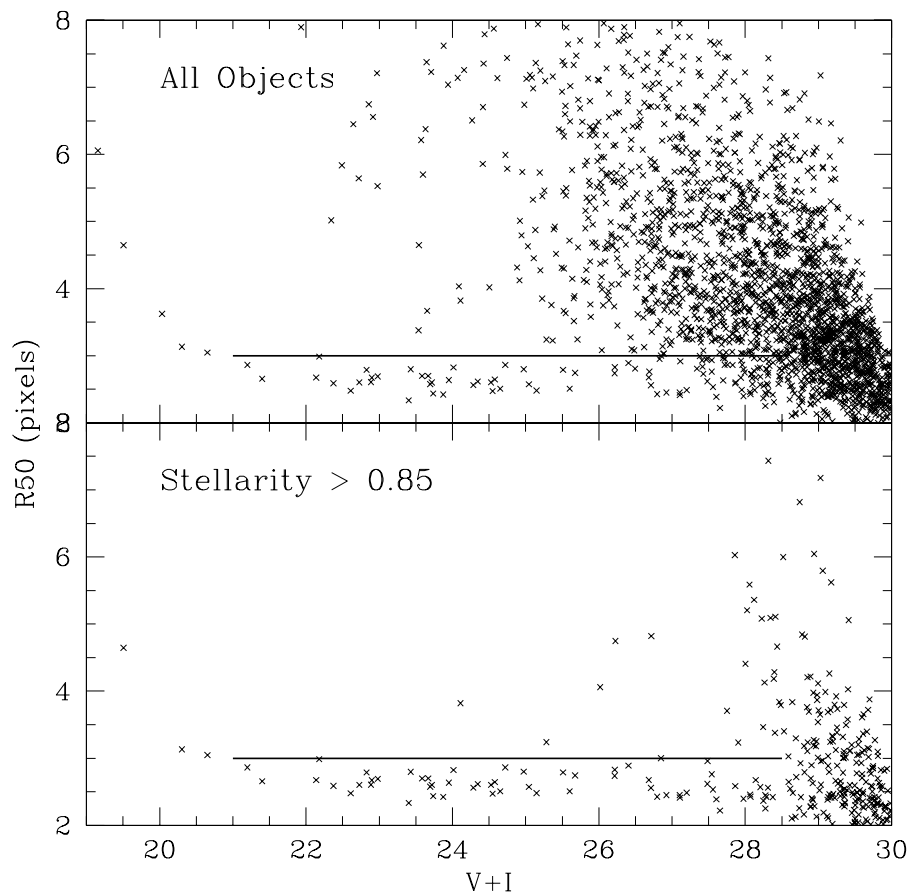


Figure 4.3: The distribution of R50 (half light radius) for the HDF South objects. The solid line separates the unresolved objects from the resolved objects.

a few faint resolved objects, misclassification of these objects would not change the conclusions derived from our analysis (see §4.4).

All of the unresolved objects in the HDFS ( $V + I > 21$ ) have stellarity index  $> 0.87$ ,  $R50 < 3$ , and  $FWHM < 5$ . The unresolved objects can be identified easily down to  $V + I = 27$ . Even though, the classification becomes harder for  $V + I > 27$ , five of the six objects that are fainter than  $V + I = 27$  and classified as unresolved (HDFS 261, 441, 1020, 1306, and 2178) all have PSFs,  $R50$ ,  $FWHM$ , and the stellarity values consistent with unresolved objects. Therefore, their identification as point sources is secure. The identification of HDFS 2488 ( $R50 = 2.96$ ,  $I = 26.97$ ) as unresolved is questionable, but still included in our analysis for completeness purposes. Astrometric and photometric data for the 46 objects that we identified as unresolved are given in Table 4.4. We adopted the calibrated photometry of Casertano et al. (2000).

### 4.3.2 The HDFS Second Epoch Data

The second epoch data consist of thirty six 1200 sec images in the F814W filter, and provide a baseline of 3 years. The  $10\sigma$  limiting magnitude for the point sources in the combined second epoch image is  $AB = 26.7$ .

We followed the reduction steps outlined in the HST dither handbook (Koeke-moer et al. 2002) to reduce the second epoch data. All 36 images were processed with a procedure that included the following steps: initial pipeline processing, sky background subtraction, cross-correlation and finding the offsets between images, cosmic-ray rejection, scattered-light correction, and final drizzling and combination.

We obtained the standard pipeline processed images of the HDFS 2001 observations from the Space Telescope Science Institute website. After subtracting the sky background from each image, cosmic rays were removed so that cross-correlation would not be affected by them. Each image is cross correlated with the first image

Table 4.4: Point Sources in the Hubble Deep Field South

No	Object	X(HDFS)	Y(HDFS)	$U_{300}$	$B_{450}$	$V_{606}$	$I_{814}$	Stellarity
10663	J223250.50-603400.8	3039.857	884.384	23.43	19.90	19.13	18.20	0.72
10692	J223257.00-603405.7	1836.189	772.533	20.89	19.14	19.22	18.61	0.94
10017	J223254.90-603144.1	2255.468	4321.344	24.99	21.47	20.26	18.75	0.78
10666	J223305.04-603400.8	350.133	907.811	25.62	21.80	20.52	19.24	0.99
10151	J223250.51-603218.8	3059.869	3445.525	21.76	20.25	20.35	19.87	0.99
10081	J223247.45-603160.0	3632.237	3911.988	27.14	23.93	22.23	19.89	0.89
1576	J223303.65-603330.6	614.027	1664.433	28.93	23.45	21.92	20.23	0.98
2257	J223305.63-603358.2	242.259	974.553	...	24.50	22.87	21.15	0.99
10617	J223258.30-603351.7	1599.243	1127.375	29.19	25.26	23.55	21.36	0.98
86	J223248.06-603148.6	3521.148	4199.046	23.98	22.24	21.76	21.46	0.94
15	J223248.47-603139.3	3447.529	4431.511	27.51	24.78	23.28	21.59	0.96
2041	J223251.03-603353.5	2942.939	1069.948	28.28	25.97	24.16	21.68	0.99
10326	J223252.60-603259.5	2664.651	2425.551	27.64	24.45	22.87	21.71	0.98
701	J223251.33-603237.6	2903.785	2973.677	29.04	24.80	23.24	21.78	0.96
1922	J223247.58-603347.3	3583.103	1217.824	...	24.67	23.05	21.87	0.88
1209	J223245.74-603309.7	3931.750	2158.995	...	26.93	24.75	22.24	0.98
1257	J223256.68-603313.8	1906.621	2075.463	...	26.21	24.56	22.46	0.97
431	J223247.94-603216.6	3537.732	3496.018	25.68	23.69	23.14	22.69	0.93
1187	J223258.46-603307.7	1578.305	2231.191	28.61	25.28	23.79	22.74	0.99
2469	J223253.24-603413.4	2529.645	574.651	26.26	23.89	23.22	22.83	0.98
323	J223246.71-603207.2	3765.987	3728.892	26.20	24.07	23.41	22.97	0.98
108	J223249.34-603149.0	3284.156	4189.406	27.78	25.54	24.01	22.97	0.98
1444	J223258.77-603323.5	1517.394	1833.822	23.30	22.69	22.80	23.02	0.97
2364	J223257.72-603408.7	1702.207	699.988	28.80	27.21	25.31	23.04	0.98
1724	J223258.11-603337.4	1637.423	1485.485	26.72	24.26	23.60	23.12	0.98
1386	J223248.36-603319.0	3444.716	1930.820	28.01	24.99	23.86	23.16	0.94
933	J223247.94-603251.1	3528.871	2630.077	...	26.35	24.75	23.24	0.98
2072	J223255.36-603355.0	2142.223	1039.552	27.33	26.90	25.45	23.31	0.98
1331	J223247.05-603316.0	3687.492	2003.460	28.08	26.35	24.68	23.50	0.98
316	J223253.09-603206.7	2584.979	3752.969	29.53	26.00	24.57	23.75	0.98
1010	J223256.14-603256.9	2011.083	2498.703	27.27	24.84	24.23	23.78	0.98
1426	J223304.54-603322.5	450.919	1867.914	30.99	26.48	25.04	24.10	0.99
652	J223251.18-603234.0	2933.967	3064.594	28.54	26.14	24.98	24.30	0.99
191	J223256.17-603156.5	2018.212	4011.988	...	28.28	26.82	24.41	0.95
1302	J223252.60-603315.1	2661.049	2035.617	...	27.28	25.58	24.66	0.99
895	J223246.22-603248.4	3847.227	2693.725	28.08	26.20	25.77	25.57	0.99
2615	J223258.88-603421.9	1485.890	368.651	25.45	25.17	26.91	25.69	0.98
1945	J223249.59-603347.7	3211.154	1212.031	26.23	26.53	26.46	25.88	0.97
2007	J223249.63-603351.3	3201.802	1122.227	29.13	28.72	26.69	25.92	0.99
2596	J223254.05-603419.4	2378.829	425.350	...	27.73	26.89	26.00	0.99
441	J223255.01-603217.7	2228.504	3480.124	29.78	28.34	27.12	26.14	0.98
1020	J223254.03-603257.4	2400.755	2481.265	29.20	28.83	27.12	26.29	0.98
2178	J223258.94-603400.1	1478.979	917.399	28.73	28.41	26.71	26.47	0.98
261	J223248.69-603200.8	3402.451	3893.844	31.80	28.74	27.86	26.91	0.87
1306	J223258.20-603315.2	1625.787	2040.621	29.73	...	28.47	26.93	0.98
2488	J223245.71-603413.4	3922.570	561.776	28.20	26.45	26.65	26.97	0.97

(reference image) in order to determine the shifts between them. Most hot pixels, i.e., pixels with elevated dark current, can be identified easily with images taken in different dither positions. Nevertheless, some hot pixels may escape detection if they fall near an object. We use the static pixel mask reference file, used in pipeline calibration, to create a bad pixel mask for our images.

The cosmic-ray rejection is done in three steps. Each individual input image is registered and drizzled to the same output frame. Ten of the 36 images have a higher background and suffer from a distinctive cross-shaped pattern due to the shadowing of the HST secondary by the support structure of the WFPC2 repeater (Casertano et al. 2000). The 26 images without the scattered light problem are combined into a single cosmic-ray-free median image for each chip. The median image is then blotted back (reverse drizzling) to the original position of each input image. Images with the cross pattern were corrected by applying a median filter to the image obtained after subtracting the expected image produced by the BLOT task. Inspection of the resulting images showed that the subtraction works well. In addition, each image is compared with the blotted images to identify and mask cosmic rays and bad pixels.

The final drizzled images are constructed by applying the shifts and the mask files to the individual images, and are combined into a single image for each WFPC2 chip. The parameters chosen for the final drizzling were similar to those used for the HDFS 1998 images. We used a footprint area of 0.6 input pixels (0.5 for the HDFS 1998 images), and a pixel scale of 0.4 pixels, resulting in a linear scale of  $0.04 \text{ arcsec pixel}^{-1}$ . Our experimentation with different values of the footprint for the drizzling algorithm showed that image statistics are better for a footprint of 0.6 pixels. Because of the relatively small pointing shifts, we decided not to combine all images into a single mosaic comprising all four WFPC2 chips. The pointing shifts are not large enough to recover part of the sky that is lost between the WFPC2

chips.

### **Object Identification and Proper Motion Measurements**

Casertano et al. (2000) used the SExtractor package to create source catalogs for the HDF South 1998 images. We have created source catalogs for the second epoch data using SExtractor, version 2.3, with the same parameters used for the HDF South original images. We set the source detection threshold to 0.65 and the minimum area to 16 drizzled pixels. We convolve the image with a Gaussian ( $\text{FWHM} = 3$  pixels) and sources with 16 pixels above the detection threshold are included in our catalog. Only those objects matching the positions of the objects in the first-epoch data with differences less than 1 pixel ( $0.04''$ ) are included in our final catalog of reference compact objects. Furthermore, we visually inspected all of these sources to avoid any mismatches. We note that the 1 pixel limit is only used for the reference compact objects, as we do not impose any limits on the proper motion of the point sources.

To select reference objects, we use all of the compact objects (isolated, low residuals, and not fuzzy) with positional differences less than 1 pixel ( $0.04''$ ) between the two epochs to derive a quadratic (third order two dimensional polynomial) transformation for each chip (WF2, WF3, and WF4). We rejected deviant points using a  $3\sigma$  rejection algorithm. This rejection is required because our reference objects are compact galaxies and centroiding errors are larger for galaxies. Even though using a local transformation for each object can increase the accuracy of our proper motion measurements, some of the point sources are near the edges of the chip, therefore it is not possible to perform a local transformation for each object. Our transformation solutions for individual chips are still better than doing a global transformation using a single mosaic image. After mapping the distortions with the GEOMAP package, coordinates for the compact objects and the point sources were

transformed to the second-epoch positions with the GEOXYTRAN routine.

### 4.3.3 Results

Our proper motion measurements for the point sources in the HDF South and their significances ( $\mu/\sigma$ ) are given in Table 4.5. Typical errors in our measurements are 7-8 mas yr<sup>-1</sup>. Hence, only those objects having proper motions larger than 15 mas yr<sup>-1</sup> have significance greater than  $2\sigma$ . Our errors in proper motion measurements for the objects in the HDF South are larger than that of HDF North objects due to the fact that the time difference between the first and second epoch images is only 3 years versus 7 years for the HDF North. There are 9 point sources with  $\mu/\sigma \geq 2$  in our sample, and four of these stars (HDFS 10081, 10617, 2072, and 895) display significant ( $\mu/\sigma \geq 3$ ) proper motion.

Figure 4.4 shows the observed shifts of all point sources along with the Galactic coordinates. Halo objects rotate around the Galactic center more slowly than disk stars like the Sun. Solar motion relative to the halo objects corresponds to a speed of  $\sim 200$  km s<sup>-1</sup> in the direction  $l = 90^\circ$ ,  $b = 0^\circ$  (Mihalas & Binney 1981). Therefore, halo objects are expected to lag behind the disk objects in the opposite direction to the rotation direction of the Sun ( $l$ ). Even though the reference compact objects show a symmetric distribution around the origin, most of the point sources in the HDF South are located in the lower left quadrant of Figure 4.4; the majority of them lag behind the Sun, therefore are likely to be halo objects.

Halo stars are expected to have large proper motions as a result of their high velocities relative to the Sun. Mendez & Minniti (2000) claimed that the faint blue objects in the HDF South could be ancient halo white dwarfs with distances, based on consistency with white dwarf absolute magnitudes, less than about 2 kpc from the Sun. Assuming  $V_{\text{tan}} = 200$  km s<sup>-1</sup> for a halo star at a distance  $\leq 2$  kpc, we would expect to measure a proper motion of  $\geq 21$  mas yr<sup>-1</sup> for the faint blue

Table 4.5: Proper Motions

Object	Chip	$\mu_x$ (pixel)	$\mu_y$ (pixel)	$\mu$ (mas/yr)	$\sigma_\mu$ (mas/yr)	$\mu/\sigma$
10663	wf3	-0.67	-0.58	11.82	7.04	1.68
10692	wf2	0.00	-0.41	5.50	7.93	0.69
10666	wf2	-0.68	-0.30	9.85	7.93	1.24
10151	wf4	-0.04	-0.29	3.94	8.00	0.49
10081	wf4	-1.89	-0.84	27.58	8.00	3.44
1576	wf2	-1.57	-0.23	21.17	7.93	2.67
10617	wf2	-1.54	-0.94	24.01	7.93	3.03
86	wf4	-0.11	-0.30	4.21	8.00	0.53
2041	wf3	0.11	0.47	6.47	7.04	0.92
10326	wf4	0.23	-1.48	20.00	8.00	2.50
701	wf4	-0.31	-1.08	14.94	8.00	1.87
1922	wf3	0.55	-1.20	17.57	7.04	2.50
1257	wf2	-0.33	-0.64	9.56	7.93	1.21
431	wf4	0.17	0.12	2.79	8.00	0.35
2469	wf3	-0.29	-0.33	5.86	7.04	0.83
323	wf4	0.26	-0.35	5.83	8.00	0.73
108	wf4	-0.92	-0.39	13.33	8.00	1.67
1444	wf2	0.05	-1.58	21.07	7.93	2.66
2364	wf2	-0.03	-0.20	2.70	7.93	0.34
1724	wf2	-0.10	-0.32	4.48	7.93	0.56
1386	wf3	-0.82	-0.15	11.07	7.04	1.57
933	wf4	-0.19	-0.44	6.47	8.00	0.81
2072	wf3	-1.38	-0.80	21.28	7.04	3.02
1331	wf3	-0.21	-0.55	7.83	7.04	1.11
316	wf4	-0.10	-0.38	5.29	8.00	0.66
1426	wf2	-0.91	-0.45	13.50	7.93	1.70
652	wf4	-0.31	-0.36	6.32	8.00	0.79
191	wf4	-0.98	-0.78	16.73	8.00	2.09
1302	wf3	-0.34	-0.20	5.22	7.04	0.74
895	wf4	-0.34	-2.60	34.90	8.00	4.36
2615	wf2	0.32	-0.48	7.62	7.93	0.96
1945	wf3	0.30	0.21	4.91	7.04	0.70
2007	wf3	-0.15	-0.17	3.03	7.04	0.43
2596	wf3	-0.03	-0.14	1.90	7.04	0.27
441	wf4	-0.75	-0.19	10.27	8.00	1.28
1020	wf4	-0.44	-0.57	9.63	8.00	1.20
2178	wf2	0.14	-0.13	2.56	7.93	0.32
261	wf4	0.35	-0.27	5.94	8.00	0.74
1306	wf2	-0.54	0.09	7.34	7.93	0.93
2488	wf3	-0.38	-0.17	5.60	7.04	0.80

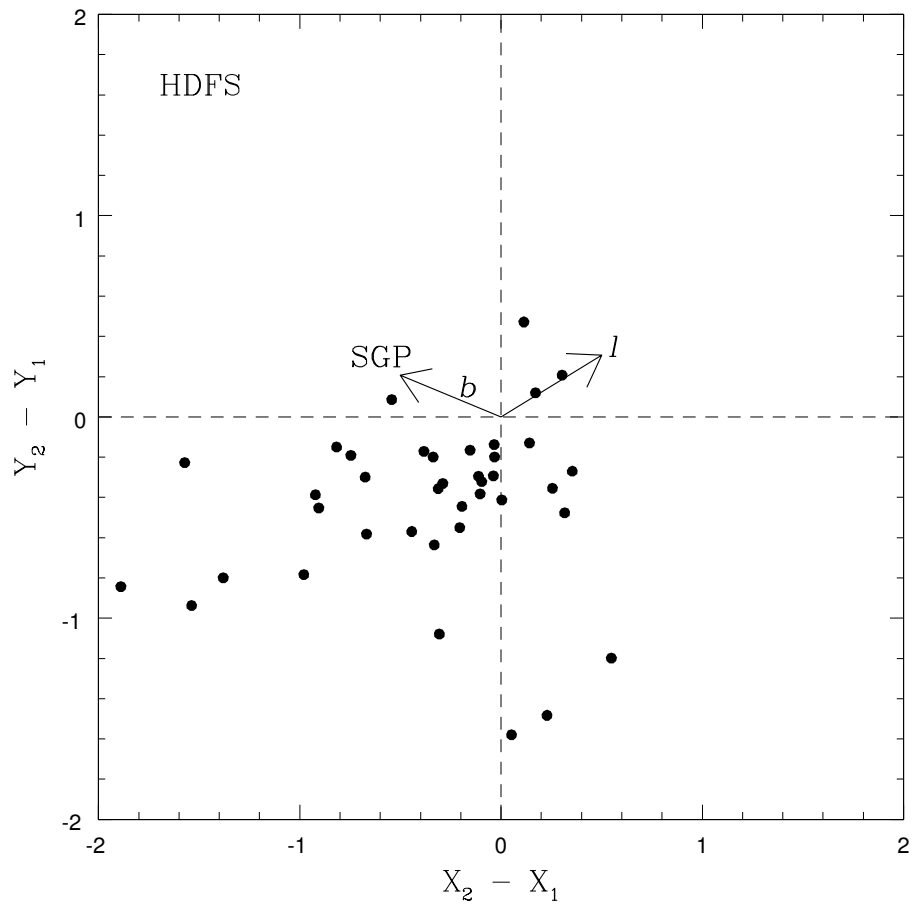


Figure 4.4: Observed shifts of all point sources in the HDF South.  $\Delta X = 1$  corresponds to 40 mas. The directions of increasing Galactic longitude ( $l$ ) and latitude ( $b$ ) and the South Galactic Pole (SGP) are also shown.

objects. Nine of the faint blue objects identified by Mendez & Minniti (HDFS 1812, 1827, 1945, 2007, 2178, 441, 1020, 261, 1332) have proper motions in the range 2.26 to  $10.27 \text{ mas yr}^{-1}$ , therefore are not likely to be halo white dwarfs. The remaining object, HDFS 1444, exhibits a significant proper motion,  $21.07 \pm 7.93 \text{ mas yr}^{-1}$ , and is likely to be either a thick disk or a halo object. If the majority of these faint blue objects are not halo white dwarfs, what are they?

It is always desirable to obtain spectroscopy of star-like objects to distinguish quasars from stars, and also to determine the spectral types of stars in order to have a reliable estimate of their absolute magnitudes and kinematic properties. Unfortunately, the most interesting point sources in deep Hubble images are the faintest, therefore the hardest ones for which to obtain spectroscopy. There is only one deep field, the Hubble Ultra Deep Field (HUDF), that is studied spectroscopically to very faint magnitudes ( $I \leq 27$ ; Pirzkal et al. 2005). Pirzkal et al. (2005) found 28 point sources in the HUDF, including 2 quasars (and two more quasars with  $I > 27$ ). Even though spectroscopy is superior to spectral energy distribution fitting using photometry, we can identify the quasars and the stars in the HUDF from their photometry. Using the IRAF package CALCPHOT, which is designed for simulating the HST observations, Kilic et al. (2006d) showed that spectral energy distribution (SED) fitting can be used to identify quasars, and to assign spectral types to stars. Their classifications for the stars agreed reasonably well with the Pirzkal et al. (2005) spectroscopic classifications, and they were also able to predict the redshifts of two of the quasars correctly, whereas the other two were predicted to be at lower redshifts than the spectroscopic redshift measurements.

Here we adopt the same SED fitting procedures used by Kilic et al. (2006d). We use Pickles (1998) stellar templates and the composite-quasar spectrum from the Sloan Digital Sky Survey (Vanden Berk et al. 2001) to simulate SEDs in  $U_{300}$ ,  $B_{450}$ ,  $V_{606}$ , and  $I_{814}$  using the CALCPHOT task. Our simulations include stellar

templates from O5 to M6 dwarf stars, and the composite quasar spectrum is used to simulate the colors for quasars up to  $z = 4.8$ . Note that we do not simulate the colors of the broad range of galaxy types, as almost every galaxy with sufficient signal-to-noise is resolved by HST (e.g. 2 kpc at  $z = 0.5$  projects to  $0.33''$  for  $\Omega_o = 0.3$ ,  $\Lambda_o = 0.7$ , and  $H_o = 70$ ).

The observed magnitudes for the faint blue objects are converted to  $F_\nu$ , normalized at  $V_{606}$ , and compared with our simulated SEDs. We assign spectral types to each object using a  $\chi^2$  minimization technique. Each photometry point is weighted according to its error bar, but we also tried giving equal weights to each photometric band to explore possible fits. We found that there are 4 point-like sources with SEDs better explained by quasars than stars. HDF5 10151 ( $z = 2.0$ ), 1945 ( $z = 0.2$ ), 2007 ( $z = 4.7$ ), and 2178 ( $z = 4.0$ ) have colors more consistent with being quasars. Interestingly enough, three of these objects were classified as possible halo white dwarf candidates by Mendez & Minniti (2000). These four objects have proper motions in the range  $2.56 - 4.91 \pm 8 \text{ mas yr}^{-1}$ , and are not moving (within the errors); they demonstrate that our proper motion measurements are reliable.

#### 4.3.4 Discussion

We identified 4 quasars and 42 stars, including 36 K0 or later type stars, with our SED fitting technique. We adopt the absolute magnitude ( $M_V$ ) for each spectral type from Pickles (1998). We use the  $M_V$  for each object to simulate the absolute magnitudes in the WFPC2 F606W filter ( $M_{F606W}$ ). We calculated photometric distances for all of the objects in our sample using the simulated  $M_{F606W}$  and the observed  $V_{606}$  magnitudes. Combining our proper motion measurements with photometric distances, we are able to derive tangential velocities for the stars. The photometric errors for the point sources in the HDF South are small, hence they cause only relatively small errors in the estimated distances. On the other hand, if

the assigned spectral types are wrong by one subclass (for example M3 instead of M2), then the absolute magnitudes could be wrong by as much as 1 magnitude. We also note that our stellar templates have approximately solar metallicity. Therefore, the distances to the metal poor halo objects, which will be intrinsically fainter for the same spectral type, may be over-estimated by our SED fitting method. For example, a metal poor G0 dwarf ( $[\text{Fe}/\text{H}] = -0.8$ ) would be 0.5 magnitude fainter than a solar metallicity G0 star (Pickles 1998). Hence, the distance to a metal poor G0 type star would be over-estimated by 26%.

In order to determine the effect of different metallicity, we use synthetic spectra from a PHOENIX model atmosphere grid (Brott & Hauschildt 2005) for stars with  $2000 \text{ K} \leq T_{\text{eff}} \leq 10000 \text{ K}$ ,  $[\text{M}/\text{H}] = 0.0, -0.5, -2.0$ , and  $\log g = 4.5$  to simulate photometric colors in the HST bands. We found that using different metallicities changes the best fit  $T_{\text{eff}}$  by 50 – 450 K for G0 and later type stars, and the spectral types obtained from metal poor atmosphere models are usually 1-2 subclass later in spectral types, e.g. M2 instead of M0, than the ones obtained from the models with solar metallicity. We also used Kurucz model atmospheres (Kurucz 1995) with  $3500 \text{ K} \leq T_{\text{eff}} \leq 6000 \text{ K}$  to test the metallicity effect, and found similar results. Using Girardi et al. (2002) theoretical isochrones, we estimate  $M_V$  and  $M_{\text{F606W}}$  for different metallicities for the point sources in our sample. Spectral types from the SED fitting procedure (using the Pickles library), estimated absolute magnitudes, derived distances, and tangential velocities are given in Table 4.6. The ranges of absolute magnitudes, distances, and tangential velocities show the effect of using models with different metallicities. Despite these potential systematic errors, the total information we have available for the point sources (the morphological information, proper motion measurements, and the SED fitting results) is sufficient to determine their nature.

Table 4.6: Spectral Types, Photometric Distances, and Tangential Velocities

Object	Type	$M_{F606W}$	$d(\text{kpc})$	$V_{\text{tan}}(\text{km/s})$
10663	K1-M0	5.73–8.25	1.5–4.8	84–269
10692	A3-4	1.42–4.97	7.1–36.4	189–948
10017	K5-6	7.33–10.58	0.9–3.9	...
10666	M2	9.17–11.09	0.8–1.9	36–87
10081	M5	12.18–12.46	0.9–1.0	118–134
1576	M3	10.19–12.56	0.7–2.2	75–222
2257	M3	10.19–12.56	1.2–3.4	...
10617	M5	12.18–12.46	1.7–1.9	188–214
86	G3	4.65–6.44	12.0–26.4	240–527
15	M3	10.19–12.56	1.4–4.2	...
2041	M5	12.18–12.46	2.2–2.5	67–76
10326	M2	9.17–11.09	2.3–5.5	216–522
701	M2.5	9.68–11.70	2.0–5.2	144–365
1922	M2	9.17–11.09	2.5–6.0	206–498
1209	M6	10.86–13.56	1.7–6.0	...
1257	M5	12.18–12.46	2.6–3.0	119–136
431	K1	5.73–7.24	15.1–30.3	200–400
1187	M1	8.69–11.14	3.4–10.5	...
2469	K1	5.73–7.21	15.9–31.5	442–874
323	K1-3	5.73–7.43	15.7–34.4	434–949
108	M1	8.69–11.14	3.7–11.6	237–731
1444	B8-9	-1.39 – -0.09	379.2–690.0	37875–68921
1444	WD	11.95	1.482	$148 \pm 56$
2364	M5	12.18–12.46	3.7–4.2	48–54
1724	K3	6.58–7.68	15.2–25.3	324–537
1386	K6	7.59–10.64	4.4–18.0	231–942
933	M3	10.19–12.00	3.6–8.2	109–251
2072	M5	12.18–12.46	4.0–4.5	399–454
1331	M2	9.17–11.09	5.2–12.6	194–469
316	K7	7.86–11.15	4.8–22.0	121–552
1010	K3	6.58–7.41	23.1–33.9	...
1426	M0	8.25–11.13	6.1–22.8	388–1460
652	K6	7.59–10.50	7.9–30.1	236–901
191	M5	12.18–12.46	7.4–8.5	589–670
1302	M0	8.25–11.13	7.8–29.3	193–725
895	G0	4.18–5.98	93.5–208.4	15469–34471
895	WD	14.17	2.094	$346 \pm 79$
2615	O9-M2	-4.32–11.09	14.6–17600	527–636472
2596	M0	8.25–11.13	14.2–53.3	127–479
441	M0	8.25–11.13	15.7–59.3	766–2886
1020	K7	7.86–11.15	15.6–71.1	713–3244
261	M0	8.25–11.13	22.2–83.5	623–2349
1306	M3	10.19–12.18	18.1–45.4	631–1577
2488	A0-1	0.71–1.00	1350–1540	35803–40918
2488	WD	11.86	9.070	$241 \pm 303$

## Late Type Stars in the Galaxy

Figure 4.5 shows the histogram of the number of stars observed at a given distance in the HDF South along with the predictions from the star count models (Reid & Majewski 1993; dashed line) and the observed distribution of stars in the HUDF (Pirzkal et al. 2005; solid line). The top panel shows the distribution of stars if we use the Pickles main sequence spectral library, and the bottom panel shows the same distribution if we use synthetic spectra with  $[M/H] = -2.0$  (halo-like metallicity). Both panels show that there is a deficit of stars in the 5–15 kpc range in the HDF South compared to the star count models.

If we assume that all of the stars in the HDF South have solar metallicity, then we see an excess number of stars at  $\sim 35$  kpc, and 4 more stars (HDFS 441, 1020, 2596, and 261) with estimated distances larger than 50 kpc, which is not expected from the star count models, nor would the distances be consistent with the metallicities for Galactic stars. Most of the objects observed at  $\sim 35$  kpc are K type stars, whereas the four objects with distances  $> 50$  kpc fit late type star SEDs fairly well, and they have essentially the same spectral type (K7-M0). If we assume that their classification as point sources is reliable, our SED fitting procedure works well to identify quasars and stars, and that they have solar metallicity, then we could claim that we discovered two new populations of stars; a cluster of stars at 35 kpc and several other stars at  $> 50$  kpc.

HDF South and HUDF have similar Galactic latitudes ( $-49.21$  and  $-54.39$ , respectively), therefore they should have similar distributions of Galactic objects. We do not find any stars with distances larger than 50 kpc in the HDF North or the HUDF. Even though HDF South ( $l = 328.25$ ,  $b = -49.21$ ) is about  $25^\circ$  away from the center of the Small Magellanic Cloud (SMC;  $l = 302.80$ ,  $b = -44.31$ ), the Magellanic Stream has over dense regions near the HDF South ( $1 \times 10^{19}$  atoms  $\text{cm}^{-2}$ ; see the HI surface density maps of Mathewson & Ford 1984). The average

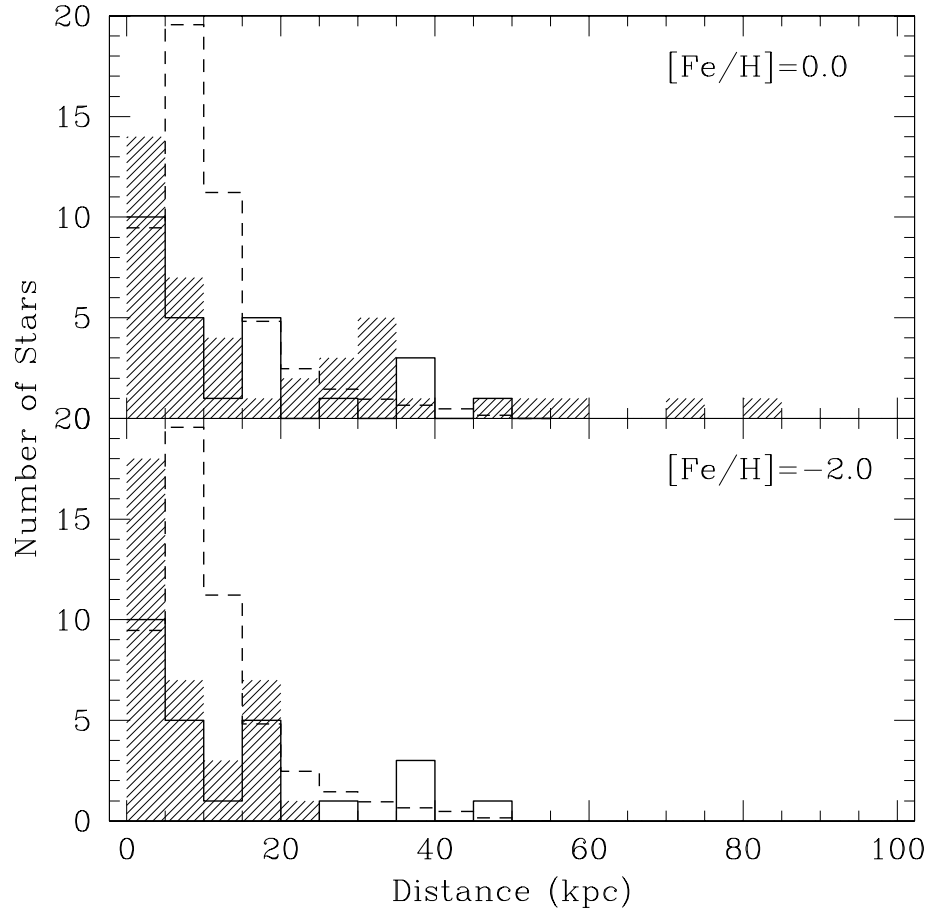


Figure 4.5: Histogram of the number of stars observed at a given distance in the HDF South (shaded histogram) assuming solar (top panel) or metal poor composition (bottom panel). The histogram of the number of stars observed in the HUDF (solid line) and the predictions from the star count models (dashed-dotted line) are also shown.

distance to the 4 objects with  $d > 50$  kpc is  $66.8 \pm 13.4$  kpc (assuming solar metallicity), whereas the distance to the SMC is measured to be  $60.6 \pm 3.8$  kpc (Hilditch, Howarth, & Harries 2005). Can these objects be members of the SMC? Assuming that they have metallicities similar to the SMC ( $[\text{Fe}/\text{H}] = -0.7$ ; Lennon 1999), we estimate their average distance to be  $17.8 \pm 3.4$  kpc, therefore they are not consistent with being in the SMC.

We expect the majority of the stars in the HDF South to be halo stars (from the star count models and the velocity distribution of Figure 4.4). Therefore, the bottom panel of Figure 4.5 is likely to represent the real distribution of stars better than the top panel. A comparison of the distances, tangential velocities, and photometric colors show that all of the 42 stars except three (HDFS 1444, 895, and 2488) are consistent with being dwarf/subdwarf stars in the Galaxy. Seven of these 42 stars (HDFS 191, 1576, 1922, 2072, 10081, 10326, and 10617) show significant proper motion ( $\mu/\sigma \geq 2$ ) and have spectral types M2–M5, therefore are probable halo M dwarfs. Large errors in our proper motion measurements prevent us from classifying the kinematic properties of the other stars, nevertheless, they are most likely to be G0 and later type dwarfs in the thick disk or halo of the Galaxy. The three stars (HDFS 1444, 895, and 2488) with estimated distances larger than 90 kpc (both for the metal rich and the metal poor case) are discussed in the next section.

## White Dwarfs

HDFS 1444, 895, and 2488 would have to be at very large distances ( $> 90$  kpc) if they were main-sequence stars of any metallicity. On the other hand, as white dwarfs, they would be at more reasonable distances. In order to find the temperatures of these objects, we simulated the colors for blackbody SEDs with temperatures in the range 3000 – 80000 K. We calculate the blackbody temperatures for these objects to be 10547 K, 6096 K, and 10463 K, respectively. We have also used pure H white

dwarf model atmospheres (D. Saumon and D. Koester, private communication) to simulate colors for white dwarfs with  $\log g = 8$  and  $3000 \text{ K} \leq T_{\text{eff}} \leq 20000 \text{ K}$ . The pure H white dwarf models that we used include the CIA opacities, therefore, we are able to compare the spectral energy distributions of young and old white dwarfs simultaneously and find the best-fit solution for our white dwarf candidates. Assuming that HDFS 1444, 895, and 2488 are pure-H atmosphere white dwarfs, we estimate the temperatures of these objects to be 10681 K, 5882 K, and 11000 K, respectively.

Using our best fit DA white dwarf atmosphere solutions, we estimate the absolute magnitudes for our white dwarf candidates using the tables from Bergeron et al. (1995). We use the white dwarf models to predict  $M_{\text{F606W}}$ , and therefore to calculate the distances and tangential velocities for these three objects. HDFS 1444 displays a significant proper motion,  $21.07 \pm 7.93 \text{ mas yr}^{-1}$ , and is consistent with being a thick disk or halo object at 1.5 kpc with  $V_{\text{tan}} = 148 \pm 56 \text{ km s}^{-1}$ . Likewise, HDFS 895 displays a proper motion of  $34.9 \pm 8.0 \text{ mas yr}^{-1}$ , and is more likely to be a halo white dwarf at 2.1 kpc with  $V_{\text{tan}} = 346 \pm 79 \text{ km s}^{-1}$ . HDFS 2488 does not display any significant proper motion, and its classification as a point source is questionable, nevertheless, if it is a star, then it would have to be a halo white dwarf at 9 kpc.

### **Mendez & Minniti Faint Blue Objects**

Mendez & Minniti (2000) identified 10 faint blue objects in the HDF South. We classified two of these 10 objects (HDFS 1812 and 1827) as resolved. We measure proper motions of  $2.26 \pm 7.93$  and  $3.25 \pm 6.98 \text{ mas yr}^{-1}$  for these two objects, respectively. One of the faint blue objects (HDFS 1332) is fainter than  $I_{814} = 27$  (therefore not included in our analysis), and has a proper motion of  $9.31 \pm 7.93 \text{ mas yr}^{-1}$ . Six of the faint blue objects (HDFS 1945, 2007, 2178, 441, 1020, 261)

have proper motions in the range 2.56 to 10.27 mas yr<sup>-1</sup>. Our SED fitting analysis showed that HDFS 1945, 2007, and 2178 have colors more consistent with being quasars than stars. In addition, we classify HDFS 441, 1020, and 261 as metal poor stars in the halo of the Galaxy. Therefore, only one of the faint blue objects identified by Mendez & Minniti (2000), HDFS 1444, plus two more white dwarf candidates identified in our analysis (HDFS 895 and 2488) are consistent with being white dwarfs.

We use Reid & Majewski (1993) star count models and our own calculations based on the equations 4.2, 4.3, and 4.4 to predict the number of stars and white dwarfs expected in the HDF South. We expect to find 45–52 stars and 0.66–2.31 white dwarfs, including 0.24–0.50 disk white dwarfs in the HDF South. The star count models mildly over-predict the observed number of stars. The observed population of 2–3 white dwarfs is consistent with the standard Galactic models.

## 4.4 Conclusion

Superb resolution of the HST WFPC2 camera helped us to eliminate almost all of the large number of galaxies present in the HDF North and South. Using accurate SED fitting procedures (to eliminate quasars) and obtaining proper motion measurements (to identify fast moving–halo objects) enabled us to classify the point sources in the HDF.

We identified 4 quasars (consistent with zero proper motion) and 42 stars in the HDF South. Three of these stars (HDFS 1444, 895, and 2488), if on the main sequence, are too distant to be in the Galaxy, and are best explained as white dwarf stars. Their kinematic properties show that HDFS 1444 is probably a thick disk object, whereas the other two are more likely to be in the halo of the Galaxy. Third epoch data on the HDF South would be useful to place better constraints on the proper motions and the kinematic memberships of the point sources.

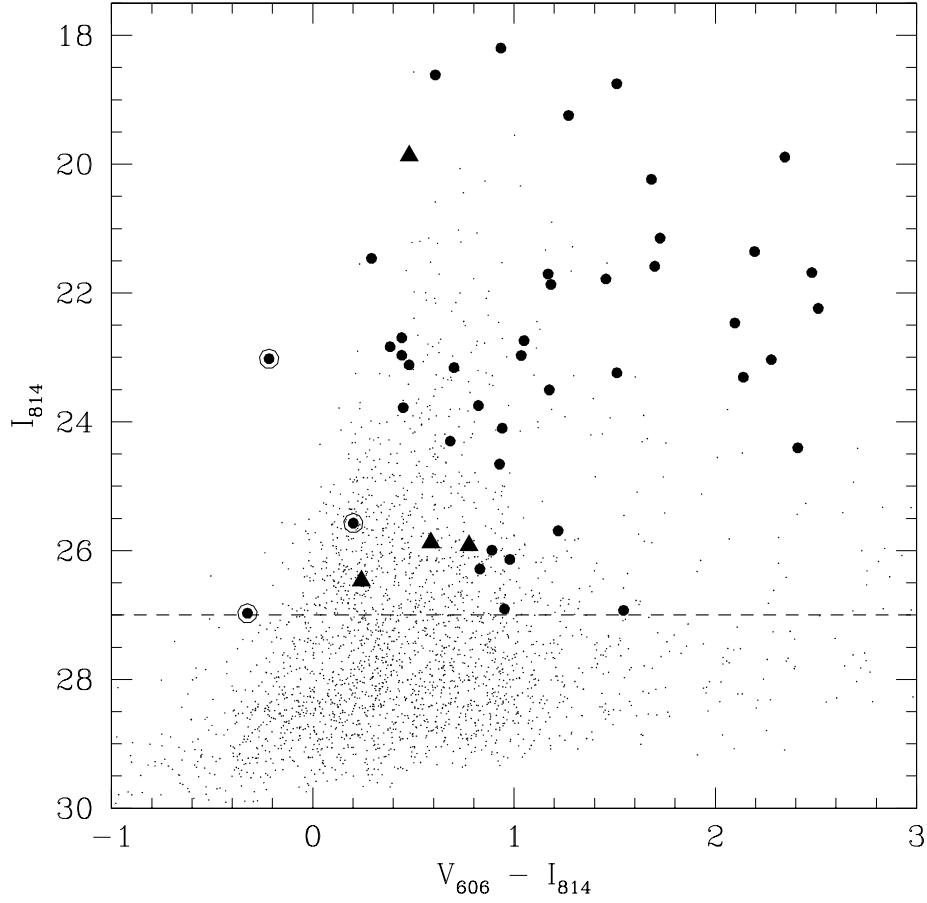


Figure 4.6: The location of the 46 point sources in the HDF South in a color magnitude diagram. Filled circles and triangles represent stars and quasars identified from spectral energy distribution fitting, respectively. White dwarf candidates are marked with open circles, whereas the smaller dots show the rest of the objects in the HDF South catalog. We limited our analysis to the objects brighter than  $I = 27$  (dashed line).

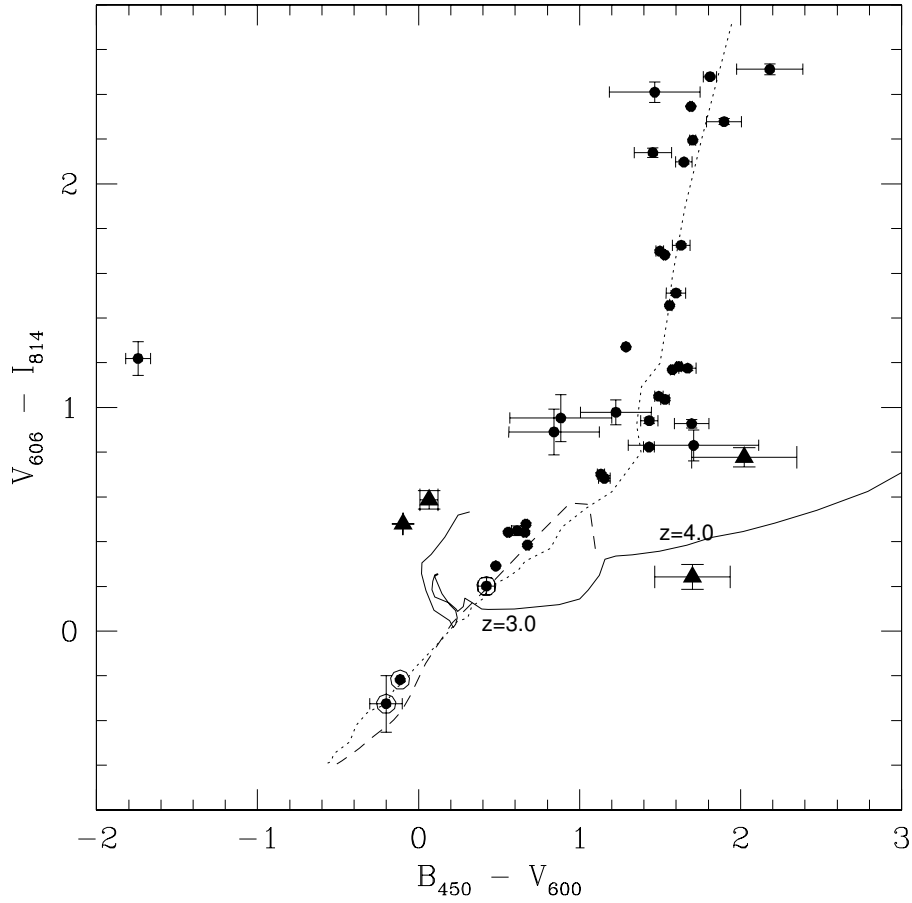


Figure 4.7:  $V_{606} - I_{775}$  vs.  $B_{435} - V_{606}$  color-color diagram for the stars (circles), the quasars (triangles) and the white dwarf candidates (open circles) in the HDF South. Expected tracks for main sequence stars (Pickles 1998; dotted line), pure-H white dwarfs ( $\log g=8$ ,  $T_{\text{eff}} = 60000\text{--}3000\text{K}$ ; dashed line), and quasars (solid line) are also shown. We note that the  $U$  and  $B$  photometry for HDF 2615 is probably wrong ( $B - V = -1.74$ ), as it is barely detected in the  $U$  and  $B$  images, yet its photometry shows excesses in the  $U$  and the  $B$  filters.

Figure 4.6 and 4.7 show the location of the stars, quasars, and white dwarf candidates in the HDF South in color-magnitude and color-color diagrams. A comparison of Figure 4.6 with Figure 3 of Mendez & Minniti (2000) shows that a detailed analysis of the faint blue objects is needed to classify their nature – important additional constraints can be derived from SED fitting and from proper motions, even with a baseline of only 3 years. The number of blue extra-galactic sources is enormous at these magnitudes compared to the number of stellar objects. Our analysis shows that only two of the faint blue objects (HDFS 1444 and 895) show significant proper motion and are consistent with being disk/halo white dwarfs. None of the other faint blue objects exhibit significant proper motion, and therefore they are highly unlikely to be halo white dwarfs. Even if we misclassified a few blue extra-galactic objects as unresolved, this would only decrease the observed number of stars and white dwarfs in the HDF South, and therefore, strengthen our conclusion that the majority of the faint blue objects are not halo white dwarfs.

We found 14 stars including 1 disk white dwarf in the HDF North, and 42 stars including 2 thick disk or halo white dwarf candidates in the HDF South ( $I \leq 27$ ). What can we learn from the HDF-North and South? These two fields are located at different Galactic longitudes and latitudes ( $b = +54.83$  and  $-49.21$ ). A comparison of the observed number of stars with the predicted number of stars from Reid & Majewski star count models and Gilmore et al. (1989) models (14 observed vs. 16-20 predicted for the HDF-North and 42 observed vs. 45-52 predicted for the HDF-South) show that the star count models are consistent with the observed number of stars in these fields.

The observed population of  $\leq 2$  white dwarf candidates ( $I < 27$ ) in each of the HDF North, HDF South, and HUDF (Kilic et al. 2006d) imply that the observed white dwarf population in the HST deep fields do not require any additions to the standard Galactic models. Even if the entire observed white dwarf population in

the HDF and HUDF is part of the dark halo, it would explain  $\leq 10\%$  of the dark matter in the Galaxy (Pirzkal et al. 2005). The faint blue objects, especially the non-observed population of halo white dwarfs, are highly unlikely to solve the dark matter problem.

# Chapter 5

## Debris Disks Around White Dwarfs

*“The true harvest of my life is intangible - a little star dust caught, a portion of the rainbow I have clutched.”*

*– Henry David Thoreau*

### 5.1 Introduction

The presence of planets around solar type stars suggests that some white dwarfs should have planetary systems as well. Even though planets within 5 AU of their parent stars will most likely not survive the red giant phases, much of the outer planets, Kuiper belt objects, and Oort-like comet clouds are predicted to survive around white dwarf stars (Debes & Sigurdsson 2002). Near and mid-infrared searches for stellar and substellar companions to white dwarfs have resulted in the discovery of late type dwarfs, including two brown dwarfs (Becklin & Zuckerman 1988; Farihi et al. 2005), but no planetary systems yet (Mullally et al. 2006). The search for the

effects of reflex orbital motion in changing light travel times caused by possible planetary companions to pulsating white dwarfs (Winget et al. 2003) has provided strong limits on one object so far, G117-B15A (Kepler et al. 2005). Finding a Jupiter-size planet around an Earth-size white dwarf would herald a new age of direct studies of extra solar planets (by enabling us to image the planetary companions).

An easier way to detect the signatures of planetary systems around white dwarfs is via debris disks. Previously stable orbits of planets around a star undergoing mass loss may become unstable, which in some systems may result in close encounters leading to tidal stripping of a parent body, thus producing a circumstellar debris disk (Debes & Sigurdsson 2002; Jura 2003). Until recently, there was only a single white dwarf known to have a circumstellar debris disk, G29-38 (Zuckerman & Becklin 1987; Chary et al. 1999). G29-38 is a pulsating DAZ white dwarf with a hydrogen rich atmosphere that has trace amounts of metals. Infrared excess around this white dwarf was initially thought to be due to a brown dwarf companion (Zuckerman & Becklin 1987), however, follow-up observations in the near- and mid-infrared showed that the excess emission is caused by a debris disk. Reach et al. (2005b) discovered silicate emission around G29-38 and could explain the observed mid-infrared spectrum by a combination of amorphous olivine, amorphous carbon, and crystalline forsterite. These observations suggest a relatively recent disruption of one or perhaps a few comets or asteroids around this white dwarf.

The presence of metals in the photosphere of G29-38 (Koester et al. 1997) is probably related to the presence of a dust disk around the star. Possible scenarios for the explanation of the metal abundances in DAZ white dwarfs include accretion from the interstellar medium (ISM; Dupuis et al. 1992), cometary impacts (Alcock et al. 1986), and accretion of asteroidal material from a surrounding debris disk (Graham et al. 1990). If accretion from the ISM is responsible for the observed metal abundances, we would expect to find cool DAZs only near interstellar clouds since

the diffusion timescales for the metals in their photospheres ( $\sim$ years) are shorter than the cloud crossing timescales ( $\geq 10^4$  years). Yet Zuckerman et al. (2003) did not find any correlation between the locations and relatively large numbers of DAZs with the locations and amount of ISM present within the local bubble.

Gianninas et al. (2004) reported the discovery of the most massive ( $1.24M_{\odot}$ ) and metal-rich DAZ white dwarf ever found; GD362. In addition to Balmer lines, they detected Ca I, Ca II, Mg I, and Fe I lines in the optical spectra of this star with estimated  $T_{\text{eff}} = 9740$  K and  $\log g = 9.1$ . They measured a calcium abundance of  $[\text{Ca}/\text{H}]^1 = -5.2$ , about a thousand times higher than the DAZ stars with similar effective temperatures in the Zuckerman et al. (2003) sample. Calcium abundances for known DAZs (Zuckerman et al. 2003; Gianninas et al. 2004; Berger et al. 2005) range from  $[\text{Ca}/\text{H}] = -5.2$  to  $-12.7$ . With several stars being more metal rich than G29-38 ( $[\text{Ca}/\text{H}] = -6.9$ ), they provide a unique opportunity to test if the observed metal abundances can be explained with debris disks similar to that around G29-38. With a goal of determining the fraction of DAZs with detectable infrared excess emission from warm debris disks, we obtained near-infrared spectroscopy of 20 DAZ white dwarfs including G29-38 and GD362.

## 5.2 Observations

### 5.2.1 Photometry

All of the DAZ white dwarfs identified by Zuckerman et al. (2003) and Koester et al. (2005) are bright enough to be detected in the Two Micron All Sky Survey (2MASS). However, the 2MASS photometry in the  $H$  and  $K$  bands is unreliable for the majority of the objects, making the search for infrared excess around these objects impossible. Figure 5.1 presents 2MASS photometry versus effective tem-

---

<sup>1</sup> $[\text{Ca}/\text{H}]$  is the logarithm of the Ca/H abundance ratio by numbers.

perature for single DAZ white dwarfs studied by Berger et al. (2005), along with the predicted sequences for DA (solid line) and DB white dwarfs (dashed line) from Bergeron et al. (1995). The 2MASS photometry for G29-38 and the 3m NASA Infrared Telescope Facility (IRTF) photometry for GD362 (filled triangles) are also plotted. Several objects are only detected in the  $J$  and  $H$  bands, but not in the  $K$  band, and are therefore not included in the bottom panel. Even though the large error bars in 2MASS photometry prevent any definitive conclusion, it is clear from this figure that several objects, most notably GD56, show excess  $K$  band flux at the  $2 - 3\sigma$  level.

### 5.2.2 Spectroscopy

We used the 0.8–5.4 Micron Medium-Resolution Spectrograph and Imager (SpeX; Rayner et al. 2003) on the IRTF and 0.5'' slit to obtain a resolving power of 90–210 (average resolution of 150) over the 0.8–2.5  $\mu\text{m}$  range. Our observations were performed under conditions of thin cirrus and partly cloudy skies between November 2 – 7, 2005. To remove the dark current and the sky signal from the data, the observations were taken in two different positions on the slit (A and B) separated by 10''. The total exposure times for individual objects ranged from 16 minutes to 96 minutes. Internal calibration lamps (a 0.1W incandescent lamp and an Argon lamp) were used for flat-fielding and wavelength calibration, respectively. In order to correct for telluric features and flux calibrate the spectra, nearby bright A0V stars were observed at an airmass similar to the target star observations. We used an IDL-based package, Spextool version 3.2 (Cushing et al. 2004), to reduce our data (see Kilic et al. 2005a for details). Using the nearby A0V star observations and the XTELLCOR package (Vacca et al. 2003), we created a telluric spectrum for each A0V star observation, and used these spectra to flux calibrate and correct the telluric features in the white dwarf spectra.

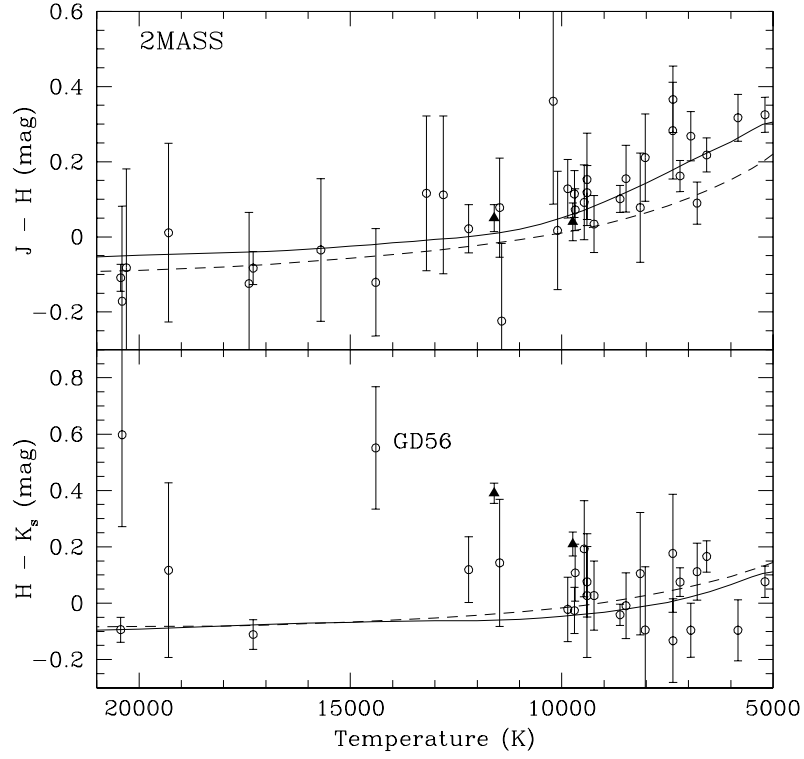


Figure 5.1:  $J - H$  and  $H - K_S$  (from 2MASS) vs.  $T_{\text{eff}}$  diagrams for single DAZ white dwarfs studied by Berger et al. (2005; open circles). The predicted sequences for DA (solid line) and DB (dashed line) white dwarfs and the colors for G29-38 and GD362 (filled triangles) are also shown. GD56, a likely debris disk candidate from 2MASS photometry, is labeled.

### 5.3 Results

Figure 5.2 presents the flux calibrated spectra of our sample stars (black lines; ordered in  $T_{\text{eff}}$ ) and their respective DA white dwarf model atmospheres (red lines; kindly made available to us by D. Koester and D. Saumon). The resolution of the model white dwarf spectra was not matched to the instrumental resolution in order to show the predicted locations of the Paschen lines (0.955, 1.005, 1.094, 1.282, and  $1.876\mu\text{m}$ ). Changing the resolution of these models would only make the hydrogen lines shallower but not change the overall shape of the continuum. The observed white dwarf spectra are affected by strong telluric features between  $1.35 - 1.45\mu\text{m}$ ,  $1.80 - 2.05\mu\text{m}$ , and longward of  $2.5\mu\text{m}$  (a typical telluric spectrum observed at the IRTF is presented in Figure 3 of Kilic et al. 2005a). Therefore, weak features observed in several stars in these wavelength ranges are likely to be due to telluric correction problems.

We derived synthetic colors of all 20 objects in our sample using our infrared spectra. Since our observations were performed under non-photometric conditions, the absolute flux level in these spectra cannot be trusted. Nevertheless, the relative flux level of the spectra,  $J - H$  and  $H - K$  colors should not be as sensitive to non-photometric conditions. The photometric error bars were calculated from the observed scatter of the spectra in individual frames. Effective temperatures, gravities, calcium abundances, 2MASS photometry, and our synthetic colors for these objects are presented in Table 5.1. A comparison of the 2MASS colors with our synthetic colors shows that they are consistent within the errors. Figure 5.3 presents synthetic colors versus temperatures, and  $J - H$  versus  $H - K$  color for our sample. Model sequences for pure H (solid line) and pure He atmosphere white dwarfs (dashed line) from Bergeron et al. (1995) are also shown. Our IRTF observations improved the photometry for these objects significantly compared to 2MASS photometry, enabling us to use the spectroscopy and photometry to identify near-

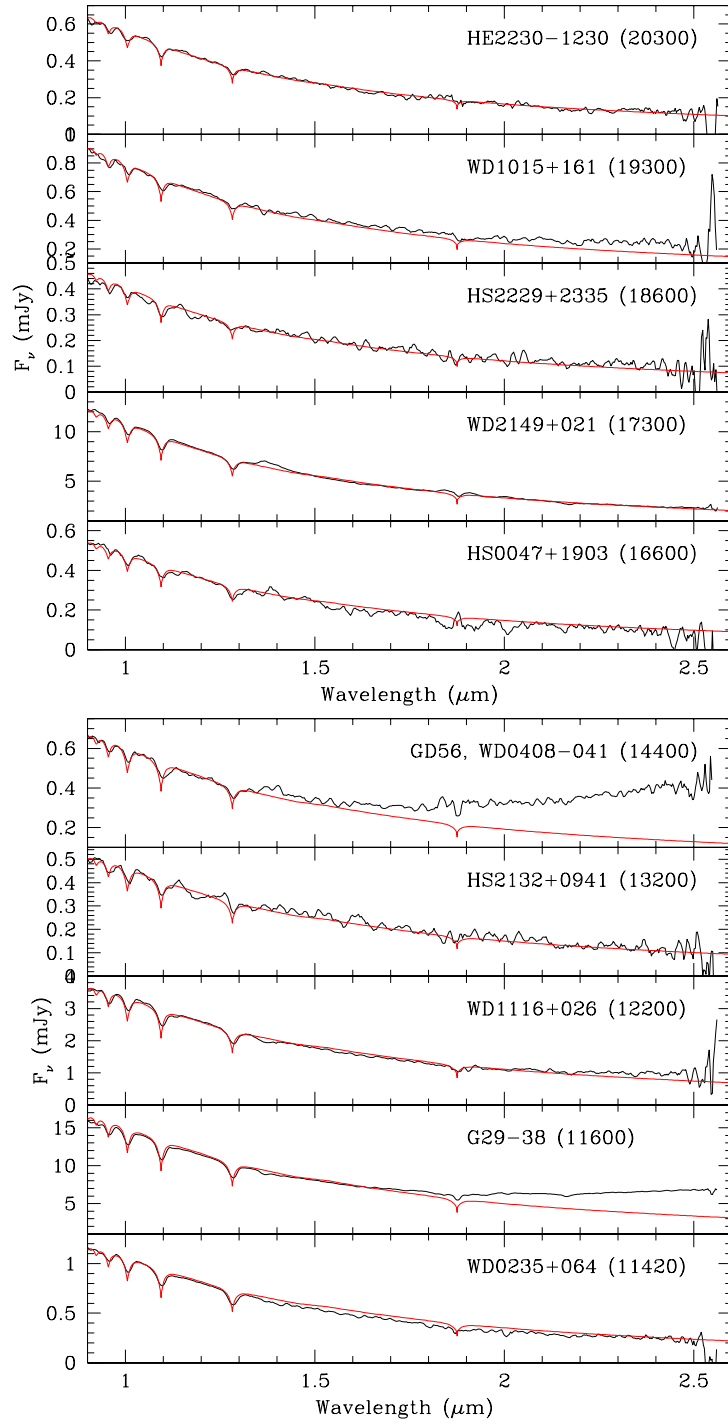


Figure 5.2: Flux calibrated spectra of the DAZ white dwarfs (black lines; ordered in  $T_{\text{eff}}$ ) observed at the IRTF compared to the white dwarf models (red lines).

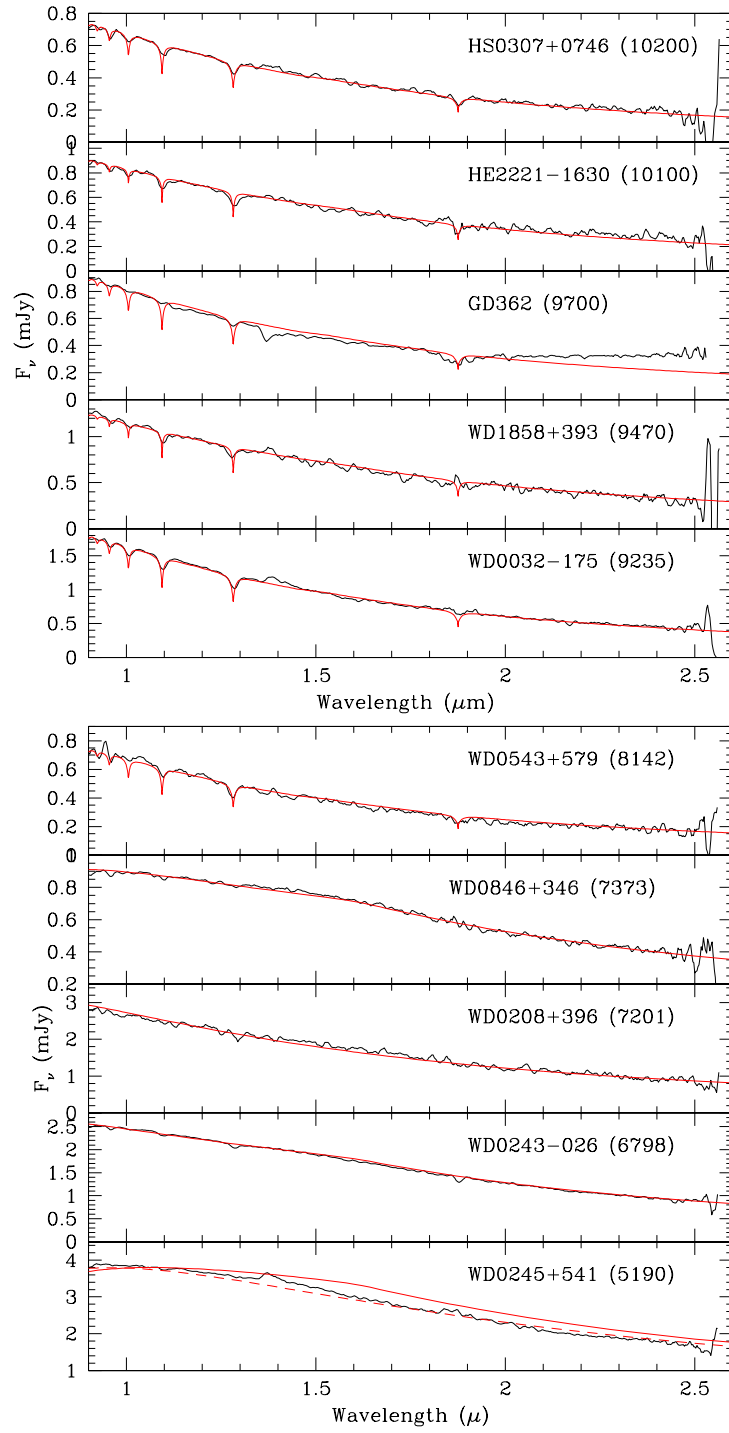


Figure 5.2: Continued

infrared excess.

A comparison of the spectroscopy and photometry for the DAZ white dwarfs in our sample shows that the majority of the stars do not show any excess emission in the near-infrared. However, the previously known debris disk white dwarf (G29-38) plus GD362 and WD0408-041 (hereafter GD56) show significant excesses in the  $K$ -band. The flux from GD362 is consistent with a typical 9000 K white dwarf in the  $J$  and  $H$  bands, but is significantly higher than the expected flux level from a white dwarf in the  $K$ -band. The upper limits on the  $H$  and  $K$  band photometry from the 2MASS are also consistent with the excess  $K$ -band emission seen in the IRTF spectrum of GD362. The amount of excess  $K$  band flux is comparable to the amount of excess light seen from G29-38. The observed spectrum of GD56 is consistent with a typical 14000 K white dwarf in the  $J$  band, but it starts to deviate from a DA white dwarf model in the  $H$  band, and shows more infrared excess than either of G29-38 and GD362. GD56, G29-38, and GD362 are easily distinguishable from the rest of the DAZs in our sample in Figure 5.3.

There are two other objects with possible slight infrared excesses, WD1015+161 and WD1116+026. WD1015+161 observations may have been affected by a nearby object, which is located  $2.1''$  away and  $\sim 0.2$  mag fainter than the white dwarf at  $J$ . We obtained a noisy spectrum of this object that did not reveal any spectral features. The overall flux distribution of this nearby object could be approximated by an  $\sim 8000$  K blackbody. Hence the observed slight excess for WD1015+161 ( $T_{\text{eff}} = 19300\text{K}$ ) in the  $K$  band may be caused by this nearby object. WD1116+026 may show slight excess in the  $K$  band as well, though our synthetic photometry shows that the excess in  $H - K$  color is less than  $2\sigma$ . This white dwarf appeared to be a single star in our guider and spectral images. Therefore, WD1116+026 ( $[\text{Ca}/\text{H}] = -7.3$ ) may be another warm debris disk case, but the observed excess and errors are consistent with photospheric flux from the white dwarf.

Table 5.1: Near-Infrared Photometry of Cool DAZs

Object	$T_{\text{eff}}(\text{K})$	$\log g$	[Ca/H]	$J_{2MASS}$	$J - H_{2MASS}$	$H - K_{2MASS}$	$J - H_{IRTF}$	$H - K_{IRTF}$
WD0032-175	9235	8.0	-10.2	$14.79 \pm 0.04$	$0.03 \pm 0.08$	$0.03 \pm 0.12$	$0.04 \pm 0.04$	$-0.02 \pm 0.04$
HS0047+1903	16600	7.8	-6.1	$16.33 \pm 0.11$	...	...	$-0.10 \pm 0.09$	$-0.10 \pm 0.15$
WD0208+396	7201	7.9	-8.8	$13.83 \pm 0.02$	$0.16 \pm 0.04$	$0.08 \pm 0.05$	$0.17 \pm 0.03$	$0.01 \pm 0.03$
WD0235+064	11420	7.9	-9.0	$15.69 \pm 0.07$	$-0.22 \pm 0.21$	...	$-0.05 \pm 0.04$	$-0.04 \pm 0.08$
WD0243-026	6798	8.2	-9.9	$14.68 \pm 0.04$	$0.09 \pm 0.06$	$0.11 \pm 0.10$	$0.21 \pm 0.03$	$0.01 \pm 0.04$
WD0245+541	5190	8.2	-12.7	$13.87 \pm 0.02$	$0.33 \pm 0.05$	$0.08 \pm 0.06$	$0.25 \pm 0.03$	$0.07 \pm 0.04$
HS0307+0746	10200	8.1	-7.6	$16.39 \pm 0.14$	$0.36 \pm 0.27$	...	$0.08 \pm 0.02$	$-0.02 \pm 0.02$
WD0408-041	14400	7.8	-7.1	$15.87 \pm 0.06$	$-0.12 \pm 0.14$	$0.55 \pm 0.22$	$0.16 \pm 0.04$	$0.56 \pm 0.04$
G29-38	11600	8.1	-6.9	$13.13 \pm 0.03$	$0.06 \pm 0.04$	$0.39 \pm 0.04$	...	...
GD362	9740	9.1	-5.2	$16.16 \pm 0.09$	...	...	$0.04 \pm 0.05$	$0.21 \pm 0.04$
WD0543+579	8142	8.0	-10.3	$15.52 \pm 0.07$	$0.08 \pm 0.15$	$0.11 \pm 0.22$	$0.02 \pm 0.08$	$-0.05 \pm 0.12$
WD0846+346	7373	8.0	-9.4	$15.89 \pm 0.07$	$0.28 \pm 0.13$	$0.18 \pm 0.21$	$0.31 \pm 0.04$	$0.03 \pm 0.04$
WD1015+161	19300	7.9	-6.3	$16.13 \pm 0.09$	$0.01 \pm 0.24$	$0.12 \pm 0.31$	$0.02 \pm 0.03$	$0.08 \pm 0.03$
WD1116+026	12200	7.9	-7.3	$14.75 \pm 0.04$	$0.02 \pm 0.06$	$0.12 \pm 0.12$	$-0.02 \pm 0.05$	$0.06 \pm 0.07$
WD1858+393	9470	8.0	-7.8	$15.53 \pm 0.05$	$0.09 \pm 0.10$	$0.19 \pm 0.17$	$0.09 \pm 0.03$	$-0.03 \pm 0.05$
HS2132+0941	13200	7.7	-7.7	$16.09 \pm 0.08$	$0.12 \pm 0.21$	...	$0.05 \pm 0.06$	$-0.05 \pm 0.09$
WD2149+021	17300	7.9	-7.6	$13.20 \pm 0.02$	$-0.08 \pm 0.04$	$-0.11 \pm 0.05$	$-0.05 \pm 0.03$	$-0.06 \pm 0.03$
HE2221-1630	10100	8.2	-7.6	$15.80 \pm 0.06$	$0.02 \pm 0.16$	$-0.06 \pm 0.14$	$0.10 \pm 0.05$	$0.07 \pm 0.04$
HS2229+2335	18600	7.9	-6.3	$16.16 \pm 0.09$	...	...	$0.02 \pm 0.07$	$0.00 \pm 0.08$
HE2230-1230	20300	7.7	-6.3	$16.36 \pm 0.11$	$-0.08 \pm 0.26$	...	$-0.09 \pm 0.08$	$-0.07 \pm 0.12$

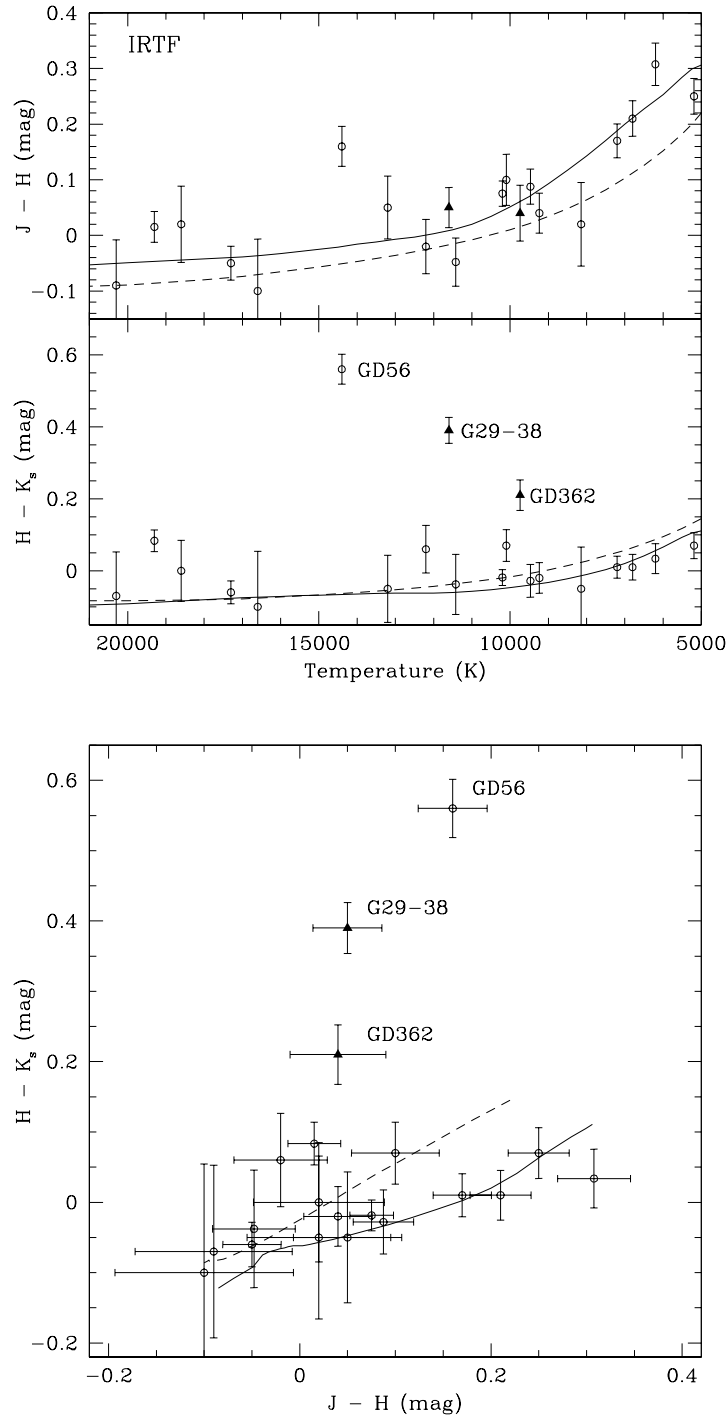


Figure 5.3:  $J - H$  and  $H - K$  vs. temperature and  $J - H$  vs.  $H - K$  color-color diagrams for the DAZ white dwarfs that we observed. Model sequences for pure H (solid line) and pure He (dashed line) atmosphere white dwarfs are also shown. The previously known white dwarf with circumstellar debris disk (G29-38) and the newly discovered white dwarfs with significant infrared excesses (GD56 and GD362) are labeled.

We note that the observed spectrum of WD0245+541 is better fitted with a 5190 K pure He white dwarf model atmosphere (dashed line in the last panel in Figure 5.2) rather than a pure H model atmosphere (solid line in the same panel). Only weak H $\alpha$  is seen in the spectrum of cool DAs with  $T_{\text{eff}} \sim 5000$  K, and infrared photometry is often necessary to determine the atmospheric composition of cool white dwarfs (see Bergeron et al. 2001 for a detailed discussion). Greenstein & Liebert (1990) obtained an H $\alpha$  equivalent width measurement of  $0.3\text{\AA}$  for WD0245+541. Their classification of this star as a DA white dwarf relies only on optical spectroscopy. Our near-infrared spectrum of this object favors a helium rich atmosphere model, therefore WD0245+541 is more likely to be a DZA instead of a DAZ.

## 5.4 Discussion

### 5.4.1 GD362

Tokunaga, Becklin, & Zuckerman (1990) presented the K-band spectrum of G29-38 in their Figure 2. Their spectrum shows a constant flux level at 6 mJy with 0.5 mJy scatter. Our IRTF spectrum of GD362 shows a constant  $K$ -band flux level at  $\sim 0.33$  mJy with little scatter. Our spectroscopic observations and the 2MASS photometry show that GD362 has a  $K$ -band excess similar to G29-38. Can this be another white dwarf with a surrounding debris disk?

Gianninas et al. (2004) derived an absolute  $V$  magnitude of 14.31 and a distance of  $\sim 24$  pc for GD362. Using these values, we derive an apparent  $V$  magnitude of 16.21; slightly fainter than the less accurate photographic magnitude of  $V = 16.0$  (Greenstein 1980). The full width at half maximum of the spatial profiles in our spectral images is about  $1''$ , which corresponds to 24 AU at 24 pc. The source of the infrared excess is within 24 AU of the star. Figure 5.4 shows the observed GD362 spectrum compared to a 9740 K blackbody (dashed line, bottom panel) nor-

malized to  $V=16.21$ . The blackbody fits the observed spectrum well in the  $J$  and  $H$  bands; the distance estimate is correct. The difference between the observed and the expected flux from the star is about 0.05 mJy in the  $K$  band. At 24 pc, this corresponds to  $M_K \sim 15.8$ , a late type T dwarf (Leggett et al. 2002). We used a T5 dwarf template from the IRTF Spectral Library (Cushing et al. 2005) plus the normalized 9740 K blackbody to attempt to match the observed excess in the  $K$  band (green line). T dwarfs suffer from broad water absorption bands (stronger for later spectral types) centered at 1.4, 1.9, and  $2.7\mu\text{m}$ . Adding a T5 dwarf to a 9740 K blackbody creates spectral features from 1.3 to  $2.5\mu\text{m}$  that are prominent, yet not seen in GD362’s spectrum. Therefore, neither T dwarfs nor any other dwarf stars can explain the excess seen between 2.0 and  $2.5\mu\text{m}$ . We also tried to match the observed spectrum with a combination of different blackbodies. The excess emission is best fit with a 700 K blackbody (red line). Therefore, the best explanation for the K-band excess in GD362 is a circumstellar dust disk heated by the white dwarf. It took 17 years to find the second white dwarf with a brown dwarf companion (Farihi & Christopher 2004). Likewise, our discovery of a debris disk around GD362 came 18 years after the first discovery of a debris disk around G29-38 (Zuckerman & Becklin 1987).

#### 5.4.2 GD56

The observed excess in GD56 is stronger than the excess seen in G29-38 and GD362. The expected flux levels from a 14400 K blackbody (normalized to the observed GD56 spectrum in the  $J$ -band) in the  $H$  and  $K_S$  bands are 0.27 and 0.17 mJy, respectively. The difference between the observed and expected flux from the star is about 0.05 mJy in the  $H$  band, and 0.18 mJy in the  $K$  band. Using  $\log g = 7.8$  and  $T_{\text{eff}} = 14400$  K (Berger et al. 2005) and Bergeron et al. (1995) models, we estimate the absolute  $K$ -band magnitude of GD56 to be 11.43 mag. If the observed

near-infrared excess is due to a late type dwarf companion, this would correspond to  $M_K \sim 11.38$  mag, an early L dwarf (Leggett et al. 2002). We used a L3 dwarf template from the IRTF Spectral Library (Cushing et al. 2005) plus the normalized 14400 K blackbody to attempt to match the observed excess in the  $K$  band (green line, top panel). Adding an L3 dwarf to a 14400 K blackbody creates spectral features from 1.3 to 2.5  $\mu\text{m}$  that are prominent, yet not seen in the spectrum of GD56, and hence a cool dwarf companion cannot explain the excess seen between 1.5 – 2.5  $\mu\text{m}$ . We can fit the observed  $K$  band excess around GD362 with a 700 K blackbody. Likewise, Reach et al. (2005b) found a best-fit blackbody temperature of 890 K for the debris disk around G29-38. The top panel in Figure 5.4 shows that the excess around GD56 can be explained with an  $\sim 890$  K blackbody as well. Therefore, the best explanation for the  $H$  and  $K$  band excess in GD56 is a circumstellar dust disk heated by the white dwarf.

GD56 was included in Farihi et al.’s (2005) search for substellar companions around white dwarfs. They obtained  $K$ -band photometry for  $\sim 1/3$  of their sample and used 2MASS photometry for the rest of the objects. Due to low signal-to-noise 2MASS  $K$ -band photometry, they did not report a near-infrared excess around GD56 (J. Farihi 2006, private communication). Their search for companions around 371 white dwarfs resulted in the discovery of late type stars and a brown dwarf, but no debris disks. Our IRTF search for near-infrared excess around cool DAZs has revealed two new debris disks. Our sample was restricted to 20 stars (50% of all known single DAZs) due to the positional constraints imposed by the time of the observations and the declination limit of the telescope. We observed all known DAZs with  $0 < \alpha < 11$  and  $19 < \alpha < 24$  hours and  $\delta > -17^\circ$ .

A *Spitzer/IRAC* search for mid-infrared excess around 4 DAZs by von Hippel et al. (2006), 4 more DAZs by Debes et al. (2006, private communication), and an additional 17 DAZs by Farihi et al. (2006, private communication) resulted

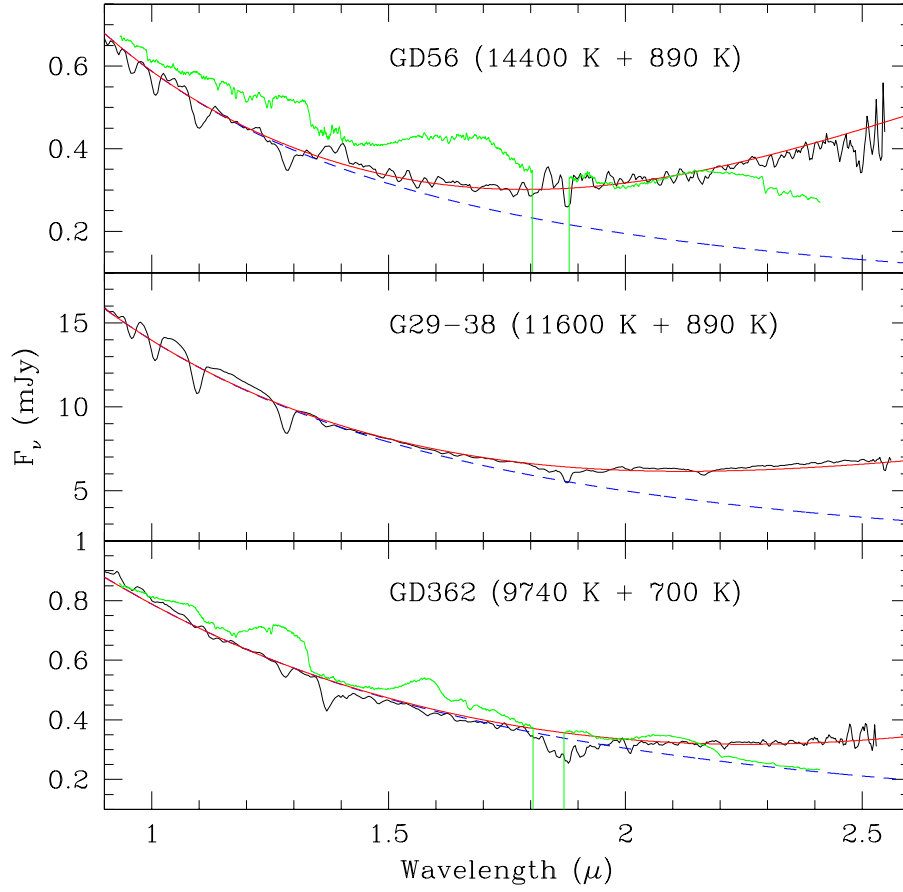


Figure 5.4: The IRTF spectra of the white dwarfs with circumstellar debris disks (black lines). The expected infrared fluxes from each star (blue dashed line) and composite blackbody + blackbody templates (red line) are shown in each panel. The top and bottom panels also show composite blackbody + brown dwarf templates for GD56 and GD362 (green lines).

in the discovery of two more debris disks around cool DAZs ( $T_{\text{eff}} < 10000$  K), increasing the number of debris disks around DAZ white dwarfs to 5. There is some overlap between our IRTF program and the Spitzer programs; the total number of DAZs observed so far in near- or mid-infrared is 35. Based on these observations, the fraction of cool DAZs with detectable debris disks is 14% (5 out of 35 stars). Only 3 of the debris disks are warm enough to be detected in the  $K$ -band, and hence the fraction of  $K$ -band detectable debris disks is  $\sim 9\%$ . These discoveries suggest a growing connection between cool DAZ white dwarfs and circumstellar debris disks.

### 5.4.3 Possible Trends

Figure 5.5 shows the calcium abundances in cool DAZ white dwarfs as a function of effective temperature from Berger et al. (2005). Objects with IRTF near-infrared spectroscopy (filled circles), and Spitzer 4.5 and  $8\mu\text{m}$  photometry (filled triangles; von Hippel et al. 2006) are also shown. The rest of the objects from the Berger et al. (2005) sample are shown as stars. Objects with circumstellar debris disks are marked with open circles.

None of the six objects with  $T_{\text{eff}} > 16000$  K that were observed at the IRTF and with Spitzer/IRAC show any excess emission from warm debris disks. Even though we cannot rule out the existence of cool debris disks around these objects, their high metal abundances require continuous, fairly high accretion rates from surrounding media (Koester et al. 2005). The diffusion timescales in a typical DAZ with  $0.6M_{\odot}$  and  $T_{\text{eff}} \geq 15000$  K are shorter than  $\sim 3$  days (Paquette et al. 1986). Photospheric metals in these stars have to be replenished on a daily basis. If the metals were accreted from circumstellar debris disks, we should have been able to detect such disks around these objects. Five of these warm DAZs are in fact more metal rich than GD56 and G29-38. Unless all 6 objects have optically thin, smaller, or edge on disks, their metal abundances may require another explanation.

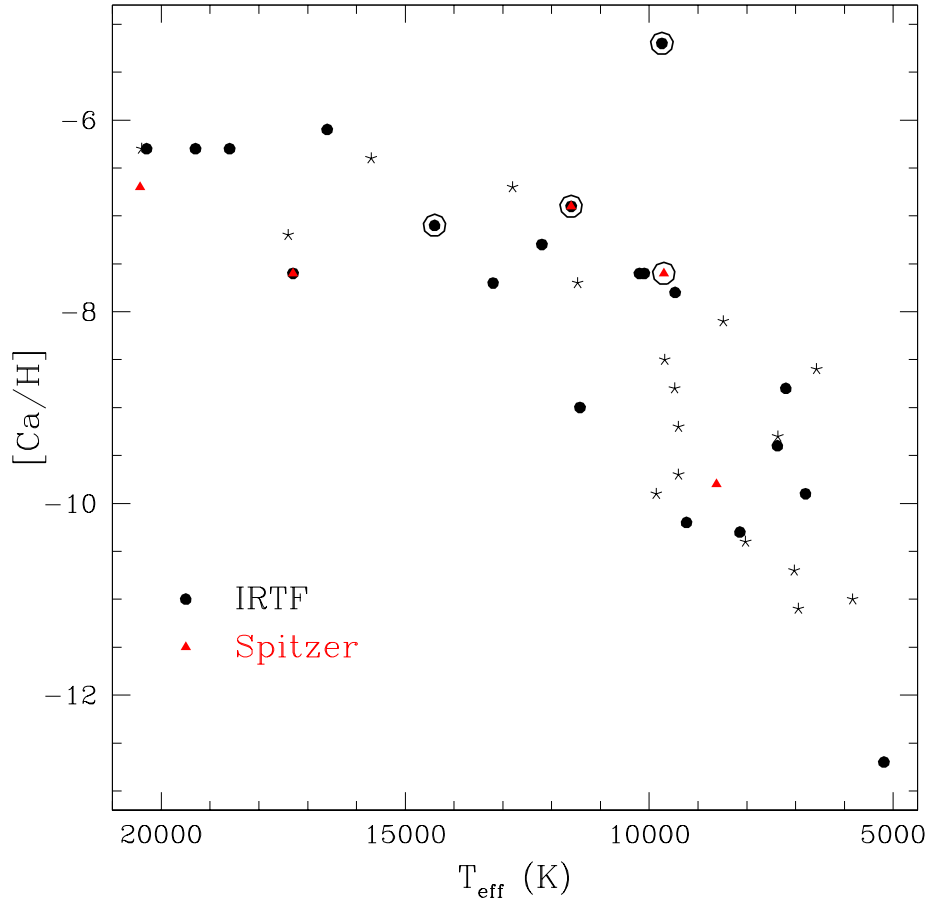


Figure 5.5: Ca abundances  $[\text{Ca}/\text{H}]$  and effective temperatures for the objects observed at the IRTF (filled circles) and Spitzer (filled triangles; from Reach et al. 2005b and von Hippel et al. 2006). The rest of the DAZs from Berger et al. (2005) are shown with star symbols. White dwarfs with circumstellar debris disks are marked with open circles.

Radiative levitation can explain the observed metal abundances in hotter white dwarfs, though it is predicted to be insignificant below 20000 K.

All three observed white dwarfs with  $T_{\text{eff}} \sim 10000 - 15000$  K and  $[\text{Ca}/\text{H}] \geq -7.1$  have debris disks around them. In addition, WD1116+026 ( $T_{\text{eff}} = 12200$  K and  $[\text{Ca}/\text{H}] = -7.3$ ) has a slight (questionable) K-band excess that can be explained by a cooler, or more distant debris disk. Its calcium abundance is 2.5 times lower than that of G29-38, therefore unlike the warm DAZ stars mentioned above, a cooler/distant debris disk can actually explain the lower metal abundance for WD1116+026. There is only one more white dwarf satisfying the above  $T_{\text{eff}}$  and  $[\text{Ca}/\text{H}]$  criteria in Berger et al. (2005) sample. WD1150-153 ( $T_{\text{eff}} = 12800$  K and  $[\text{Ca}/\text{H}] = -6.7$ ) has more calcium than GD56 and G29-38, and therefore, it is likely to have a debris disk around it. HE0106-3253 ( $T_{\text{eff}} = 15700$  K and  $[\text{Ca}/\text{H}] = -6.4$ ) has surface temperature and calcium abundance similar to warm DAZ white dwarfs without detectable debris disks. However, spectroscopic or photometric observations of both of these objects are required to search for excess flux in the infrared.

We did not detect any near-infrared excesses from debris disks in our  $K$  band observations of DAZs with  $T_{\text{eff}} < 14000$  K and  $[\text{Ca}/\text{H}] < -7.5$ . Using Spitzer/IRAC observations, von Hippel et al. (2006) found excess 4.5 and  $8\mu\text{m}$  emission around a white dwarf with  $T_{\text{eff}} = 9700$  K and  $[\text{Ca}/\text{H}] = -7.6$ . This object (WD2115-560) is included in Figure 5.1 and has  $J - H = 0.11 \pm 0.06$  mag and  $H - K = -0.03 \pm 0.08$  mag as measured by 2MASS. Its 2MASS colors are consistent with the predicted colors for a 9700 K white dwarf. Von Hippel et al. (2006) also observed a cooler DAZ white dwarf with  $T_{\text{eff}} = 8619$  K and a calcium abundance two orders of magnitude smaller than WD2115-560 and did not find any excess up to  $8\mu\text{m}$ . The lack of infrared excess around this object does not necessarily mean that it does not have a debris disk, as it may have a colder, more distant debris disk that would explain the lower calcium abundance and would show up at longer wavelengths. Four out of

10 DAZs with  $T_{\text{eff}} = 9000 - 15000$  K and  $[\text{Ca}/\text{H}] > -8$  have debris disks detectable with the current precision of our observations.

#### 5.4.4 Properties of White Dwarf Debris Disks

The similarity of the near-IR excess around the known debris disks white dwarfs suggests that the well studied white dwarf, G29-38, is a good template for understanding debris disk phenomenon. Jura (2003) suggested that the infrared excess around G29-38 can be explained by emission from an optically thick disk with an inner radius of  $0.14 R_{\odot}$  and an outer radius of less than  $1 R_{\odot}$ . This ring of dust would lie within the Roche region of the white dwarf where an asteroid could have been destroyed to produce a system similar to Saturn’s rings.

Reach et al. (2005b) obtained *Spitzer* photometry and spectroscopy of G29-38 which revealed a continuum peak around  $4.5\mu\text{m}$  and a  $9\text{--}11 \mu\text{m}$  emission feature. Fitting an optically thin dust cloud model to these observations, they showed that a model consisting of two blackbodies with temperatures of 890 K and 290 K would explain the observed IR continuum, and a mixture of amorphous olivine and forsterite in an emitting region  $1 - 5 R_{\odot}$  from the star can reproduce the  $9\text{--}11 \mu\text{m}$  feature. If the dust cloud is optically thin, this distance would be unexpected since the Poynting-Robertson timescale for particles to spiral onto the white dwarf from a distance of  $1 R_{\odot}$  is on the order of years (G29-38 is known to have IR excess since 1987). Therefore, an optically thick dust cloud/disk seems more reasonable (von Hippel et al. 2006).

If we assume that the disks are analogs of planetary rings, optically thick but physically thin disks of rocks and dust, they would have lifetimes set by the viscous spreading time of the rings. Assuming a similar viscosity for the white dwarf debris disks and Saturn’s rings, hence assuming a similar optical depth and particle size distribution, von Hippel et al. (2006) estimated that the white dwarf ring lifetimes

are  $\sim 100$  times longer than the lifetime of Saturn’s rings because of their larger radii. This lifetime is easily  $\geq 10^9$  years, comparable to the median post-main sequence lifetime of the known debris disk white dwarfs. This scenario provides a disk lifetime consistent with the ages of the debris disk white dwarfs.

## 5.5 Conclusions

Our near-infrared spectroscopic observations of 20 cool DAZs resulted in the discovery of two more white dwarfs with circumstellar debris disks. The observed near-IR excesses around GD56 and GD362 are similar to the infrared excess seen around the previously known DAZ with a circumstellar debris disk (G29-38). Due to its  $T_{\text{eff}}$  and calcium abundance (i.e. its position in Figure 5), we postulate that another DAZ white dwarf, WD1150-153, is likely to have a  $K$ -band detectable circumstellar debris disk.

If the debris disks around white dwarfs are similar to planetary rings, the disk lifetimes would be consistent with the ages of the white dwarfs, and the debris disks would not require continual replenishment from a longer-lived source of small bodies. However, if the lifetime of the debris disks is short, it would suggest that the hot dust comes from populations of colder, longer-lived reservoirs of comets or other debris that are more massive than the hot dust clouds.

Debris disks around main sequence stars often have excesses at  $24\mu\text{m}$ , but hardly ever at  $8\mu\text{m}$  (e.g. Chen et al. 2005). DAZ white dwarfs may well behave the same way. The cool reservoir model (a cloud of dust at  $\sim 120$  K) may be an example of the kind of dust cloud that the recent IRAC surveys could not detect around cool DAZs, but a sensitive longer wavelength survey could. The fraction of known single DAZs with near- or mid-infrared (up to  $8\mu\text{m}$ ) excesses is 14%. Mid-infrared photometry of more DAZs at longer wavelengths will likely bring this fraction up. Accretion from these debris disks would also explain the photospheric

metal abundances observed in DAZ white dwarfs.

Our understanding of debris disks around white dwarfs will benefit greatly from mid-infrared spectroscopy. *Spitzer* spectroscopy of G29-38 revealed a silicate feature around this object suggesting a cometary or asteroidal origin for the debris disk (Reach et al. 2005b). Mid-infrared spectroscopy of GD56 and GD362 along with the other debris disk white dwarfs will be needed to check if all of them show silicate emission at 10  $\mu\text{m}$ . These observations will help our understanding of the formation and evolution of debris disks around white dwarfs.

## Chapter 6

# Conclusions and Future Work

*“Obstacles cannot crush me. Every obstacle yields to stern resolve. He who is fixed to a star does not change his mind.”*

*– Leonardo da Vinci*

### 6.1 An Improved White Dwarf Luminosity Function

When we started this project, our goal was to discover thousands of new white dwarfs in order to create an accurate white dwarf luminosity function so that we can study white dwarf cooling physics and determine the age of the Galactic disk precisely. First, we tried using a narrow-band filter to photometrically identify cool white dwarfs. However, this method turned out to be an inefficient way of identifying white dwarfs among many other field stars, and hence we had to change our strategy. Using proper motions from the USNO-B and the Sloan Digital Sky Survey, we succeeded in discovering a large number of white dwarfs. Our current luminosity function includes  $\sim 6000$  stars. The observed cut off of our new luminosity function is consistent with the previous luminosity functions, however due to uncertainties at the faint end, we have not been able to present a more precise age estimate.

The main uncertainty at the faint end of the luminosity function is caused by the lack of near-infrared photometry. Cool white dwarfs do not show any spectral features below 5000 K and the only way to tell the atmospheric compositions of the stars is to use optical and near-infrared photometry to differentiate between hydrogen and helium rich atmospheres. Hydrogen rich atmosphere white dwarfs show broad absorption features in the near-infrared. Harris et al. (2006; see Figure 6.1) assumed different fractions of hydrogen and helium rich atmospheres for cool white dwarfs and presented luminosity functions for three different cases. Their criteria include a most-likely H/He mix (Best Fractions), and two alternative mixes that favor more hydrogen types (Alternative A) and more helium types (Alternative B). Adopting a higher fraction of hydrogen-dominated stars (Alternative A) results in more stars being assigned fainter luminosities and gives a less pronounced drop and a more extended faint tail to the luminosity function. In order to resolve the present ambiguity at the faint end of the luminosity function, we are obtaining *JHK* photometry of the coolest white dwarfs from our SDSS sample at the NASA Infrared Telescope Facility and Gemini-North Telescope. The optical photometry from the SDSS complemented with near-infrared photometry will enable us to do a detailed model atmosphere analysis of each star and create an accurate luminosity function.

Another source of uncertainty in our luminosity function is caused by our kinematic selection bias. White dwarfs with low tangential velocities can have the same values of reduced proper motion as main-sequence subdwarfs with high tangential velocities, so the two types of stars overlap to some extent in our reduced proper motion diagram. In order to minimize contamination of our white dwarf sample, we have chosen a minimum tangential velocity  $V_{\min}$ . Candidate white dwarfs with  $V_{\tan} < V_{\min}$  are rejected from the sample, and a correction factor  $\chi$  is included in the luminosity function calculation for the rejected stars. Small values of  $V_{\min}$  introduce more contamination by subdwarfs, whereas high values reduce the contamination at

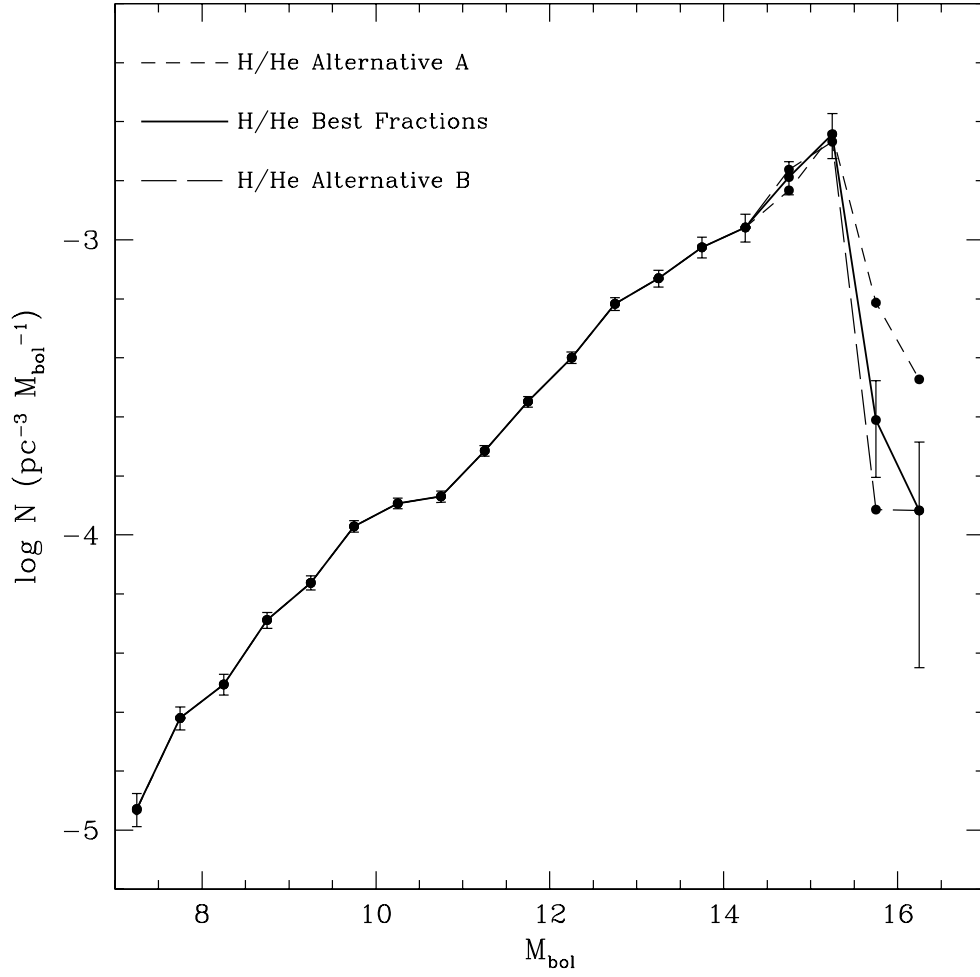


Figure 6.1: The luminosity function derived assuming different fractions of hydrogen- and helium-dominated atmospheres for the coolest white dwarfs (Harris et al. 2006).

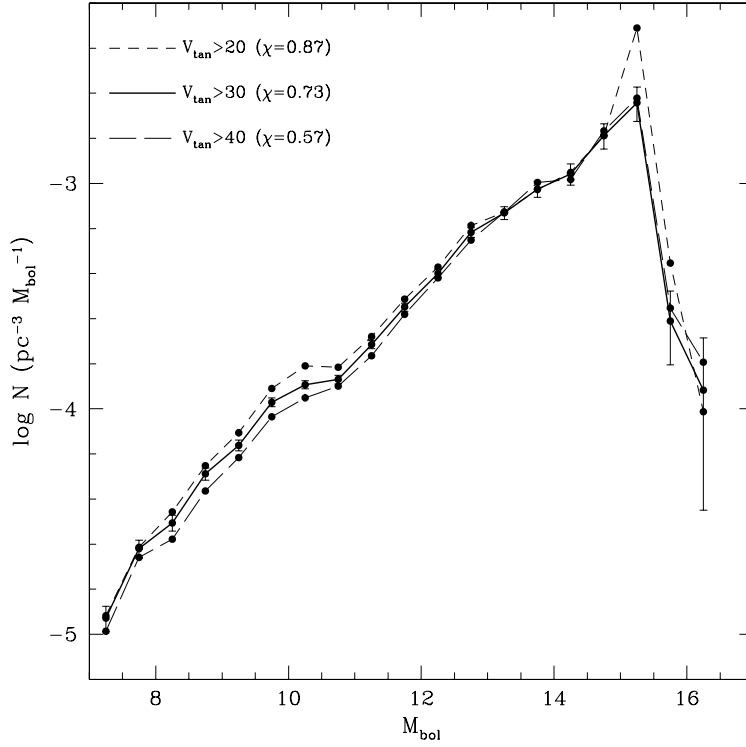


Figure 6.2: The luminosity function derived using different lower limits of tangential velocity. The factor ( $\chi$ ) comes from a particular kinematic model and it is used to account for low velocity white dwarfs below the selection limit (see Harris et al. 2006).

the expense of reducing our white dwarf sample and making the correction factor  $\chi$  more uncertain. Figure 6.2 presents the luminosity function for different tangential velocity cuts (Harris et al. 2006). The luminosity function includes 7116, 6000, and 4501 for  $V_{\text{tan}} = 20, 30$ , and  $40 \text{ km s}^{-1}$ , respectively.

Figure 6.2 shows that  $V_{\text{tan}} \geq 30$  and  $40 \text{ km s}^{-1}$  luminosity functions give similar results for the faint end, whereas  $V_{\text{tan}} \geq 20 \text{ km s}^{-1}$  luminosity function predicts a more pronounced peak at  $M_{\text{bol}} = 15-15.5$ . The overabundance of objects with  $M_{\text{bol}} = 15-15.5$  for the latter case is probably due to contamination from high

velocity subdwarfs. However, the observed peak coincides with the predicted peak in theoretical luminosity functions due to crystallization. Obtaining an accurate shape of the luminosity function in the  $M_{\text{bol}} = 15 - 15.5$  range is important for studies of crystallization and phase separation and necessary for calibrating theoretical ages of cool white dwarf stars. In order to eliminate subdwarfs from our sample of white dwarf candidates with  $V_{\text{tan}} \geq 20 \text{ km s}^{-1}$ , we have begun a project at the HET to spectroscopically confirm all of our candidates with  $M_{\text{bol}} \geq 14.6$ .

This search has been fruitful. We have discovered one of the coolest DQ white dwarfs (SDSS J124739.05+064604.6) with  $g - r = 1.34$ . This is currently the reddest white dwarf in our sample. In addition, we have discovered another white dwarf (SDSS J134532.92+420044.2) with  $V_{\text{tan}} \sim 21 \text{ km s}^{-1}$  at a distance of 20 pc. Our follow up spectroscopy of the coolest white dwarfs in Harris et al.'s (2006)  $V_{\text{tan}} \geq 30 \text{ km s}^{-1}$  sample showed that all of the objects except one (SDSS J091948.11+435621.6) are white dwarfs. Without follow-up spectroscopy, we would classify this object as a cool white dwarf with  $M_{\text{bol}} = 15.33$  and it would be one of the 10 white dwarfs that define the cut off in the luminosity function. We expect to secure optical spectroscopy of all cool white dwarf candidates with  $V_{\text{tan}} \geq 20 \text{ km s}^{-1}$  and  $M_{\text{bol}} \geq 14.6$  by the end of 2006. Our current (as of Mar 11, 2006) spectral classifications are shown in Figure 6.3.

### 6.1.1 The Future

One of the main limitations of our recent survey of high proper motion white dwarfs from the SDSS is the number of the coolest white dwarfs. The limitations imposed by the USNO-B plate astrometry restricted our study to  $g < 19.5$ . We did not discover many ultracool white dwarfs and we did not discover enough halo white dwarfs to create an accurate luminosity function for the Galactic halo.

Von Hippel et al. (2005) proposed to extend our survey and more fully

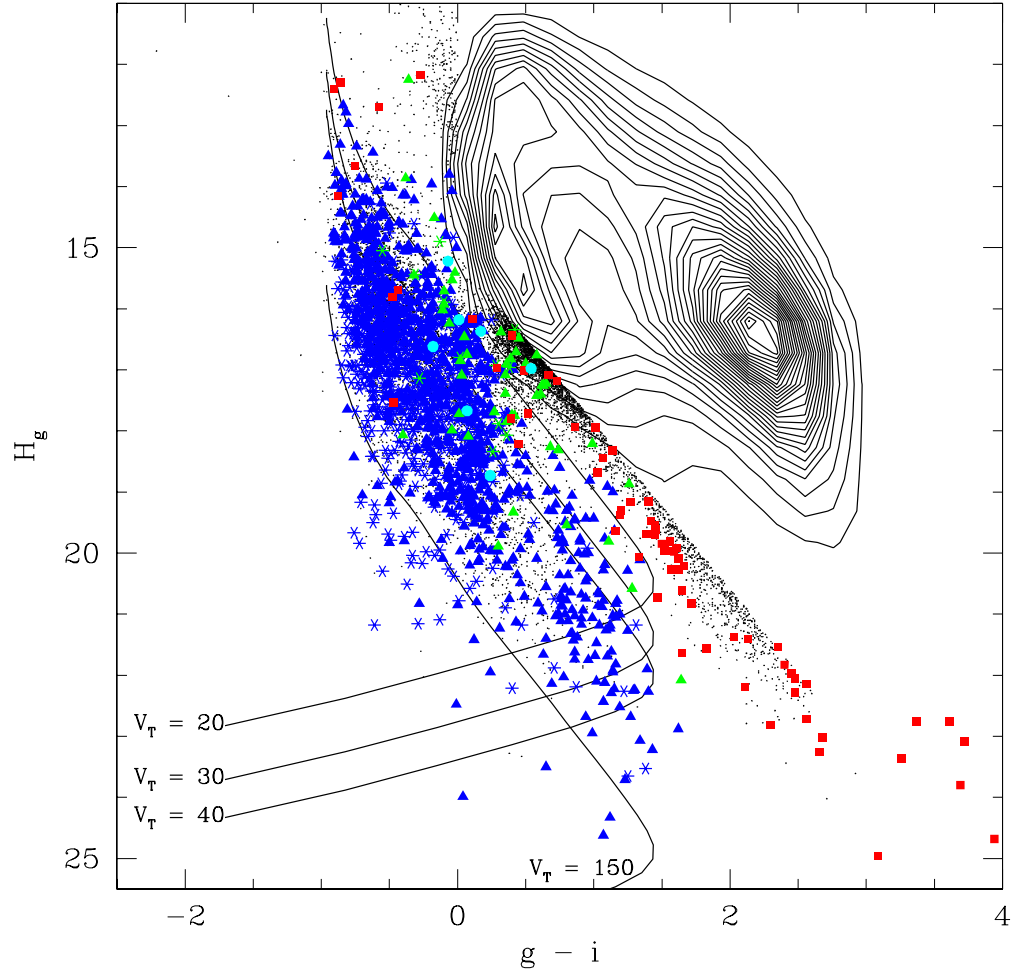


Figure 6.3: The reduced proper motion diagram for stars in the SDSS DR3. Spectroscopically confirmed white dwarfs, white dwarf plus late type star binaries, subdwarfs, and quasars are shown as blue triangles, green triangles, red squares, and cyan circles, respectively.

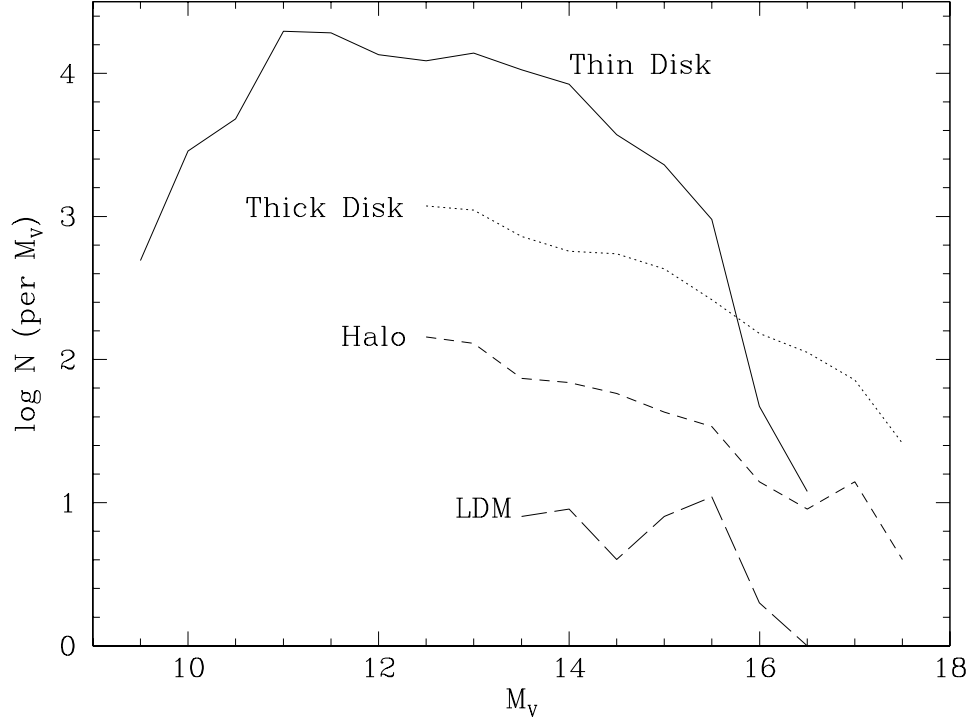


Figure 6.4: Expected number of white dwarfs for a  $r \leq 21$  survey of 5000 square degrees compared to the Liebert et al. (1988; LDM) luminosity function.

leverage the SDSS by conducting a single-filter ( $r$ ), deep ( $r = 21$ ) 5000 square degree astrometric survey. Using the Bok 90 inch telescope and the 90Prime camera (with 1 degree field-of-view) to image the SDSS Data Release 3 fields, we obtain an accuracy of  $20\text{--}25 \text{ mas yr}^{-1}$  for our proper motion measurements over a  $\sim 5$  year baseline. We have already started this survey in January 2006 and we were successful in obtaining accurate proper motion measurements for objects as faint as  $r = 21.5$ . The number of cool white dwarfs expected in this 5000 square degree survey is a vast improvement over what is available today. Figure 6.4 shows the expected number of white dwarfs with  $r \leq 21$  in 5000 square degrees compared to the Liebert et al. (1988; LDM) luminosity function.

The new astrometric survey will allow us to find 100,000 disk white dwarfs, including  $\sim 28$  white dwarfs in the last magnitude bin of the disk luminosity function, where the Liebert et al. (1988) sample has 3 stars. We also expect to find  $\sim 16,000$  thick disk and  $\sim 750$  halo white dwarfs. This survey will provide an excellent data set for the disk and thick disk, and a large sample of faint halo white dwarfs. This data set will allow us, for the first time, (1) to place the Galactic disk, thick disk, and halo on the same age scale; (2) to determine the age of the Galactic disk and halo precisely, and (3) to put strict limits on the contribution of halo white dwarfs to dark matter in the Galaxy. Pushing our survey to greater depth also leverages our experience with the techniques and our tremendous success at identifying cool white dwarfs via spectroscopy.

## 6.2 Resolving the Mystery of Cool White Dwarf Atmospheres

To first order, white dwarf photospheres are expected to be simple greybodies in the mid-infrared. In our Cycle 1 Spitzer program, we obtained the first mid-infrared photometry of white dwarfs cooler than 6500 K. Several cool white dwarfs ( $5000 \text{ K} < T_{\text{eff}} < 7000 \text{ K}$ ) in our sample showed mid-infrared flux deficits relative to white dwarf models. Neither the cause of this deficit nor its importance to white dwarf evolution is understood.

Extending our survey to the coolest white dwarfs in the Galaxy will be necessary to develop our understanding of ultra-cool white dwarf atmospheres, provide insights into radiative transfer in dense gases, and help us calibrate the age of the Galaxy based on cooling white dwarfs. By obtaining *Spitzer* IRAC photometry and IRS spectroscopy of white dwarfs with  $4000 \text{ K} \leq T_{\text{eff}} \leq 5500 \text{ K}$ , we can map the dependence of the mid-infrared flux deficits with temperature. Molecular absorp-

tion is expected to cause features in the SEDs, therefore, photometry in all IRAC channels and/or spectroscopy are required to constrain the exact shape of the SED.

There are  $\sim 50$  known cool white dwarfs with  $T_{\text{eff}} \leq 5500$  K that are bright enough to be observed with IRAC. In addition, several of them also allow us to do spectroscopy with IRS. *Are the flux deficits the shape of a molecular band-head or are they broad and featureless?* Resolving the mystery of near- and mid-infrared opacities will be necessary to be able to calculate reliable bolometric corrections and use the coolest white dwarfs as accurate chronometers to determine the age of Galactic populations.

### 6.3 Debris Disks Around White Dwarfs

Eighteen years after the discovery of an IR excess around a single white dwarf (G29-38, Becklin et al. 1987; Chary et al. 1999; Reach et al. 2005b), we have discovered the second (GD362, Kilic et al. 2005a; Becklin et al. 2005), third (GD56, Kilic et al. 2006c), and fourth (WD2115–560, von Hippel et al. 2006) debris disk around other single white dwarfs. In addition, Farihi et al. (2006) discovered another debris disk white dwarf. All of these white dwarfs are DAZs, they show trace amounts of metals in their hydrogen-dominated atmospheres.

The “Z” phenomenon (metals in white dwarf photospheres) has been puzzling astronomers for decades. Due to extremely large surface gravities, metals are predicted to sink down quickly to the bottom of the photosphere of white dwarf stars. The observed metals in white dwarfs can only be explained with continuous accretion from the surrounding medium (Koester et al. 2006). However, the search for a correlation between interstellar matter clouds and DAZ stars turned out to be inconclusive. There is not enough interstellar matter within the local ISM to explain the observed metal abundances in DAZ white dwarfs.

The discovery of 5 DAZ white dwarfs with circumstellar debris disks provides

a (partial) solution to this problem. Five out of 35 DAZs that have been observed in the near- or mid-infrared have debris disks. Our mid-infrared observations extend out to  $8\ \mu\text{m}$ , therefore they are capable of detecting warm debris disks. However, we would not be able to detect a cold or more distant reservoir of material around the stars. Photometry at longer wavelengths, including  $24$  and  $70\ \mu\text{m}$ , may help us discover extended debris disks around other DAZ stars. If so, circumstellar debris disks may explain most or all of the DAZ stars.

Mid-infrared spectroscopy of G29-38 (Reach et al. 2005b) showed that the debris disk is most likely created by the tidal disruption of a comet or an asteroid around the white dwarf. These debris disks appear to reveal the remnant planetary systems around white dwarfs. Zuckerman et al. (2003) found that 25% of all DA stars in their sample are DAZs. Koester et al. (2005) found a smaller percentage of DAZs ( $\sim 5\%$ ) in their study. In any case, these studies suggest that at least 5% of all white dwarfs may have remnant planetary systems. Stable planetary systems around white dwarfs would not create debris disks, therefore the percentage of white dwarfs with planetary systems may be higher.

### 6.3.1 The Future

Follow-up mid-infrared photometry and spectroscopy of the currently known five DAZs with circumstellar debris disks will be important. G29-38 shows a strong silicate feature at  $\sim 10\ \mu\text{m}$ . We do not know if the others have similar silicate features or if they are different. Studying the composition of the debris disks will reveal their source, whether they are the remnants of comets, asteroids, or planets.

Search for near- and mid-infrared excesses around more DAZs will be necessary to increase the number of known debris disk white dwarfs. The Sloan Digital Sky Survey has found several new DAZs (Eisenstein et al. 2006) that are suitable for a near-infrared search at an 8m-class telescope. In addition, searching for vari-

ability of the metal lines and mid-infrared flux distributions of DAZs will help us understand the evolution of debris disks. The diffusion timescales of metals in DAZ photospheres are on the orders of years, and they can be as short as several days for warmer DAZs. Therefore, if the accretion from the circumstellar debris disks is not continuous, we should detect variability in the metal lines on timescales of days to years. Follow-up optical spectroscopy of the Ca II, Mg, and Na I lines will be helpful.

## 6.4 Faint Halo White Dwarfs: The Ultra Deep Field

The deepest image of the Universe acquired with the Hubble Space Telescope, the Hubble Ultra Deep Field (HUDF; Beckwith et al. 2004), provides a new opportunity to study the structure of the Galactic disk and the halo to its limits. Previous deep field images, the Hubble Deep Field North and South were used extensively to constrain the stellar content of the Galaxy (Ibata et al. 1999; Mendez & Minniti 2000; Kilic et al. 2004a; Kilic et al. 2005b). The faint blue objects observed in these fields were thought to be old halo white dwarfs which would be consistent with the observed microlensing events toward the Large Magellanic Cloud (Alcock et al. 2000) and would explain part of the dark matter in the solar neighborhood. Kilic et al. (2004a; 2005b) and Pirzkal et al. (2005) showed that some of these faint blue objects are confused with quasars and an extensive study including spectral energy distribution fitting is required to identify stars in deep HST images.

We could identify possible white dwarf candidates in the HDF North and South using proper motion measurements from two epochs. Pirzkal et al. (2005) divided the original HUDF images into two epochs separated by 73 days in order to identify fast moving objects. They did not find any objects moving faster than 2.5 HUDF pixels ( $0.3 \text{ arcsec yr}^{-1}$ ). Their  $3\sigma$  detection limit was  $0.081 \text{ arcsec yr}^{-1}$ , and they did not detect any significant proper motion for the point sources that they

identified in the HUDF.

The HUDF was imaged at the end of 2003. Observing it again in the next HST cycle for 6-7 orbits will enable us to measure accurate proper motions down to  $I = 27$  over a 4 year baseline. More sensitive proper-motion measurements will be helpful to positively identify unresolved objects in the Galactic disk and halo. It would also allow us to search for high tangential velocity objects among the fainter ( $I > 27$ ) unresolved sources identified in the HUDF. Excluding halo membership of objects down to HUDF limiting magnitude would further constrain the maximum white dwarf contribution to the Galactic dark matter. Re-imaging of the HUDF should be done before the end of the HST era.

## 6.5 Overview

Our initial project was ambitious; we hoped to find two orders of magnitude more white dwarfs than previous studies. With the help of the Sloan Digital Sky Survey, we achieved our goal and discovered thousands of new white dwarfs. What we have found will not cure cancer or improve the lives of people living in poverty, but we are hoping that we provided new information/knowledge that will make people think about their place in the Universe. *“We are all in the gutter, but some of us are looking at the stars (Oscar Wilde)”*. Our work on debris disks around white dwarfs resulted in a press release which was printed in China, the Czech Republic, Hungary, Germany, Iran, Italy, and the USA. If we could make a child more curious about our discovery and astronomy in general, then we are happy.

There is always more than one interesting problem in any field of research. We got a chance to work on several interesting problems in white dwarf research including their mysterious atmospheres, their contribution to dark matter, and dust disks and planets around white dwarfs. Before we started, not much was known about these problems, and we still have a lot of questions to answer. However, we

are making progress in different fields and a lot more is on the way.

We tried to unlock the mysteries of white dwarf stars, yet we found more mystery than we can resolve. We do not think that we will solve every problem in white dwarf research. The saying “Shoot for the stars so that you can climb a tree.” reminds us that we need to shoot for all the hard problems and hopefully the answers will follow.

# Bibliography

- [1] Abazajian, K. et al. 2004, AJ, 128, 502
- [2] Abrikosov, A. A. 1960, Zh. Eksp. i. Teor. Fiz., 39, 1798
- [3] Adams, W. S. 1915, PASP, 27, 236
- [4] Adelman-McCarthy, J. K. et al. 2006, ApJS, 162, 38
- [5] Afonso et al. 2003, A&A, 400, 951
- [6] Alcock, C., Fristrom, C. C., & Siegelman, R. 1986, ApJ, 302, 462
- [7] Alcock, C. et al. 1997, ApJ, 486, 697
- [8] Alcock, C. et al. 2000, ApJ, 542, 281
- [9] Anderson, J., & King, I. R. 2000, PASP, 112, 1360
- [10] Angel, J. R. P. 1977, ApJ, 216, 1
- [11] Barger, A. J. et al. 2003, AJ, 126, 632
- [12] Becklin, E. E. & Zuckerman, B. 1988, Nature, 336, 656
- [13] Becklin, E. E. et al. 2005, ApJ, 632, 119
- [14] Beckwith, S. V. W. et al. 2004, in preparation

- [15] Bedin, L. R., Piotto, G., King, I. R., and Anderson, J. 2003, *A&A*, 126, 247
- [16] Bergeron, L. et al. 2005, *A&A*, in press, astro-ph/0509121
- [17] Bergeron, P. et al. 1994, *ApJ*, 423, 456
- [18] Bergeron, P., Saumon, D., & Wesemael, F. 1995, *ApJ*, 443, 764
- [19] Bergeron, P., Ruiz, M. T., & Leggett, S. K. 1997, *ApJS*, 108, 339
- [20] Bergeron, P., Leggett, S. K. , & Ruiz, M. T. 2001, *ApJS*, 133, 413
- [21] Bergeron, P. 2001, *ApJ*, 558, 369
- [22] Bergeron, P. & Leggett, S. K. 2002, *ApJ*, 580, 1070
- [23] Bergeron, P. 2003, *ApJ*, 586, 201
- [24] Bertin, E. & Arnouts, S. 1996, *A&AS*, 117, 393
- [25] Bessel, F. W. 1844, *MNRAS*, 6, 136
- [26] Borysow, A. et al. 1997, *A&A*, 324, 185
- [27] Brott, I. & Hauschildt, P. H. 2005, Proceedings of the Gaia Symposium "The Three-Dimensional Universe with Gaia" (ESA SP-576), Editors: C. Turon, K.S. O'Flaherty, M.A.C. Perryman, p.565
- [28] Casertano, S. et al. 2000, *A&A*, 120, 2747
- [29] Chabrier, G. Segretain, L., Hernanaz, M., & Mochkovitch, R., 1993, 8th E. Workshop on WDs, Kluwer A. Publishers, p. 115
- [30] Chabrier, G., Baraffe, I., Allard, F. & Hauschildt, P. 2000a, *ApJ*, 542, 464
- [31] Chabrier, G., Brassard, P., Fontaine, G., & Saumon, D. 2000b, *ApJ*, 543, 216

- [32] Chandrasekhar, S. 1931, ApJ, 74, 81
- [33] Chary, R., Zuckerman, B., & Becklin, E. E. 1999, ESA SP-427, 289
- [34] Chen, B. et al. 2001, ApJ, 553, 184
- [35] Chen, C. H. et al. 2005, ApJ, 634, 1372
- [36] Claver, C. F. 1995, Ph.D. Thesis, University of Texas
- [37] Cohen, J. G. et al. 2000, ApJ, 538, 29
- [38] Cushing, M. C., Vacca, W. D., & Rayner, J. T. 2004, PASP 116, 362
- [39] Cushing, M. C., Rayner, J. T., & Vacca, W. D. 2005, ApJ, 623, 1115
- [40] Cutri, R. M et al. 2003, VizieR Online Data Catalog, 2246
- [41] Dahn, C.C., Monet, D.G., & Harris, H.C. 1989, in IAU Colloq. 114, White Dwarfs, ed. G. Wegner (Berlin, Springer), 24
- [42] Debes, J. H. & Sigurdsson, S. 2002, ApJ, 572, 556
- [43] Dufour, P., Bergeron, P., & Fontaine, G. 2005, ApJ, 627, 404
- [44] Dupuis, J., Fontaine, G., Pelletier, C., & Wesemael, F. 1992, ApJS, 82, 505
- [45] Eisenstein, D. J. et al. 2006, ApJ, in press
- [46] Fazio, G. G. et al. 2004, ApJS, 154, 10
- [47] Gates, E. et al. 2004, ApJ, 612, 129
- [48] Eddington, A. S. 1926, The Internal Constitution of the Stars, Cambridge: Cambridge University Press
- [49] Fabricant, D. G., Hertz, E. H. & Szentgyorgyi, A. H. 1994, Proc. SPIE Vol. 2198, p. 251-263

- [50] Farihi, J. 2004, ApJ, 610, 1013
- [51] Farihi, J. 2005, AJ, 129, 2382
- [52] Farihi, J., Becklin, E. E., Zuckerman, B. 2005, ApJS, 161, 394
- [53] Fleming, T. A., Liebert, J., & Green, R. F. 1986, ApJ, 308, 176
- [54] Flynn, C., Gould, A., and Bahcall, J.N. 1996, ApJ, 466, 55
- [55] Fontaine, G., Brassard, P., & Bergeron, P. 2001, PASP, 113, 409
- [56] Fowler, R. H. 1926, MNRAS, 87, 114
- [57] Frommhold, L. 1993, Collision-induced absorption in gases, Cambridge (England)
- [58] Gates, E. 2004, ApJ, 612, 129
- [59] Geijo, E. M., Torres, S., Isern, J., & García-Berro, E. 2006, MNRAS, 511
- [60] Gianninas, A., Dufour, P., & Bergeron, P. 2004, ApJ, 617, 57
- [61] Giavalisco, M., and GOODS Team 2003, BAAS, 202, 1703
- [62] Giavalisco, M., and GOODS Team 2004, ApJ, 600, 93
- [63] Gilmore, G., King, I. R., and van der Kruit, P.C. 1989, Proceedings of the 19th Advanced Course of the Swiss Society of Astronomy and Astrophysics (SSAA), Saas-Fee, ed. R. Buser, and I. R. King (Mill Valey, University Science Books)
- [64] Girardi, L. et al. 2002, A&A 391, 195
- [65] Graham, J. R., Matthews, K., Neugebauer, G., & Soifer, B. T. 1990, ApJ, 357, 216
- [66] Greenstein, J.L. 1980, ApJ, 242, 738

- [67] Greenstein, J. L. & Liebert, J. W. 1990, *ApJ*, 360, 662
- [68] Hansen, B. M. S. 1998, *Nature*, 394, 860
- [69] Hansen, B. M. S. 1999, *ApJ*, 520, 680
- [70] Hansen, B. M. S., et al. 2004, *ApJS*, 155, 551
- [71] Harris, H. C. et al. 2001, *ApJ*, 549, 109
- [72] Harris, H. C. et al. 2006, *AJ*, 131, 571
- [73] Hilditch, R. W., Howarth, I. D., & Harries, T. J. 2005, *MNRAS*, 357, 304
- [74] Hogg, D. W. 2001, *AJ*, 122, 2129
- [75] Holberg, J.B., Oswalt, T. D., and Sion, E. M. 2002, *ApJ*, 571, 512
- [76] Holtzman, J. A. et al. 1995, *PASP*, 107, 1065
- [77] Hoyos, C., Guzman, R., Bershad, M. A., Koo, D. C., & Diaz, A. I. 2004, *AJ*, 128, 1541
- [78] Ibata, R. A., Richer, H. B., Gilliland, R. L., and Scott, D. 1999, *ApJ*, 524, 95
- [79] Ibata, R., Irwin, M., Bienaymé, O., Scholz, R., & Guibert, J. 2000, *ApJ*, 532, 41
- [80] Iben, I. Jr. & Tutukov, A. V. 1984, *ApJ*, 282, 615
- [81] Iben, I. Jr. 1991, *ApJS*, 76, 55
- [82] Jorgensen, U. G., Hammer, D., Borysow, A., & Falkesgaard, J. 2000, *A&A*, 361, 283
- [83] Jura, M. 2003, *ApJ*, 584, 91

- [84] Kawaler, S. D. 1996, *ApJ*, 467, 61
- [85] Kepler, S. O. et al. 2005, *ApJ*, 634, 1311
- [86] Kilic, M., Winget, D. E., von Hippel, T., & Claver, C. F. 2003, *NATO ASIB Proc. 105: White Dwarfs*, 389
- [87] Kilic, M., von Hippel, T., Mendez, R. A., & Winget, D. E. 2004a, *ApJ*, 609, 766
- [88] Kilic, M., Winget, D. E., von Hippel, T., & Claver, C. F. 2004b, *AJ*, 128, 1825
- [89] Kilic, M., von Hippel, T., Leggett, S. K., & Winget, D. E. 2005a, *ApJ*, 632, 115
- [90] Kilic, M., Mendez, R. A., von Hippel, T., & Winget, D. E. 2005b, *ApJ*, 633, 1126
- [91] Kilic, M. et al. 2006a, *AJ*, 131, 582
- [92] Kilic, M. et al. 2006b, *ApJ*, 642, 1051
- [93] Kilic, M., von Hippel, T., Leggett, S. K., & Winget, D. E. 2006c, *ApJ*, 646, 474
- [94] Kilic, M., von Hippel, T., & Winget, D. E. 2006d, *ApJ*, submitted
- [95] Kleinman, S. J. et al. 2004, *ApJ*, 607, 426
- [96] Kirzhnits, D. A. 1960, *Soviet Phys. - JETP*, 11, 365
- [97] Knox, R. A., Hawkins, M. R. S., & Hambly, N. C. 1999, *MNRAS*, 306, 736
- [98] Koekemoer, A. M. et al. 2002, "HST Dither Handbook", Version 2.0, (Baltimore:STScI)
- [99] Koester, D., Provencal, J., & Shipman, H. L. 1997, *A&A*, 320, 57

- [100] Koester, D. et al. 2005, A&A, 432, 1025
- [101] Koester, D. & Wilken, D. 2006, A&A, in press
- [102] Kowalski, P. M. & Saumon, D. 2004, ApJ, 607, 970
- [103] Kowalski, P. M., Saumon, D., & Mazevet, S. 2005, ASP Conf. Ser. 334: 14th European Workshop on White Dwarfs, 203
- [104] Kowalski, P. M. 2006, ApJ, 641, 488
- [105] Kurucz, R. L. 1995, Workshop on Laboratory and astronomical high resolution spectra. Proceedings of ASP Conference no. 81; edited by A.J. Sauval, R. Blomme, and N. Grevesse, p.583
- [106] Leggett, S. K., Ruiz, M. T., & Bergeron, P. 1998, ApJ, 497, 294
- [107] Leggett, S. K. et al. 2002, ApJ, 564, 452
- [108] Lennon, D. J. 1999, Revista Mexicana de Astronomia y Astrofisica Conference Series, 8, 21
- [109] Lépine, S., Shara, M.M., & Rich, R.M. 2003, AJ, 126, 921
- [110] Liebert, J. 1979, In IAU Colloquium 53: White Dwarfs and Variable Degenerate Stars, p. 146
- [111] Liebert, J., Dahn, C. C., & Monet, D. G. 1988, ApJ, 332, 891
- [112] Liebert, J., Bergeron, P., & Holberg, J. 2005, ApJS, 156, 47
- [113] Luyten, W. J. 1918, Lick Observatory Bulletin, 10, 135
- [114] Luyten, W. J. 1979, LHS Catalogue. A Catalogue of Stars with Proper Motions Exceeding 0.5" Annually (Minneapolis: Univ. Minnesota)

- [115] Mathewson, D. S. & Ford, V. L. 1984, IAUS, 108, 125
- [116] Maxted, P. F. L., Marsh, T. R., & Moran, C. K. J. 2000, MNRAS, 319, 305
- [117] McCook, G. P. & Sion, E. M. 2003, VizieR On-line Data Catalog: III/235
- [118] Mendez, R. A. et al. 1996, MNRAS, 283, 666
- [119] Mendez, R. A., and Minniti, D. 2000, ApJ, 529, 911
- [120] Mendez, R. A. 2002, A&A, 395, 779
- [121] Mestel, L. 1952, MNRAS, 112, 583
- [122] Metcalfe, T. S., Montgomery, M. H., & Kanaan, A. 2004, ApJ, 605, 133
- [123] Monelli, M. et al. 2005, ApJ, 621, 117
- [124] Monet, D. G., et al. 2003, AJ, 125, 984
- [125] Montgomery, M. H., Klumpe, E. W., Winget, D. E., & Wood, M. A. 1999, ApJ, 525, 482
- [126] Morrison, H. L. et al. 2000, AJ, 119, 2254
- [127] Morrison, H. L. et al. 2001, AJ, 121, 283
- [128] Munn, J. A. et al. 2004, AJ, 127, 3034
- [129] Oppenheimer, B. R. Hambly, N. C. Digby, A. P. Hodgkin, S. T. & Saumon, D. 2001, Science, 292, 698
- [130] Oswalt, T. D., Smith, J. A., Wood, M. A., & Hintzen, P. 1996, Nature, 382, 692
- [131] Paquette, C., Pelletier, C., Fontaine, G., & Michaud, G. 1986, ApJS, 61, 197

- [132] Pham, H. A. 1997, ESA SP-402: Hipparcos, Venice, 559
- [133] Pelletier, C. et al. 1986, ApJ, 307, 242
- [134] Pickles, A. J. 1998, PASP, 110, 863
- [135] Pirzkal, N. et al. 2005, ApJ, 622, 319
- [136] Rayner, J. T. et al. 2003, PASP, 115, 362
- [137] Reach, W. T. et al. 2005a, PASP, 117, 978
- [138] Reach, W. T. et al. 2005b, ApJ, 635, 161
- [139] Reid, N., and Majewski, S. R. 1993, ApJ, 409, 635
- [140] Reid, I. N., Sahu, K.C., & Hawley, S.L. 2001, ApJ, 559, 942
- [141] Reyle, C., Robin, A. C., & Creze, M. 2001, A&A, 378, 53
- [142] Richer, H. B., Hansen, B. M. S., Limongi, M., Chieffi, A., Straniero, O., and Fahlman, G. G. 2000, ApJ, 529, 318
- [143] Richer, H. B. et al. 2001, preprint, astro-ph/0107079
- [144] Richer, H. B., et al. 2005, American Astronomical Society Meeting Abstracts, 207, #128.08
- [145] Roellig, T. L. et al. 2004, ApJS, 154, 418
- [146] Salaris, M., García-Berro, E., Hernanz, M., Isern, J., & Saumon, D. 2000, ApJ, 544, 1036
- [147] Salpeter, E. E. 1961, ApJ, 134, 669
- [148] Saumon, D. & Jacobson, S. B. 1999, ApJ, 511, 107

- [149] Schatzman, E. 1958, *White Dwarfs*, Amsterdam, North Holland Publishing Co; New York, Interscience Publishers
- [150] Schlegel, D. J., Finkbeiner, D. P., & Davis, M. 1998, *ApJ*, 500, 525
- [151] Schmidt, G. D., Bergeron, P., & Fegley, B. Jr. 1995, *ApJ*, 443, 274
- [152] Schneider, D. P. et al. 2003, *AJ*, 126, 2579
- [153] Schulze, H. J., Polls, A., Ramos, A., & Vidana, I. 2006, *PhRvC*, 73, 058801
- [154] Silvestri, N. M., Oswalt, T. D., & Hawley, S. L. 2002, *AJ*, 124, 1118
- [155] Smith, J. A. et al. 2002, *AJ*, 123, 2121
- [156] Spagna, A., Carollo, D., Lattanzi, M. G., & Bucciarelli, B. 2004, *A&A*, 428, 451
- [157] Stevenson, D. J. 1980, *Journal de Physique*, 41, 2
- [158] Tokunaga, A. T., Becklin, E. E., & Zuckerman, B. 1990, *ApJ*, 358, 21
- [159] Udalski, A., Szymanski, M., Kaluzny, J., Kubiak, M., & Mateo, M. 1992, *AcA*, 42, 253
- [160] Vacca, W. D., Cushing, M. C., & Rayner, J. T. 2003, *PASP* 115, 389
- [161] Vanden Berk D. E. et al. 2001, *AJ*, 122, 549
- [162] Van Horn, H. M. 1968, *ApJ*, 151, 227
- [163] Van Maanen, A. 1913, *PASP*, 29, 258
- [164] von Hippel, T. & Bothun, G. 1990, *AJ*, 100, 403
- [165] von Hippel, T. 2001, 12th European Workshop on White Dwarfs, ASP Conference Proceedings, Vol. 226, p. 415

- [166] von Hippel, T., et al. 2005, ASP Conf. Ser. 334: 14th European Workshop on White Dwarfs, 334, 3
- [167] Werk, J. K., Jangren, A., & Salzer, J. J. 2004, ApJ, 617, 1004
- [168] Werner, M. W. et al. 2004, ApJS, 154, 1
- [169] Wheeler, J. C. 2000, Cosmic Catastrophes, Cambridge, UK: Cambridge University Press
- [170] Wickramasinghe, D. T., Allen, D. A., & Bessel, M. S. 1982, MNRAS, 198, 473
- [171] Williams, R. E. et al. 1996, AJ, 112, 1335
- [172] Winget, D. E. et al. 1987, ApJ, 315, L77
- [173] Winget, D. E. et al. 2003, ASP Conf. Ser. 294: Scientific Frontiers in Research on Extrasolar Planets, 59
- [174] Winget, D. E. et al. 2004, ApJ, 602, 109
- [175] Wirth, G. D. et al. 2004, preprint, astro-ph/0401353
- [176] Wolff, B., Koester, D., & Liebert, J. 2002, A&A, 385, 995
- [177] Wood, M. A. 1990, Ph.D. Thesis Texas Univ., Austin
- [178] Wood, M. A. 1992, ApJ, 386, 539
- [179] Wood, M. A. 1995, Proceedings from the 9th European Workshop on White Dwarfs, Vol. 443, p. 41
- [180] Wood, M. A. & Oswalt, T. D. 1998, ApJ, 497, 870
- [181] Young, P. J. 1976, AJ, 81, 807
- [182] Zuckerman, B., & Becklin, E. E. 1987, Nature, 300, 138

[183] Zuckerman, B., Koester, D., Reid, I. N., & Hunsch, M. 2003, *ApJ*, 596, 477

# Vita

Mukremin Kilic was born in Bursa, Turkey on 15 May 1977. He lived in Bursa with his parents Aziz and Rebiye and brothers Zakir, Zeki, and Enes until graduating from Malcılar Secondary School in 1991. In August of that year, he moved to Kayseri, Turkey to attend Kayseri Science High School for three years. He moved to Istanbul in 1994 to study Physics at Boğaziçi (Bosphorus) University, where he received a Bachelor of Science degree in May 1999. He came to Austin, Texas in August 2000 to begin graduate studies in the Department of Astronomy at the University of Texas.

Permanent Address: 4310 Avenue B, Apt 113, Austin TX, 78751

This dissertation was typeset with L<sup>A</sup>T<sub>E</sub>X 2<sub>ε</sub><sup>1</sup> by the author.

---

<sup>1</sup>L<sup>A</sup>T<sub>E</sub>X 2<sub>ε</sub> is an extension of L<sup>A</sup>T<sub>E</sub>X. L<sup>A</sup>T<sub>E</sub>X is a collection of macros for T<sub>E</sub>X. T<sub>E</sub>X is a trademark of the American Mathematical Society. The macros used in formatting this dissertation were written by Dinesh Das, Department of Computer Sciences, The University of Texas at Austin, and extended by Bert Kay, James A. Bednar, and Ayman El-Khashab.